Neurodegenerative Diseases — Empowering Hope

AD/PD 2026

siemens-healthineers.com/alzheimer-disease

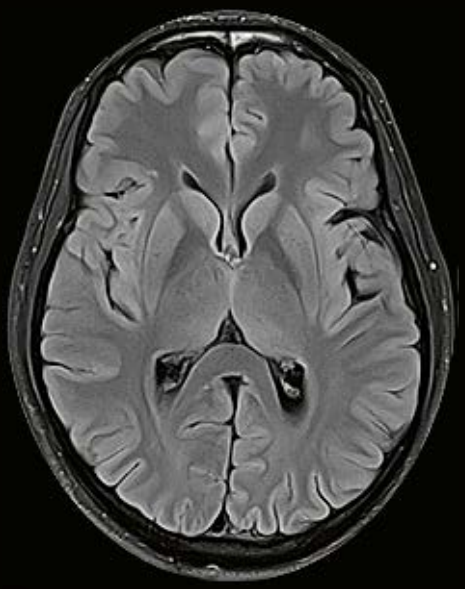

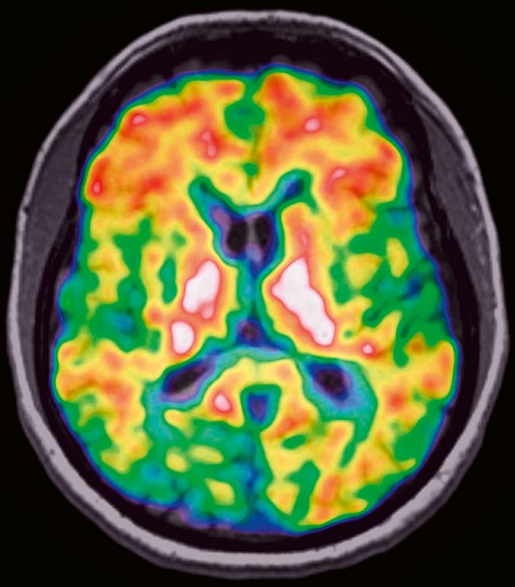

SIEMENS Healthineers

A clinician's guide to detecting and diagnosing ARIA in Alzheimer's disease patients

Abstract

In the rapidly evolving landscape of Alzheimer's disease treatment, the quest for effective therapies has brought to light a critical challenge: the detection and management of amyloid-related imaging abnormalities (ARIA), which may result from anti-amyloid disease modifying therapies. Encompassing both ARIA-E (edema/effusion) and ARIA-H (hemorrhage/hemosiderosis), ARIA represents a spectrum of MRI-detectable changes that can complicate the clinical management of patients undergoing amyloid-targeting therapies. And clinicans play a critical role in precisely detecting and diagnosing ARIA to ensure patient safety and support the effective delivery of treatment.

This guide is designed to equip clinicians with the essential knowledge and practical strategies needed to navigate the complexities of ARIA detection, delving into MRI techniques that reveal the subtle, yet significant, imaging abnormalities associated with ARIA. By providing a comprehensive overview of current best practices, from optimizing MRI sequences to interpreting findings and making informed treatment decisions, this article aims to enhance diagnostic precision and improve patient outcomes. As we advance in our fight against Alzheimer's disease, mastering ARIA detection is not just a necessity — it's a cornerstone of responsible and effective patient management in the era of innovative therapies.

Alzheimer's disease: An increasing challenge for healthcare providers

Globally, an estimated 55 million people [1] are currently living with dementia. By 2050, the number of new dementia cases is projected to more than double, affecting up to 139 million people [1].

Alzheimer's disease (AD) is the most common neurodegenerative disease worldwide [2] and most common form of dementia accounting for over 60–80 % of all dementia cases [3]. Clinically characterized by a gradual decline in cognitive function, memory, and reasoning abilities, AD progresses through mild, moderate, and severe stages, eventually leading to complete dependency and death. Pathologically, AD is marked by the accumulation of extracellular amyloid-beta (Aβ) plaques and intracellular neurofibrillary tangles (tau tangles) in the brain, leading to neuronal loss and brain atrophy. The presence of Aβ plaques is one of the defining features of the disease [4].

Although the underlying pathophysiology of AD is complex, the prevailing theory postulates that Aβ accumulation directly results in synaptic dysfunction, neurodegeneration, and, ultimately, clinical symptoms [5–7]. As a result, the AD drug development pipeline consists of many disease-modifying treatments, such as immunotherapy with monoclonal antibodies, that typically target the cessation of Aβ formation or facilitate plaque removal [8]. These AD therapies can cause side effects described as amyloid-related imaging abnormalities (ARIA) [9].

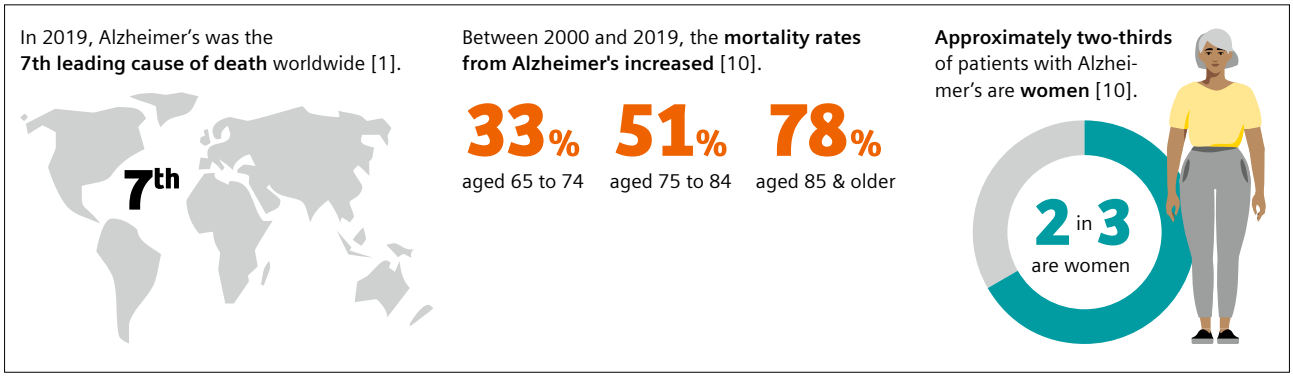

What is ARIA?

In July 2010, the Alzheimer's Association Research Roundtable convened a working group comprising academic and industry representatives, which first introduced "ARIA" as a term encompassing a spectrum of magnetic resonance imaging (MRI) findings observed in patients receiving anti-Aβ immunotherapies for AD. Recognizing the potential development of ARIA in patients undergoing monoclonal antibody treatment for AD, the working group established recommendations regarding inclusion and exclusion criteria, as well as safety monitoring for AD clinical trials [9].

Significant advances have been made in our understanding of ARIA since the 2010 working group. ARIA refers to imaging findings seen exclusively on MRI, and depending on the MRI appearance, two types of ARIA are recognized: ARIA-E, which is characterized by edema and effusion, and ARIA-H, which is characterized by microhemorrhages and superficial siderosis [9].

What causes ARIA?

ARIA is an inherently imaging-based phenomenon that emerges in patients with AD undergoing treatment with novel amyloid-targeting therapies, such as Lecanemab and Donanemab [11,12]. Although the mechanisms underlying ARIA are not fully understood, the current hypothesis is that these abnormalities occur due to the breakdown of the blood-brain barrier as a result of the binding of monoclonal antibodies to accumulated Aβ in the cerebral parenchyma and vasculature [9]. This binding leads to amyloid clearance, resulting in loss of vessel wall integrity and vessel leakiness of proteinaceous fluid (ARIA-E) and heme products (ARIA-H) [9].

"ARIA is an inherently image-based phenomenon. The diagnosis of ARIA depends on the radiologic diagnosis. Radiologist education and understanding of how to interpret these cases is crucial."

Ana M. Franceschi, M.D., Ph.D.,
Associate Professor of Radiology,
Division of Neuroradiology Lenox Hill Hospital, USA
Donald and Barbara Zucker School of Medicine at Hofstra/Northwell, USA

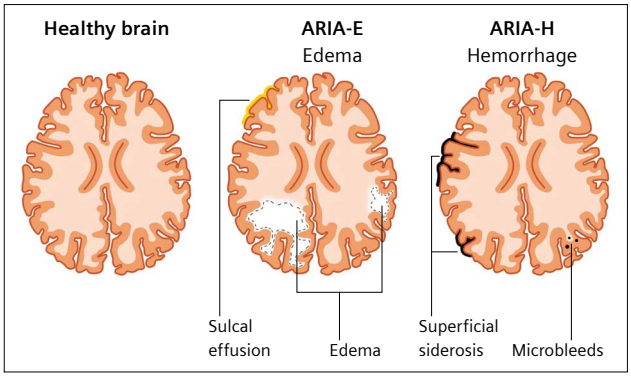

ARIA-E vs. ARIA-H

ARIA-E and ARIA-H are both associated with amyloid-targeting therapies used in the treatment of AD, but they differ in their underlying pathology and imaging characteristics (Fig. 1) [11]. Both ARIA-E and ARIA-H typically occur early in the treatment course (within six months), and approximately 90% of patients are asymptomatic, underscoring the importance of routine imaging monitoring [11].

Pathophysiology of ARIA-E (edema and effusion)
ARIA-E involves the leakage of fluid into the brain parenchyma or into the subarachnoid space, resulting in cerebral edema or effusions. Detected through MRI scans, ARIA-E appears as regions of hyperintensity on T2-weighted FLAIR (fluid-attenuated inversion recovery) sequences. ARIA-E may present as local mass effect and gyral swelling [13].

Pathophysiology of ARIA-H (microhemorrhages and superficial siderosis)
ARIA-H involves microhemorrhages or small areas of bleeding within the brain tissue, leading to the deposition of hemosiderin (a blood breakdown product) [14]. Detected through MRI scans, particularly on T2*-weighted and susceptibility-weighted imaging (SWI) sequences, ARIA-H appears as hypointense (dark) spots on these MRI sequences, indicating areas of microbleeding [14].

ARIA-E, ARIA-H, and Cerebral Amyloid Angiopathy (CAA)
ARIA-E and ARIA-H have similar MRI findings to cerebral amyloid angiopathy (CAA). Both ARIA and CAA are related to the deposition of Aß in cerebral blood vessels, which compromises the integrity of the vascular walls and the blood-brain barrier [9]. This compromised integrity can lead to fluid leakage, causing edema in ARIA-E and inflammatory CAA, and to microhemorrhages or hemosiderin deposits, as seen in ARIA-H and CAA-associated microbleeds [9].

	ARIA-E		ARIA-H	
	Edema	Effusion	Microhemorrhage	Superficial siderosis
Primary MRI features	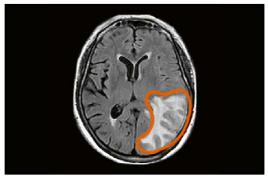	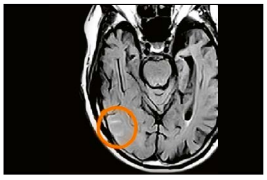	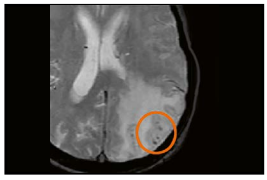	
	Parenchymal edema in the left parieto-occipital lobe (T2 FLAIR) *(solid circle)*	Leptomeningeal effusion in several sulci within the right temporo-occipital lobe (T2 FLAIR) *(solid circle)*	Several small parenchymal microbleeds in the left occipital lobe (T2*) *(solid circle)*	Small leptomeningeal hemosiderin deposit in the left frontal lobe sulcus (T2*) *(solid circle)*
Nature and location of leakage products	Leakage of intravascular fluid and proteins into the parenchymal interstitial fluid compartment	Leakage of proteinaceous fluid into the lepto-meningeal/subarachnoid space	Leakage of blood degradation products into adjacent brain parenchyma	Leakage of blood degradation products into subarachnoid space

1 **Main characteristics of ARIA-E and ARIA-H.** ARIA-E is characterized by the presence of parenchymal edema and sulcal effusions. ARIA-H is usually seen in combination with ARIA-E and is characterized by the presence of parenchymal microhemorrhages (most common) and sulcal/leptomeningeal hemosiderin deposits [11].

CAA is frequently detected in up to 90% of patients with AD [10]. And clinically, ARIA and CAA present with overlapping symptoms, such as headaches, cognitive decline, seizures, and focal neurological deficits, reflecting the underlying vascular and inflammatory processes. Therefore, the only real distinguishing feature between ARIA and CAA is clinical context: ARIA only occurs in individuals undergoing treatment with amyloid lowering agents, whereas CAA has been shown to be associated with AD independent of amyloid plaque and tau tangle pathology [11,12].

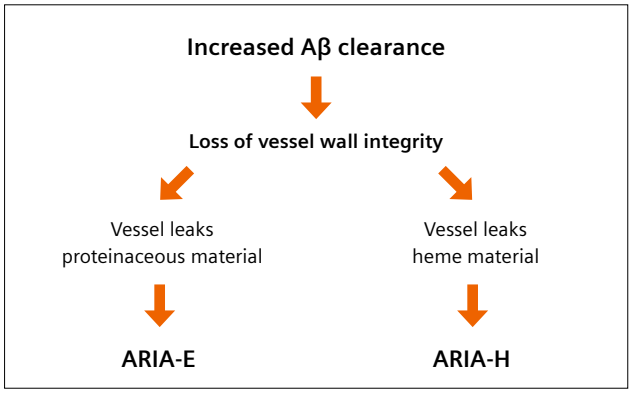

2 **Pathophysiology of ARIA.** The current hypothesis is that these abnormalities occur due to the breakdown of the blood-brain barrier as a result of the binding of monoclonal antibodies to accumulated Aβ in the cerebral parenchyma and vasculature [9]. This binding leads to increased amyloid clearance, resulting in loss of vessel wall integrity and vessel leakiness of proteinaceous fluid (ARIA-E) and heme products (ARIA-H).

Risk factors for ARIA

The primary risk factor for both ARIA-E and ARIA-H is apolipoprotein E (APOE) ϵ4 allele carriership. Patients with the APOE ϵ4 allele tend to have higher Aβ loads in both brain tissue and blood vessels. This increased amyloid burden is thought to enhance perivascular Aβ clearance under antibody treatment, which in turn heightens vascular permeability [9]. This heightened permeability allows protein-rich fluid and red blood cells to leak out, leading to ARIA-E and ARIA-H, respectively (Fig. 2) [9]. Therefore, genetic testing prior to treatment initiation is crucial for clinicians to identify patients at higher risk for ARIA.

Additional risk factors

- **High dosages of anti-Aβ immunotherapies:** ARIA-E demonstrates an additional dose dependence, occurring more frequently at higher doses of anti-Aβ immunotherapies due to greater mobilization of Aβ [9].
- **Antithrombotic medications:** Previous clinical trials have shown that concomitant anti-amyloid treatment with anti-coagulants, antiplatelets or antithrombotics is associated with increased risk of ARIA-H, warranting potential exclusion in these patient populations [9].
- **Existing microhemorrhages:** Patients who already have cerebral microbleeds or CAA at baseline are at higher risk for developing additional microhemorrhages with anti-amyloid therapy [11].
- **Age:** Advanced age can increase susceptibility to ARIA-E and ARIA-H due to cumulative vascular damage and decreased repair mechanisms [15].

Detecting, monitoring, and managing ARIA

Regular MRI is required to detect and monitor different forms of ARIA during initiation of approved antiamyloid therapies, such as Lecanemab and Donanemab [16]. The guidelines for using MRI to detect ARIA typically include protocols for baseline imaging, regular monitoring, and managing detected abnormalities. These guidelines aim to ensure early detection and appropriate intervention to mitigate potential risks associated with amyloid-targeting treatments. In this next section, we provide the key imaging characteristics of ARIA-E and ARIA-H detection.

Imaging characteristics of ARIA-E

ARIA-E is easily detected using T2-weighted FLAIR MRI sequences [17], examplary T2 FLAIR images are shown in Figure 3. FLAIR is particularly effective for highlighting abnormalities in brain tissue by suppressing the signal from cerebrospinal fluid, thereby enhancing the visibility of pathologies like edema. Prolonged signals on T2 FLAIR sequences within the brain (intra-axial) highlight the presence of edema, prolonged signals outside the brain (extra-axial) represent effusion or exudate in the sulci or leptomeningeal spaces [18].

ARIA-E appear as areas of increased signal intensity (hyperintensity) in the cortical and subcortical regions of the brain [17]. The hyperintense areas may also show mild swelling of the gyri (the ridges of the brain's surface) (Fig. 1). This indicates localized swelling due to fluid accumulation. In some ARIA-E cases, there can be a slight mass effect, which means the swelling may cause pressure on adjacent brain structures. This can be seen as displacement or compression of nearby brain tissue [18].

When ARIA-E affects the sulci, it might be mistaken for leptomeningeal processes if the radiologist is not aware that the patient is undergoing monoclonal antibody therapy for AD. ARIA-E more frequently affects the occipital lobes than the parietal, frontal, and temporal lobes. It is much less common in the cerebellum [14]. Having baseline MRI images before starting amyloid-targeting therapy is crucial. These baseline images allow for the detection of subtle changes that occur later, making it easier to identify and diagnose ARIA-E accurately.

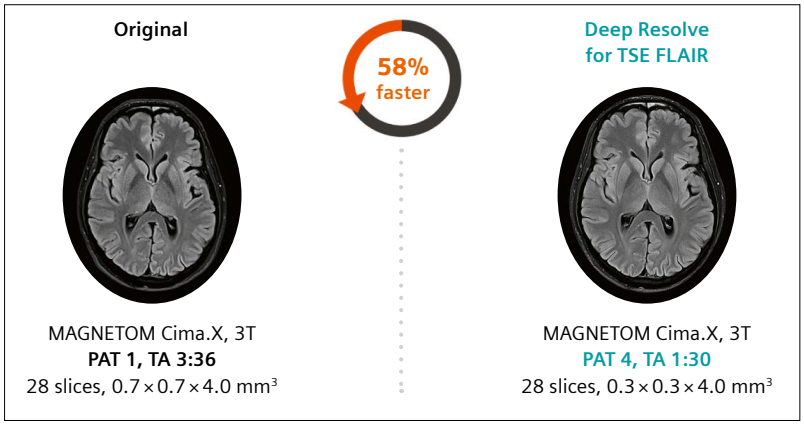

3 **Comparison of conventional and advanced brain scans using the MAGNETOM Cima.X 3T system.** The left image shows a conventional brain scan (PAT 1, TA 3:36) captured with the MAGNETOM Cima.X 3T scanner, highlighting standard resolution and contrast. The right image demonstrates the use of Siemens Healthineers' Deep Resolve for TSE FLAIR (PAT 4, TA 1:30), offering enhanced image clarity and detail, as well as a 58% faster scanning time.

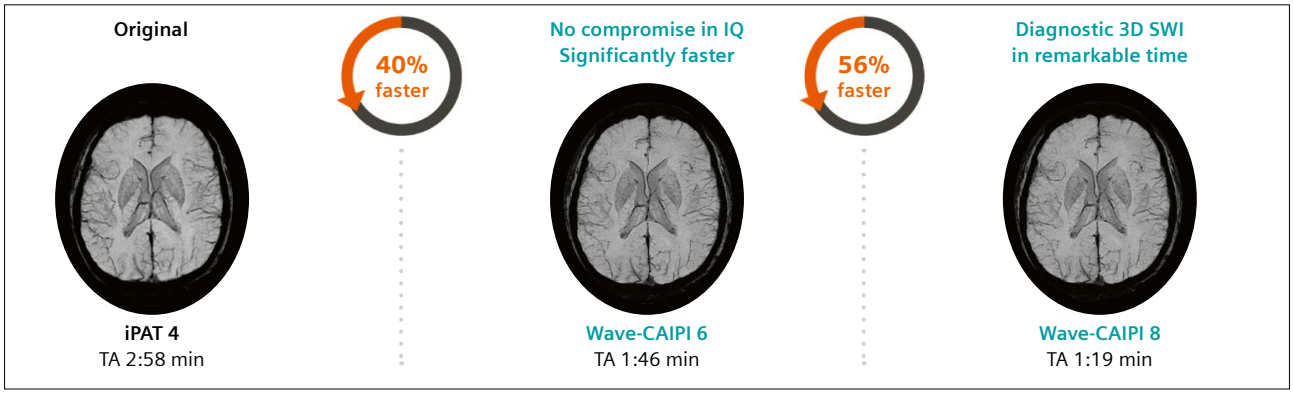

4 **Comparison of brain scans using standard and advanced SWI techniques.** The first image shows a brain scan with current standard SWI using iPAT 4 (TA 2:58 mins), offering a high-quality but longer acquisition time. The second image highlights a faster scan using Wave-CAIPI 6 (TA 1:46 mins) with no compromise in image quality (IQ), reducing scan time significantly. The third image features a diagnostic 3D SWI using Wave-CAIPI 8 (TA 1:19 mins), delivering remarkable time efficiency while maintaining excellent diagnostic clarity, ideal for rapid yet precise brain imaging.

Imaging characteristics of ARIA-H

ARIA-H is detected on MRI using long echo time (TE) T2*-weighted gradient echo (GRE) sequences. These sequences are sensitive to magnetic susceptibility differences caused by hemosiderin deposits that appear as markedly hypointense signals in the brain parenchyma or sulci. ARIA-H can also be detected through SWI, a technique that uses high-resolution 3D spoiled GRE acquisition, providing higher spatial resolution and increased sensitivity compared to conventional T2*-weighted GRE sequences [9]. SWI can detect hemosiderin, calcification, and iron deposits with greater accuracy [9]. Exemplary SWI images are shown in Figure 4.

On T2*-weighted GRE and SWI sequences, ARIA-H appear as areas of hypointense signal due to the presence of hemosiderin deposits in the brain tissue. T2*-weighted GRE sequences augment the effects of local field variations and spin dephasing caused by microhemorrhages, resulting in susceptibility-related signal loss, commonly referred to as "blooming" [9]. This increases the conspicuity of microhemorrhages (Fig. 1).

The imaging characteristics of ARIA-H are similar to those seen in CAA. However, ARIA-H typically affects the lobar regions of the brain, especially at the gray-white matter junction or cortex. This means the hemorrhages are more common in the outer parts of the brain, unlike hypertensive hemorrhages which usually occur in the deep gray matter structures of the brain [9].

ARIA-H is usually not visible on CT scans or standard MRI sequences like T1-weighted, T2-weighted, FLAIR or diffusion-weighted imaging (DWI) [9]. These sequences lack the sensitivity to detect the small, subtle changes caused by hemosiderin deposits. Therefore, long-TE T2*-weighted GRE and SWI are the preferred MRI techniques for detecting ARIA-H due to their sensitivity to hemosiderin [9].

Field strength of MRI magnet in ARIA detection

Field strength of the MRI magnet matters for the detection of ARIA. Higher field strength magnets, such as 3 Tesla (3T) compared to 1.5 Tesla (1.5T), offer several advantages in the detection of ARIA-E and ARIA-H.

So, several consensus documents are now recommending 3T MRI machines over 1.5T [19]. The use of low-field 0.55T MRI machines is currently under investigation for detecting ARIA, particularly in resource-limited settings [19]. However, low-field MRI has reduced SNR, reduced susceptibility-weighting, and longer scan times, which can result in lower image resolution and quality [20].

Here's how field strength impacts ARIA detection

- **Improved Signal-To-Noise Ratio (SNR):** 3T magnets provide a higher SNR compared to 1.5T magnets. This improved SNR enhances the overall quality of the images, making subtle abnormalities more detectable [21]. The increased SNR is particularly useful in detecting the subtle changes associated with ARIA, such as small areas of edema or microhemorrhages [14].
- **Enhanced sensitivity to susceptibility effects:** Higher field strength increases sensitivity to magnetic susceptibility effects [14]. This is critical for detecting ARIA-H, where hemosiderin deposits create susceptibility artifacts [18]. The enhanced sensitivity at 3T improves the visualization of microhemorrhages, which appear as hypointense areas on T2*-weighted or SWI sequences.
- **Higher spatial resolution:** At higher field strength, the intrinsically higher SNR can be traded for higher spatial resolution imaging. This means that the images can show finer details, which is essential for detecting small or subtle ARIA lesions. Better spatial resolution also helps in precisely localizing and characterizing the extent of ARIA-related changes in the brain [22].
- **Longer TE:**At higher field strengths, longer echo times can be used without compromising image quality. This is beneficial for T2*-weighted and SWI sequences, which rely on longer TEs to enhance susceptibility effects. Longer TEs at higher field strengths also improve the detection of hemosiderin deposits, making it easier to identify and quantify microhemorrhages [23].

Importance of consistency in MRI imaging parameters

MRI protocols for ARIA detection must be standardized. Since guidelines for use of MRI to detect ARIA when administering amyloid-targeting therapies typically include protocols for baseline imaging, regular monitoring, and managing detected abnormalities, it is crucial that there is consistency in imaging parameters.

It is ideal to use the same MRI field strength (e.g., 3T), the same MRI machine vendor (e.g., Siemens Healthineers), and the same scanner model for all serial exams of a patient [24]. Consistency in these factors helps ensure that images are comparable over time. In addition, using identical MRI sequences (i.e. either use T2*-weighted GRE or SWI) and the same sequence parameters (e.g., echo time, repetition time) across all exams ensures uniformity in the images obtained (Fig. 5) [24].

Consistency and standardization in imaging protocols are critical for accurately assessing and monitoring ARIA [24]. Variations in imaging parameters can lead to differences in image appearance, making it difficult to detect subtle changes or to compare images over time [24]. For example, the field strength of the MRI (e.g., 1.5T vs. 3T) has a significant impact on the detection of ARIA-H. Higher field strength enhances the sensitivity to magnetic susceptibility effects, making it easier to detect hemosiderin deposits and microhemorrhages. Consequently, field strength should not be changed during the course of baseline MRI and ARIA monitoring as this has direct impact on the detection of ARIA, particularly ARIA-H.

Similarly, different MRI vendors may have slight variations in how they generate and display images. These differences can affect the appearance of brain regions, particularly the occipital white matter. This variability can impact the detection and assessment of ARIA-E, where subtle changes in the white matter need to be accurately identified.

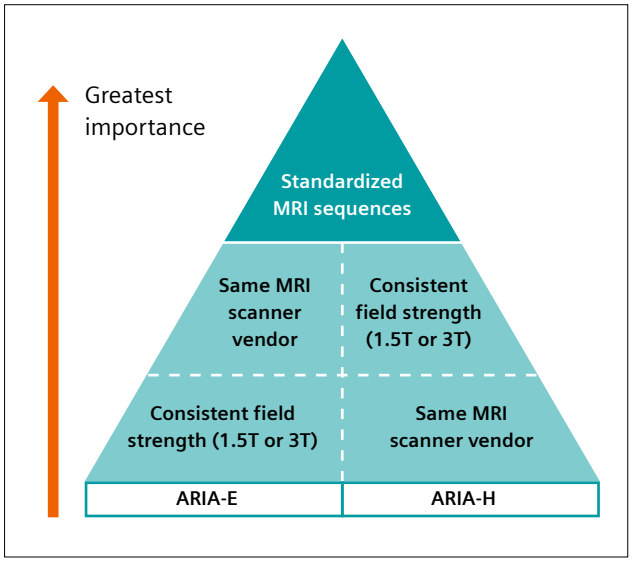

5 **Key factors impacting MR imaging of ARIA [24].** Maintaining consistency and standardization in MRI imaging parameters — such as using the same field strength, vendor, scanner model, and identical sequences with the same parameters — is crucial for the accurate assessment of ARIA over time [24]. Field strength particularly affects the detection of ARIA-H, while differences in MRI vendors can impact the appearance and detection of ARIA-E, especially in the occipital white matter [24]. Uniform imaging protocols help ensure reliable and comparable results across serial exams.

Optimization of MRI sequences for ARIA detection

MRI sequences must be optimized for the effective detection of ARIA for three key reasons:

1. **Subtle abnormalities:** ARIA often presents with subtle changes that can be easily missed without high sensitivity and resolution.
2. **Specificity:** ARIA-E and ARIA-H require different imaging characteristics for accurate detection.
3. **Consistency:** To monitor ARIA progression or resolution over time, consistent and optimized imaging protocols are essential.
4. **Rule out stroke:** To differentiate symptomatic ARIA-E from stroke, i.e. ischemia, a diffusion-weighted imaging (DWI) scan should be performed.

Optimized MRI sequences for ARIA-E detection

For ARIA-E detection, T2-weighted FLAIR sequences enhance the visibility of edema by suppressing the signal from cerebrospinal fluid, allowing better contrast of abnormal fluid accumulation in the brain parenchyma. In addition, DWI sequences help differentiate vasogenic edema (seen in ARIA-E) from cytotoxic edema (seen in acute infarct, i.e. stroke). ARIA-E do not show up as hyperintense areas in high b-value DWI while ischemic lesions do.

Optimized MRI sequences for ARIA-H detection

For ARIA-H detection, T2*-weighted GRE sequences are sensitive to magnetic susceptibility effects caused by blood breakdown products like hemosiderin. SWI provides enhanced sensitivity and spatial resolution for detecting small hemorrhages and hemosiderin deposits. Even small microbleeds appear as dark spots, providing greater detail than T2*-weighted GRE.

Clinical applications

MRI sequences must be optimized for ARIA detection to enhance sensitivity and specificity to the subtle changes associated with ARIA-E and ARIA-H. This involves using high field strength, selecting appropriate sequences, and adjusting sequence parameters. MRI sequences for ARIA monitoring can be found on the website of the American Society of Neuroradiology (ASNR) or directly downloaded from the MAGNETOM World website from Siemens Healthineers.
https://www.asnr.org/education-resources/alzheimers-webinar-series/ or
https://www.magnetomworld.siemens-healthineers.com/clinical-corner/protocols/neurology-neurography/asnr

Impact of MRI findings on treatment decision-making

MRI findings of ARIA-E and ARIA-H play a crucial role in treatment decision-making for patients receiving amyloid-targeting therapies.

Detection and monitoring

Baseline imaging: Before starting amyloid-targeting therapies, baseline MRI scans are performed to identify any pre-existing abnormalities [25]. This helps in distinguishing new ARIA findings from chronic changes.
Regular monitoring: Routine MRI scans are conducted during treatment to detect new or worsening ARIA-E and ARIA-H [17]. This regular monitoring helps in early detection and timely intervention.

ARIA-E assessment

Severity: Mild ARIA-E typically involves small areas of cortical-subcortical hyperintensity with mild gyral swelling. Mild cases might be monitored without immediate changes to therapy. With moderate to severe ARIA-E, larger areas of hyperintensity with significant mass effect or effusion indicate more severe edema [17]. These cases often require more immediate intervention (Fig. 6).
Treatment modifications: If moderate or severe ARIA-E is detected, treatment with amyloid-targeting therapy is often paused to prevent further complications. If the patient is symptomatic (e.g., headaches, confusion), additional treatments, such as corticosteroids, may be considered to reduce inflammation and edema [16]. Patients with ARIA-E typically undergo follow-up MRI scans after a pause in treatment to assess resolution. Once ARIA-E has resolved or significantly improved, therapy may be cautiously resumed, often at a lower dose.

ARIA-H assessment

Severity: Small, isolated hypointense spots (microhemorrhages) on T2*-weighted or SWI sequences might be monitored closely without immediate therapy changes [26]. Extensive or confluent areas of hypointensity indicating significant bleeding may necessitate more immediate and aggressive management (Fig. 6).
Treatment modifications: In cases of extensive ARIA-H, amyloid-targeting therapy is typically paused to prevent further bleeding. Although ARIA-H may be asymptomatic, any new neurological symptoms (e.g., seizures, focal neurological deficits) should be closely monitored and managed [16]. The presence of ARIA-H may lead to a re-evaluation of the risks versus benefits of continuing amyloid-targeting therapy. In some cases, therapy may be discontinued altogether if the risk is deemed too high.

ARIA management

MRI findings of ARIA-E and ARIA-H are integral to the management of patients on amyloid-targeting therapies. They help in assessing the severity of ARIA, guiding modifications in therapy, and ensuring patient safety. Regular monitoring and timely intervention based on MRI findings are essential to optimize treatment outcomes and minimize complications. Clinicians must follow established guidelines and protocols, such as those from the Food and Drug Administration (FDA) and other regulatory bodies, which provide recommendations on managing ARIA.

For Lecanemab, patients require a baseline MRI scan as well as follow-up scans before the 3rd, 5th, 7th, and 14th infusion. An additional follow-up MRI scan is recommended prior to the 26th infusion in patients who are APOE4 carriers or in those who showed evidence of ARIA (with or without symptoms) on earlier MRIs [27, 28].

ARIA-Class	Mild	Moderate	Severe
ARIA-E (Edema, effusion, exudate)	FLAIR hyperintensity measuring **<5** cm in one site	FLAIR hyperintensity measuring **5–10 cm**, or signal at **>1** site with each measuring **<10 cm**	FLAIR hyperintensity measuring **>10 cm** in one or more separate sites
ARIA-H (Microhemorrhages)	**1 to 4** new microhemorrhages	**5 to 9** new microhemorrhages	**10 or more** new microhemorrhages
ARIA-H (Superficial siderosis)	**1** focal area of superficial siderosis	**2** focal areas of superficial siderosis	**More than 2** focal areas of superficial siderosis

6 **ARIA severity grading scale.** ARIA can be categorized by radiographic severity as mild, moderate, or severe according to hyperintense signal measuring (ARIA-E) or the presence of new microhemorrhages or focal areas of superficial siderosis (ARIA-H) [14].

For Donanemab, patients also need a baseline scan and follow-up scans prior to the 2nd, 3rd, 4th, and 7th infusion. An additional follow-up MRI scan is recommended prior to the 12th infusion in higher-risk individuals (e.g., APOE4 carriers, patients with previous ARIA events earlier in treatment) [29].

ARIA is often asymptomatic and detected incidentally during routine MRI surveillance rather than through the presentation of symptoms. When ARIA does cause symptoms, they are usually unspecific and can include headaches, confusion, visual disturbances, visuospatial impairment, and apraxia. Although rare, some severe cases of ARIA have been reported, which required intensive care unit admissions due to significant symptoms. Typically, clinical symptoms of ARIA often resolve on their own when the amyloid-targeting treatment is paused or withdrawn. In some cases, based on the severity of ARIA, adjustments to the treatment dose or complete discontinuation may be necessary to manage symptoms and prevent further complications [11].

Mastering ARIA detection

As the prevalence of AD continues to rise, clinicians face a massive challenge in managing this complex and debilitating condition. The increasing burden of Alzheimer's care demands that healthcare professionals be well-prepared to navigate the multifaceted aspects of treatment and patient management. Central to this preparation is the integration of advanced diagnostic tools and monitoring techniques, particularly the detection and management of ARIA.

ARIA assessment, encompassing both ARIA-E and ARIA-H, is a critical component in the management of Alzheimer's patients undergoing amyloid-targeting therapies. Effective ARIA detection through MRI is essential for tailoring treatment plans, minimizing potential risks, and optimizing therapeutic outcomes. By staying vigilant in monitoring ARIA, clinicians can better address treatment-related complications, adjust therapies as needed, and ultimately improve the quality of care for patients. As the burden of AD grows, mastering ARIA detection and monitoring will be integral to ensuring that patients receive the safest and most effective treatment possible.

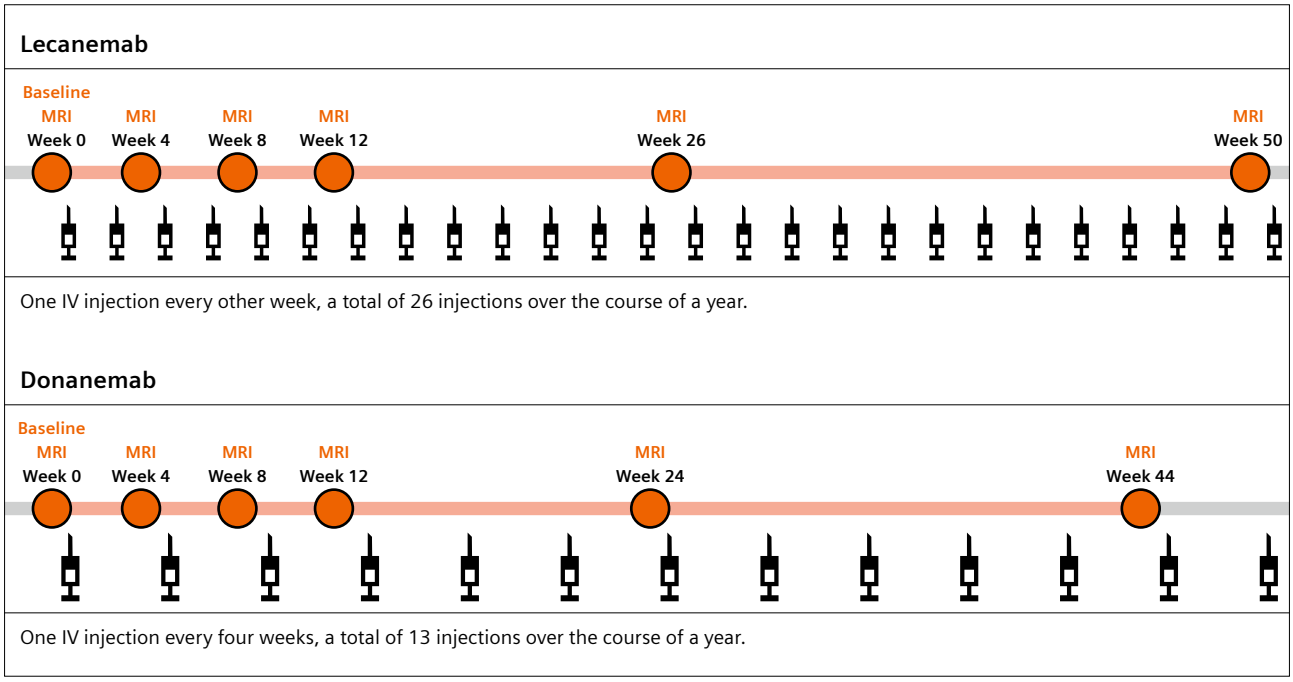

7 Recommended MRI Monitoring Schemes.

References

1 Faktenzentrale Demenz. https://www.dzne.de/aktuelles/hintergrund/faktenzentrale
2 Alzheimer's Disease and Dementia: What Healthcare Practitioners Need to Know. www.thedoctors.com/articles/alzheimers-disease-and-dementia-what-healthcare-practitioners-need-to-know/
3 2024 Alzheimer's disease facts and figures. Alzheimers Dement. 2024;20(5):3708-3821. https://alz-journals.onlinelibrary.wiley.com/doi/10.1002/alz.13809
4 Pathology of Alzheimer's Disease — an Overview | ScienceDirect Topics. Sciencedirect.com, 2012, https://www.sciencedirect.com/topics/medicine-and-dentistry/pathology-of-alzheimers-disease
5 Scheltens P, De Strooper B, Kivipelto M, Holstege H, Chételat G, Teunissen CE, et al. Alzheimer's disease. Lancet. 2021;397(10284):1577-1590. https://pmc.ncbi.nlm.nih.gov/articles/PMC8354300/
6 Ono K, Watanabe-Nakayama T. Aggregation and structure of amyloid β-protein. Neurochem Int. 2021;151:105208. https://www.sciencedirect.com/science/article/abs/pii/S0197018621002540?via%3Dihub
7 Selkoe DJ, Hardy J. The amyloid hypothesis of Alzheimer's disease at 25 years. EMBO Mol Med. 2016;8(6):595-608. https://pmc.ncbi.nlm.nih.gov/articles/PMC4888851/pdf/EMMM-8-595.pdf
8 Cummings JL, Zhou Y, Lee G, Zhong K, Fonseca J, Leisgang-Osse AM, et al. Alzheimer's disease drug development pipeline: 2025. Alzheimers Dement (N Y). 2025;11(2):e70098. https://doi.org/10.1002/trc2.70098
9 Roytman M, Mashriqi F, Al-Tawil K, Schulz PE, Zaharchuk G, Benzinger TLS, et al. Amyloid-Related Imaging Abnormalities: An Update. AJR Am J Roentgenol. 2023;220(4):562-574. https://www.ajronline.org/doi/10.2214/AJR.22.28461
10 2023 Alzheimer's disease facts and figures. Alzheimers Dement. 2023:1598-1695. https://alz-journals.onlinelibrary.wiley.com/doi/10.1002/alz.13016
11 Hampel H, Elhage A, Cho M, Apostolova LG, Nicoll JAR, Atri A. Amyloid-related imaging abnormalities (ARIA): radiological, biological and clinical characteristics. Brain. 2023;146(11):4414-4424. https://academic.oup.com/brain/article/146/11/4414/7191051
12 Gaillard, F. Amyloid Related Imaging Abnormalities (ARIA) | Radiology Reference Article | Radiopaedia.org. Radiopaedia, radiopaedia.org/articles/amyloid-related-imaging-abnormalities-aria
13 VandeVrede L, Gibbs DM, Koestler M, La Joie R, Ljubenkov PA, Provost K, et al. Symptomatic amyloid-related imaging abnormalities in an APOE ε4/ε4 patient treated with aducanumab. Alzheimers Dement (Amst). 2020;12(1):e12101. https://doi.org/10.1002/dad2.12101.
14 Cogswell PM, Barakos JA, Barkhof F, Benzinger TS, Jack CR Jr, Poussaint TY, et al. Amyloid-Related Imaging Abnormalities with Emerging Alzheimer Disease Therapeutics: Detection and Reporting Recommendations for Clinical Practice. AJNR Am J Neuroradiol. 2022;43(9):E19-E35. https://www.ajnr.org/content/early/2022/08/25/ajnr.A7586
15 Doran SJ, Sawyer RP. Risk factors in developing amyloid related imaging abnormalities (ARIA) and clinical implications. Front Neurosci. 2024;18:1326784. https://www.ncbi.nlm.nih.gov/pmc/articles/PMC10834650/
16 Withington CG, Turner RS. Amyloid-Related Imaging Abnormalities With Anti-amyloid Antibodies for the Treatment of Dementia Due to Alzheimer's Disease. Front Neurol. 2022;13:862369. www.ncbi.nlm.nih.gov/pmc/articles/PMC8985815/, https://doi.org/10.3389/fneur.2022.862369.
17 Agarwal A, Gupta V, Brahmbhatt P, Desai A, Vibhute P, Joseph-Mathurin N, et al. Amyloid-related Imaging Abnormalities in Alzheimer Disease Treated with Anti-Amyloid-β Therapy. Radiographics. 2023;43(9):e230009. https://doi.org/10.1148/rg.230009.
18 Barakos J, Purcell D, Suhy J, Chalkias S, Burkett P, Marsica Grassi C, et al. Detection and Management of Amyloid-Related Imaging Abnormalities in Patients with Alzheimer's Disease Treated with Anti-Amyloid Beta Therapy. J Prev Alzheimers Dis. 2022;9(2):211-220. https://doi.org/10.14283/jpad.2022.21.
19 Graves MJ. 3 T: the good, the bad and the ugly. Br J Radiol. 2022 Feb 1;95(1130):20210708. https://doi.org/10.1259/bjr.20210708.
20 Sarracanie M, Salameh N. Low-Field MRI: How Low Can We Go? A Fresh View on an Old Debate. Front Phys, 2020;8. https://doi.org/10.3389/fphy.2020.00172.
21 Caruso D, Zerunian M, De Santis D, Biondi T, Paolantonio P, Rengo M, et al. Magnetic Resonance of Rectal Cancer Response to Therapy: An Image Quality Comparison between 3.0 and 1.5 Tesla. Biomed Res Int. 2020;2020:9842732. www.ncbi.nlm.nih.gov/pmc/articles/PMC7576357/, https://doi.org/10.1155/2020/9842732.
22 Verma G, Balchandani P. Ultrahigh field MR Neuroimaging. Top Magn Reson Imaging. 2019;28(3):137-144. https://pmc.ncbi.nlm.nih.gov/articles/PMC6784841/
23 Vachha B, Huang SY. MRI with ultrahigh field strength and high-performance gradients: challenges and opportunities for clinical neuroimaging at 7 T and beyond. Eur Radiol Exp. 2021;5(1):35. https://doi.org/10.1186/s41747-021-00216-2.
24 Franceschi, AM. "Amyloid-Related Imaging Abnormalities (ARIA): An Update." Powerpoint and lecture presented at: ECR 2025; 27 Feb. 2025.
25 Yu FF. Invited Commentary: Radiologist's Role in Anti-Amyloid Therapy for Alzheimer Disease. Radiographics. 2023;43(9):e230205. doi:https://doi.org/10.1148/rg.230205
26 Haller S, Vernooij MW, Kuijer JPA, Larsson EM, Jäger HR, Barkhof F. Cerebral Microbleeds: Imaging and Clinical Significance. Radiology. 2018;287(1):11-28. https://pubs.rsna.org/doi/10.1148/radiol.2018170803. Accessed 21 Jan. 2021.
27 Cummings J, Apostolova L, Rabinovici GD, Atri A, Aisen P, Greenberg S, et al. Lecanemab: Appropriate Use Recommendations. J Prev Alzheimers Dis. 2023;10(3):362-377. https://doi.org/10.14283/jpad.2023.30
28 https://www.fda.gov/drugs/drug-safety-and-availability/fda-recommend-additional-earlier-mri-monitoring-patients-alzheimers-disease-taking-leqembi-lecanemab
29 Rabinovici GD, Selkoe DJ, Schindler SE, Aisen P, Apostolova LG, Atri A, et al. Donanemab: Appropriate use recommendations. J Prev Alzheimers Dis. 2025;12(5):100150. https://doi.org/10.1016/j.tjpad.2025.100150

access·ad

ADVANCING ALZHEIMER'S DISEASE CARE

Building pathways for timely diagnosis and equitable treatment of Alzheimer's disease

info@access-ad.org

@access-ad

COCIR Advancing Healthcare · efpia · EuropaBio The European Association for Bioindustries · MedTech Europe from diagnosis to cure · Vaccines Europe

innovative health initiative

Co-funded by the European Union

This project is supported by the Innovative Health Initiative Joint Undertaking (IHI JU) under grant agreement No 101253010. The JU receives support from the European Union's Horizon Europe research and innovation programme and COCIR, EFPIA, Europa Bio, MedTech Europe, and Vaccines Europe.

Beta-amyloid PET/CT imaging in the assessment for anti-amyloid monoclonal therapy

Jana Ivanidze, MD, PhD[1]; Misty Long, ARRT, RT(R)(N)[2]; Andrés Ricaurte-Fajardo, MD[1]; Mohammad Raza Khan, MPhys, MSc[2]; Lady Sawoszczyk, BS, CNMT[2]; Brett Muench, BS, ARRT(N)(CT)[1]

[1] IDepartment of Molecular Imaging and Therapeutics, New York-Presbyterian Hospital/Weill Cornell Medicine, New York, New York, USA
[2] Siemens Healthineers Molecular Imaging, Hoffman Estates, Illinois, USA

History

A 76-year-old female presented with memory impairment and was subsequently evaluated for cognitive decline by her primary care physician. Initial workup included ^{18}F-FDG PET/MRI and MRI brain without contrast, to determine the regional pattern of cortical ^{18}F-FDG avidity as well as to assess for any structural abnormalities, burden of microvascular ischemic change, and cerebral atrophy patterns (Figure 1). Per standard of care protocol, the patient was administered 7.5 mCi (277.1 MBq) of Fludeoxyglucose F 18 (^{18}F-FDG) Injection[1] followed by a 60-minute uptake. Statistical comparison of the ^{18}F-FDG PET data to a database of normal subjects confirmed a disproportionate

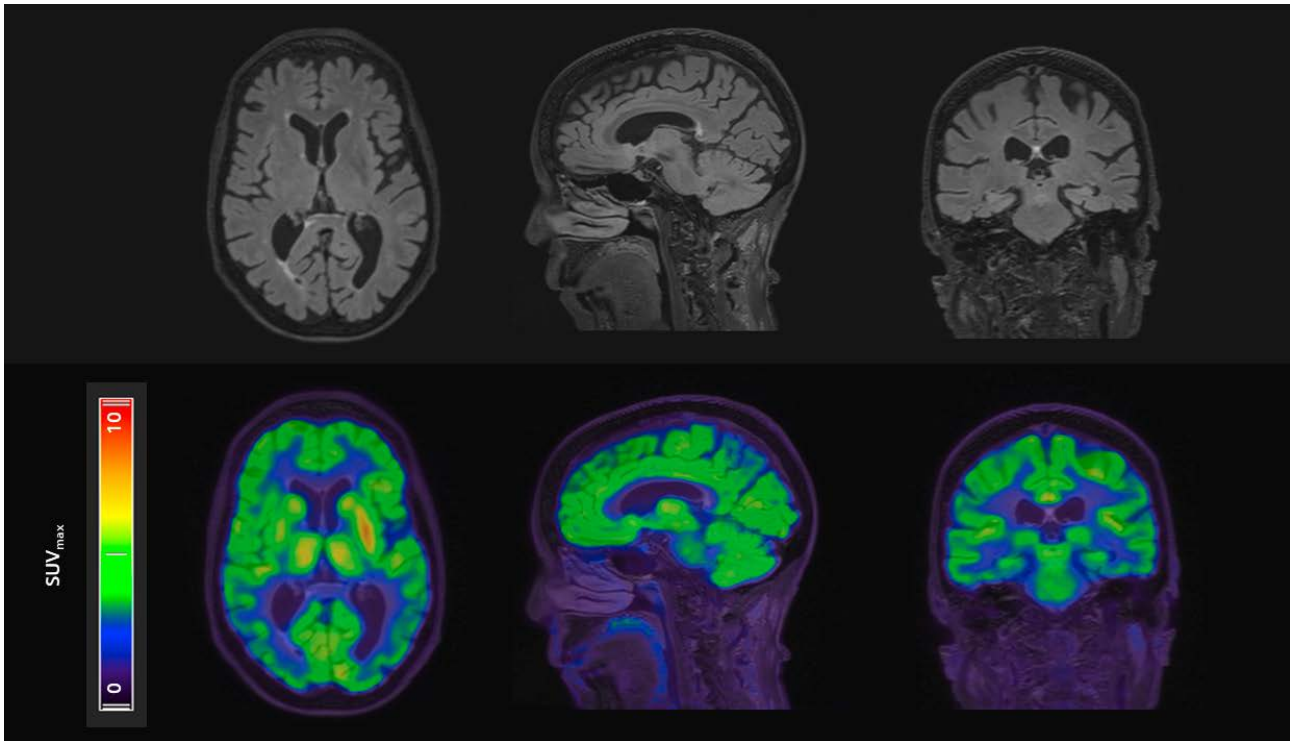

1 Axial, sagittal, and coronal MRI and PET/MRI images. Top row demonstrates axial, sagittal, and coronal T2FLAIR images; bottom row demonstrates matching attenuation-corrected PET fused to T2 FLAIR series, windowed at maximum SUV 0-10. There is disproportionate decrease in ^{18}F-FDG avidity in the bilateral, inferolateral parietal cortices, precuneus cortices, and posterior temporal cortices.

[1] Please see Indications and Important Safety Information for Fludeoxyglucose F 18 (^{18}F-FDG) Injection on page 14. For full Prescribing Information, please see pages 18–20.

decrease in ^{18}F-FDG avidity in the bilateral inferolateral parietal cortices, precuneus cortices, and posterior temporal cortices (Figure 2). Further assessment with analysis of cerebrospinal fluid (CSF) AD biomarkers was indeterminate, demonstrating borderline results (A-Beta42: 611.3 pg/ml, T-Tau: 301.5 pg/ml, P-Tau: 61.3 pg/ml, ATI: 1.03). Quantitative analysis confirmed a disproportionate decrease in ^{18}F-FDG avidity in the bilateral inferolateral parietal cortices, precuneus cortices, and posterior temporal cortices.

The patient was referred to a dementia specialist for further evaluation and beta-amyloid PET/CT imaging was performed. Ninety minutes following intravenous (IV) administration of 7.6 mCi (283 MBq) ^{18}F-Florbetaben, the patient underwent PET/CT imaging on Biograph mCT.

Findings

^{18}F-Florbetaben PET images in Figure 3 show increased tracer uptake in the entire cerebral gray matter, reflecting increased amyloid deposition with loss of normal gray-white matter contrast. There is diffuse avidity of the radiotracer in the cortical gray matter and white matter, with evidence of markedly increased ^{18}F-Florbetaben avidity throughout the bilateral lateral temporal cortices, frontal cortices, posterior cingulate/precuneus regions, and lateral parietal cortices, relative cortical tracer uptake score of 3 in all regions, compatible with overall brain amyloid plaque load score of 3.

syngo.MI Neuro Cortical Analysis uses the standard uptake ratio (SUVr) as an index of pathologic amyloid deposits in patients with suspected cognitive impairment. SUVr is defined as the ratio between selected cortical regions of interest (ROI), and, in this case, the cerebellar cortex as a reference. Here, *syngo*.MI Neuro Cortical Analysis demonstrates high global and regional cortico-cerebellar ratio (global SUVr: 2.27), which is significantly higher than the upper level of normal for amyloid burden based on the method by Barthel et al. (Figure 4). The method is based on a multi-center trial which demonstrated a threshold of greater than or equal to 1.57 SUVr, reflects pathological levels of amyloid accumulation associated with Alzheimer's disease (AD) [1]. In addition, the Centiloid (CL) score is 152.6, reflecting a high cortical beta-amyloid burden. Siemens Healthineers offers quantitative software on *syngo*.via for the accurate localization of cortical beta-amyloid distribution and quantification of brain PET images. *syngo*.MI Neuro DB Comparison enables physicians

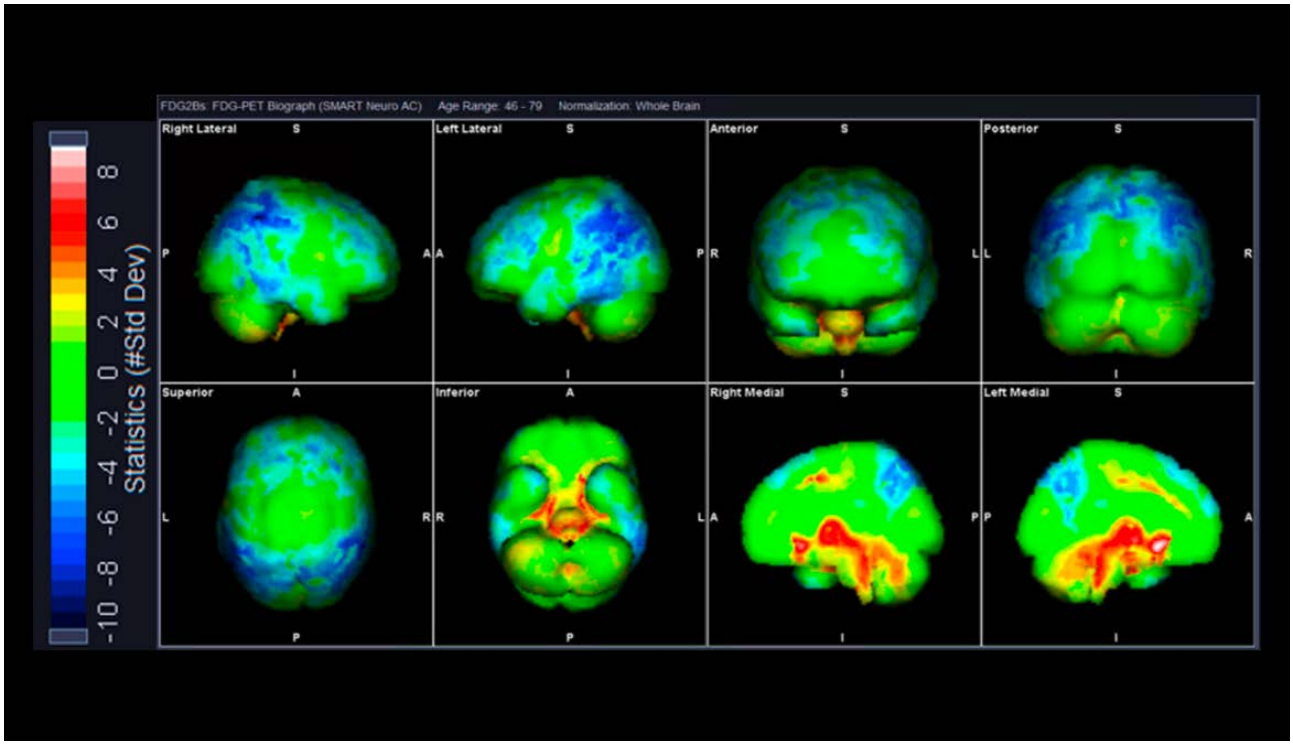

2 Database comparison of patient's PET to a reference database using *syngo*.MI Neuro DB Comparison (whole-brain intensity normalization, reference cohort age range: 46-79 years). Quantitative analysis confirmed a disproportionate decrease in ^{18}F-FDG avidity in the bilateral inferolateral parietal cortices, precuneus cortices, and posterior temporal cortices.

Fludeoxyglucose F 18 injection

INDICATIONS AND USAGE

Fludeoxyglucose F 18 Injection (^{18}F-FDG) is indicated for positron emission tomography (PET) imaging in the following settings:

- **Oncology:** For assessment of abnormal glucose metabolism to assist in the evaluation of malignancy in patients with known or suspected abnormalities found by other testing modalities, or in patients with an existing diagnosis of cancer.
- **Cardiology:** For the identification of left ventricular myocardium with residual glucose metabolism and reversible loss of systolic function in patients with coronary artery disease and left ventricular dysfunction, when used together with myocardial perfusion imaging.
- **Neurology:** For the identification of regions of abnormal glucose metabolism associated with foci of epileptic seizures.

IMPORTANT SAFETY INFORMATION

- **Radiation Risk:** Radiation-emitting products, including Fludeoxyglucose F 18 Injection, may increase the risk for cancer, especially in pediatric patients. Use the smallest dose necessary for imaging and ensure safe handling to protect the patient and health care worker.
- **Blood Glucose Abnormalities:** In the oncology and neurology setting, suboptimal imaging may occur in patients with inadequately regulated blood glucose levels. In these patients, consider medical therapy and laboratory testing to ensure at least two days of normoglycemia prior to Fludeoxyglucose F 18 Injection administration.
- **Adverse Reactions:** Hypersensitivity reactions with pruritus, edema, and rash have been reported. Have emergency resuscitation equipment and personnel immediately available.
- **Pediatric Use:** The safety and effectiveness of Fludeoxyglucose F 18 Injection in pediatric patients with epilepsy is established on the basis of studies in adult and pediatric patients. In pediatric patients with epilepsy, the recommended dose is 2.6 mCi. The optimal dose adjustment on the basis of body size or weight has not been determined.

In the oncology or cardiology settings, the safety and effectiveness of Fludeoxyglucose F 18 Injection have not been established in pediatric patients.

DOSAGE FORMS AND STRENGTHS

Multiple-dose 30 mL and 50 mL glass vial containing 0.74 to 7.40 GBq/mL (20 to 200 mCi/mL) Fludeoxyglucose F 18 Injection and 4.5 mg of sodium chloride with 0.1 to 0.5% w/w ethanol as a stabilizer (approximately 15 to 50 mL volume) for intravenous administration.

- Recommended dose for pediatric patients: Within the neurology setting, the recommended dose for pediatric patients is 2.6 mCi, as an intravenous injection. The optimal dose adjustment on the basis of body size or weight has not been determined.

Fludeoxyglucose F 18 Injection is manufactured and distributed by PETNET Solutions, Inc., 810 Innovation Drive, Knoxville, TN 37932

to compare the patient's cortical beta-amyloid distribution with a normal reference database and determine region-specific z-scores in a heat map as shown in Figure 5. Additionally, *syngo*.MI Neuro Cortical Analysis enables the calculation of cortico-cerebellar SUVr. Furthermore, the CL method allows standardized evaluation of beta-amyloid PET results, which has demonstrated utility in prospective therapeutic clinical trials [2]. The CL scale is referenced from 0 to 100, where the 0 CL represents young healthy amyloid-negative controls, and the 100 CL represents amyloid-positive patients with confirmed diagnosis of AD. However, scores can fall above or below 0-100 range. These quantitative metrics of beta-amyloid PET are likely to be incorporated in clinical reports in the near future. MRI fusion, normalization to a standard reference template, and the ability to create a custom normal database further enhance *syngo*.MI Neurology's capabilities. A robust solution for both visual interpretation and quantification, adding further reader confidence to a clinical read.

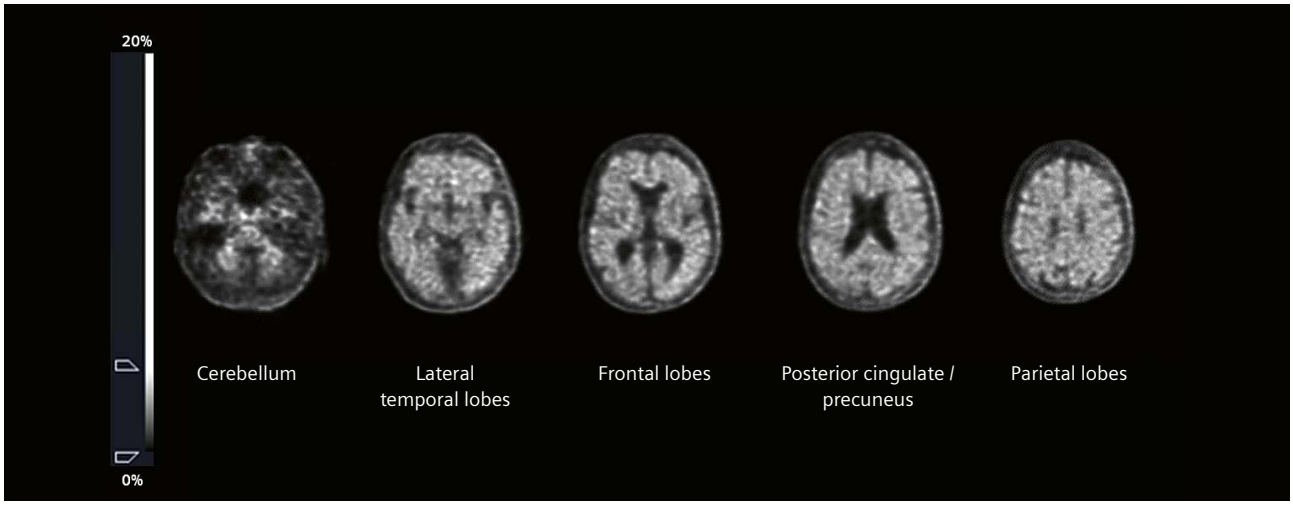

3 Axial ^{18}F-Florbetaben beta-amyloid PET images show increased tracer uptake throughout the entire cerebral gray matter, including the bilateral lateral temporal cortices, frontal cortices, posterior cingulate/precuneus regions, and lateral parietal cortices, with loss of normal gray-white matter differentiation, reflecting diffuse cortical beta-amyloid deposition.

4 Axial, coronal, and sagittal ^{18}F-Florbetaben PET images fused with MRI with *syngo*.MI Neuro Cortical Analysis demonstrates high global and regional cortico-cerebellar ratio (global SUVr: 2.27). CL score is 152.6, reflecting a high cortical beta-amyloid burden.

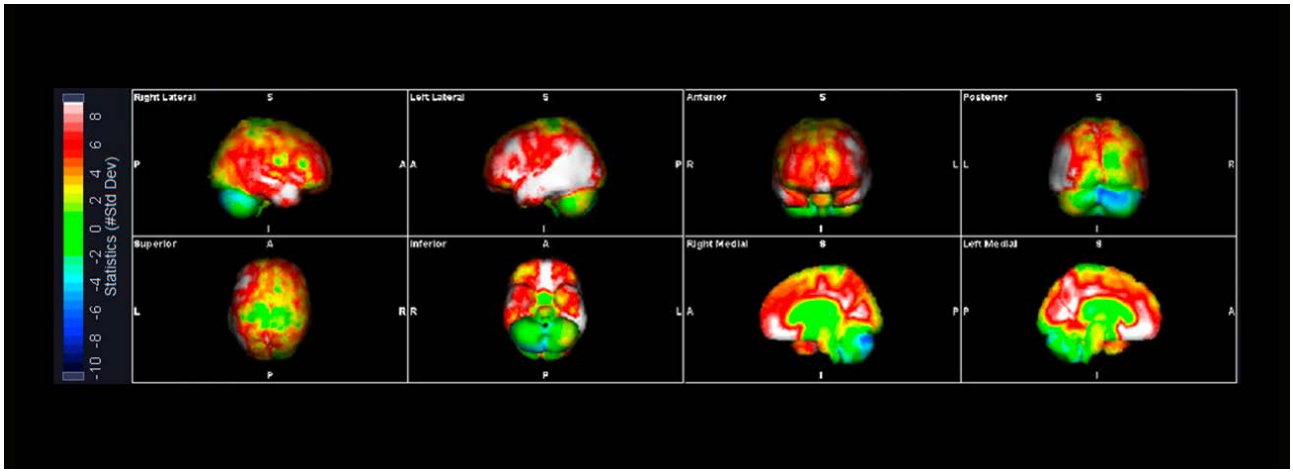

5 *syngo*.MI Neuro DB Comparison, 3D Stereotatic Surface Projection (3D-SSP).

Subsequent apolipoprotein E (APOE) gene testing revealed the patient to be a carrier of the APOE4 allele and APOE3 allele genotype, which is associated with an increased risk of AD. Positive confirmation of beta-amyloid burden derived from ^{18}F-Florbetaben PET/CT imaging made the patient eligible for anti-amyloid monoclonal antibody treatment using Lecanumab. As a requirement for therapy monitoring, MRI was obtained to evaluate for Amyloid Related Imaging Abnormalities ARIA). While most adverse events are asymptomatic, carriers of APOE4 are at higher risk for ARIA. In this patient, baseline MRI demonstrated no acute abnormalities; there was a mild burden of chronic microvascular ischemic changes and no evidence of chronic microhemorrhages. After initiation of Lecanemab therapy, subsequent surveillance MRI revealed no interval change, including no evidence of ARIA-H (microhemorrhages) or ARIA-E (edema), allowing the patient to proceed with subsequent therapeutic doses of Lecanemab for the treatment of AD as per standard of care.

Discussion

Molecular imaging is a key component in the management of patients with suspected AD. Specifically, brain PET imaging with ^{18}F-FDG allows visualization of altered patterns of cortical metabolism, thereby providing important differential diagnostic considerations. Amyloid-targeted PET allows visualization of cortical beta-amyloid distribution, and thereby, provides an estimate of beta-amyloid neuritic plaque density in patients with cognitive impairment who are being evaluated for AD and other causes of cognitive decline [3]. Most notably, confirmation of presence of beta-amyloid pathology prior to initiating treatment is required by the label to qualify for anti-amyloid monoclonal antibody treatment in patients with mild cognitive impairment (MCI) or mild dementia stage of AD [2]. Currently, there are two approaches available for the evaluation of cortical beta-amyloid plaque burden: CSF analysis via lumbar puncture, also known as a spinal tap, and beta-amyloid PET imaging. Importantly, compared to lumbar puncture, PET imaging is minimally invasive to the patient.

Along with the visual interpretation, PET imaging allows quantitative assessment of the geographic distribution of cortical beta-amyloid plaque deposition. Both SUVr and CL scale assessments are widely adopted in current amyloid PET studies, including anti-amyloid therapy trials and FDA-approved therapies [2]. In addition to current standard clinical practice interpretation of a positive or negative scan, gray versus white matter visual assessment, quantitative evaluation using database comparison, cortico-cerebellar SUVr, and CL scale has the potential of optimizing patient selection and monitoring for amyloid-targeted therapy.

Examination protocol

Scanner: Biograph mMR

PET		MR	
Injected dose	7.5 mCi (277 MBq) ^{18}F-Fludeoxyglucose	Sequence	3D T1 MPRAGE, 3D T2 FLAIR, DWI
Post-injection delay	60 minutes	Slice thickness	1.0 mm
Acquisition	1 bed position/20 minutes per bed Total scan time: 20 minutes		
Reconstruction	344 x 344 matrix, PSF+OSEM, 3i21s, Gaussian filter 2		

Scanner: Biograph mCT

PET		CT	
Injected dose	7.6 mCi (283 MBq) ^{18}F-Florbetaben	Tube voltage	120 kV
Post-injection delay	90 minutes	Tube current	96 mAs
Acquisition	1 bed position/20 minutes per bed Total scan time: 20 minutes	Slice collimation	1.5 mm
Reconstruction	440 x 440 matrix, PSF+TOF, 5i21s, Gaussian filter 2	Slice thickness	3.0 mm

Conclusion

Anti-amyloid therapy has the potential to slow down the progression of cognitive decline in patients with AD pathology. Beta-amyloid PET has thus become an important component in AD management and selection of patients for amyloid-targeted therapy. Not only is amyloid PET imaging non-invasive (compared to CSF analysis, which requires lumbar puncture), it also allows a quantitative, geographic assessment of cortical beta-amyloid burden as opposed to global values provided in CSF biomarker analysis. Additionally, CSF analysis may often be inconclusive as in this clinical example. Thus, beta-amyloid PET imaging represents a reliable, non-invasive diagnostic modality that allows the evaluation of patients for anti-amyloid therapeutic treatment and the assessment of the impact of therapy on cortical amyloid burden.

References

1 Barthel H, et al. Cerebral amyloid-β PET with florbetaben (18F) in patients with Alzheimer's disease and healthy controls: a multicentre phase 2 diagnostic study. Lancet Neurol. 2011;10(5):424-35. doi:10.1016/S1474-4422(11)70077-1.
2 Eisai and Biogen. LEQEMBI. Prescribing Information. Available at https://www.leqembi.com/-/media/Files/Leqembi/Prescribing-Information.pdf?hash=77aa4a86-b786-457a-b894-01de37199024.
3 Life Molecular Imaging. NEURACEQ. Prescribing Information. Available at https://neuraceq.com/wp-content/uploads/PRESCRIBING-INFORMATION.pdf.

HIGHLIGHTS OF PRESCRIBING INFORMATION

These highlights do not include all the information needed to use Fludeoxyglucose F 18 Injection safely and effectively. See full prescribing information for Fludeoxyglucose F 18 Injection.

Fludeoxyglucose F 18 Injection, USP
For intravenous use
Initial U.S. Approval: 2005

INDICATIONS AND USAGE

Fludeoxyglucose F 18 Injection is indicated for positron emission tomography (PET) imaging in the following settings:

- Oncology: For assessment of abnormal glucose metabolism to assist in the evaluation of malignancy in patients with known or suspected abnormalities found by other testing modalities, or in patients with an existing diagnosis of cancer.
- Cardiology: For the identification of left ventricular myocardium with residual glucose metabolism and reversible loss of systolic function in patients with coronary artery disease and left ventricular dysfunction, when used together with myocardial perfusion imaging.
- Neurology: For the identification of regions of abnormal glucose metabolism associated with foci of epileptic seizures (1).

DOSAGE AND ADMINISTRATION

Fludeoxyglucose F 18 Injection emits radiation. Use procedures to minimize radiation exposure. Screen for blood glucose abnormalities.

- In the oncology and neurology settings, instruct patients to fast for 4 to 6 hours prior to the drug's injection. Consider medical therapy and laboratory testing to assure at least two days of normoglycemia prior to the drug's administration (5.2).
- In the cardiology setting, administration of glucose-containing food or liquids (e.g., 50 to 75 grams) prior to the drug's injection facilitates localization of cardiac ischemia (2.3).

Aseptically withdraw Fludeoxyglucose F 18 Injection from its container and administer by intravenous injection (2).

The recommended dose:

- for adults is 5 to 10 mCi (185 to 370 MBq), in all indicated clinical settings (2.1).
- for pediatric patients is 2.6 mCi in the neurology setting (2.2).

Initiate imaging within 40 minutes following drug injection; acquire static emission images 30 to 100 minutes from time of injection (2).

DOSAGE FORMS AND STRENGTHS

Multi-dose 30mL and 50mL glass vial containing 0.74 to 7.40 GBq/mL (20 to 200 mCi/mL) Fludeoxyglucose F 18 Injection and 4.5mg of sodium chloride with 0.1 to 0.5% w/w ethanol as a stabilizer (approximately 15 to 50 mL volume) for intravenous administration (3).

CONTRAINDICATIONS

None.

WARNINGS AND PRECAUTIONS

- Radiation risks: use smallest dose necessary for imaging (5.1).
- Blood glucose abnormalities: may cause suboptimal imaging (5.2).

ADVERSE REACTIONS

Hypersensitivity reactions have occurred; have emergency resuscitation equipment and personnel immediately available (6).

To report SUSPECTED ADVERSE REACTIONS, contact PETNET Solutions, Inc. at 877-473-8638 or FDA at 1-800-FDA-1088 or www.fda.gov/medwatch.

USE IN SPECIFIC POPULATIONS

- Lactation: Temporarily discontinue breastfeeding. A lactating woman should pump and discard breastmilk for 9 hours after Fludeoxyglucose F 18 Injection (8.2).
- Pediatric Use: Safety and effectiveness in pediatric patients have not been established in the oncology and cardiology settings (8.4).

See 17 for PATIENT COUNSELING INFORMATION

Revised: 10/2019

FULL PRESCRIBING INFORMATION: CONTENTS*

* Sections or subsections omitted from the full prescribing information are not listed.

FULL PRESCRIBING INFORMATION

1 INDICATIONS AND USAGE

Fludeoxyglucose F 18 Injection is indicated for positron emission tomography (PET) imaging in the following settings:

1.1 Oncology

For assessment of abnormal glucose metabolism to assist in the evaluation of malignancy in patients with known or suspected abnormalities found by other testing modalities, or in patients with an existing diagnosis of cancer.

1.2 Cardiology

For the identification of left ventricular myocardium with residual glucose metabolism and reversible loss of systolic function in patients with coronary artery disease and left ventricular dysfunction, when used together with myocardial perfusion imaging.

1.3 Neurology

For the identification of regions of abnormal glucose metabolism associated with foci of epileptic seizures.

2 DOSAGE AND ADMINISTRATION

Fludeoxyglucose F 18 Injection emits radiation. Use procedures to minimize radiation exposure. Calculate the final dose from the end of synthesis (EOS) time using proper radioactive decay factors. Assay the final dose in a properly calibrated dose calibrator before administration to the patient *[see Description (11.2)]*.

2.1 Recommended Dose for Adults

Within the oncology, cardiology and neurology settings, the recommended dose for adults is 5 to 10 mCi (185 to 370 MBq) as an intravenous injection.

2.2 Recommended Dose for Pediatric Patients

Within the neurology setting, the recommended dose for pediatric patients is 2.6 mCi, as an intravenous injection. The optimal dose adjustment on the basis of body size or weight has not been determined *[see Use in Special Populations (8.4)]*.

2.3 Patient Preparation

- To minimize the radiation absorbed dose to the bladder, encourage adequate hydration. Encourage the patient to drink water or other fluids (as tolerated) in the 4 hours before their PET study.
- Encourage the patient to void as soon as the imaging study is completed and as often as possible thereafter for at least one hour.
- Screen patients for clinically significant blood glucose abnormalities by obtaining a history and/or laboratory tests *[see Warnings and Precautions (5.2)]*. Prior to Fludeoxyglucose F 18 PET imaging in the oncology and neurology settings, instruct patient to fast for 4 to 6 hours prior to the drug's injection.
- In the cardiology setting, administration of glucose-containing food or liquids (e.g., 50 to 75 grams) prior to Fludeoxyglucose F 18 Injection facilitates localization of cardiac ischemia.

2.4 Radiation Dosimetry

The estimated human absorbed radiation doses (rem/mCi) to a newborn (3.4 kg), 1-year old (9.8 kg), 5-year old (19 kg), 10-year old (32 kg), 15-year old (57 kg), and adult (70 kg) from intravenous administration of Fludeoxyglucose F 18 Injection are shown in Table 1. These estimates were calculated based on human[2] data and using the data published by the International Commission on Radiological Protection[4] for Fludeoxyglucose ^{18}F. The dosimetry data show that there are slight variations in absorbed radiation dose for various organs in each of the age groups. These dissimilarities in absorbed radiation dose are due to developmental age variations (e.g., organ size, location, and overall metabolic rate for each age group). The identified critical organs (in descending order) across all age groups evaluated are the urinary bladder, heart, pancreas, spleen, and lungs.

Table 1. Estimated Absorbed Radiation Doses (rem/mCi) After Intravenous Administration of Fludeoxyglucose F 18 Injection[a]

Organ	Newborn (3.4 kg)	1-year old (9.8 kg)	5-year old (19 kg)	10-year old (32 kg)	15-year old (57 kg)	Adult (70 kg)
Bladder wall[b]	4.3	1.7	0.93	0.60	0.40	0.32
Heart wall	2.4	1.2	0.70	0.44	0.29	0.22
Pancreas	2.2	0.68	0.33	0.25	0.13	0.096
Spleen	2.2	0.84	0.46	0.29	0.19	0.14
Lungs	0.96	0.38	0.20	0.13	0.092	0.064
Kidneys	0.81	0.34	0.19	0.13	0.089	0.074
Ovaries	0.80	0.8	0.19	0.11	0.058	0.053
Uterus	0.79	0.35	0.19	0.12	0.076	0.062
LLI wall *	0.69	0.28	0.15	0.097	0.060	0.051
Liver	0.69	0.31	0.17	0.11	0.076	0.058
Gallbladder wall	0.69	0.26	0.14	0.093	0.059	0.049
Small intestine	0.68	0.29	0.15	0.096	0.060	0.047
ULI wall **	0.67	0.27	0.15	0.090	0.057	0.046
Stomach wall	0.65	0.27	0.14	0.089	0.057	0.047
Adrenals	0.65	0.28	0.15	0.095	0.061	0.048
Testes	0.64	0.27	0.14	0.085	0.052	0.041
Red marrow	0.62	0.26	0.14	0.089	0.057	0.047
Thymus	0.61	0.26	0.14	0.086	0.056	0.044
Thyroid	0.61	0.26	0.13	0.080	0.049	0.039
Muscle	0.58	0.25	0.13	0.078	0.049	0.039
Bone surface	0.57	0.24	0.12	0.079	0.052	0.041
Breast	0.54	0.22	0.11	0.068	0.043	0.034
Skin	0.49	0.20	0.10	0.060	0.037	0.030
Brain	0.29	0.13	0.09	0.078	0.072	0.070
Other tissues	0.59	0.25	0.13	0.083	0.052	0.042

[a] MIRDOSE 2 software was used to calculate the radiation absorbed dose.
[b] The dynamic bladder model with a uniform voiding frequency of 1.5 hours was used.
* LLI = lower large intestine; ** ULI = upper large intestine

2.5 Radiation Safety – Drug Handling

- Use waterproof gloves, effective radiation shielding, and appropriate safety measures when handling Fludeoxyglucose F 18 Injection to avoid unnecessary radiation exposure to the patient, occupational workers, clinical personnel and other persons.
- Radiopharmaceuticals should be used by or under the control of physicians who are qualified by specific training and experience in the safe use and handling of radionuclides, and whose experience and training have been approved by the appropriate governmental agency authorized to license the use of radionuclides.
- Calculate the final dose from the end of synthesis (EOS) time using proper radioactive decay factors. Assay the final dose in a properly calibrated dose calibrator before administration to the patient *[see Description (11.2)]*.
- The dose of Fludeoxyglucose F 18 used in a given patient should be minimized consistent with the objectives of the procedure, and the nature of the radiation detection devices employed.

2.6 Drug Preparation and Administration

- Calculate the necessary volume to administer based on calibration time and dose.
- Aseptically withdraw Fludeoxyglucose F 18 Injection from its container.
- Inspect Fludeoxyglucose F 18 Injection visually for particulate matter and discoloration before administration, whenever solution and container permit.
- Do not administer the drug if it contains particulate matter or discoloration; dispose of these unacceptable or unused preparations in a safe manner, in compliance with applicable regulations.
- Use Fludeoxyglucose F 18 Injection within 12 hours from the EOS.

2.7 Imaging Guidelines

- Initiate imaging within 40 minutes following Fludeoxyglucose F 18 Injection administration.
- Acquire static emission images 30 to 100 minutes from the time of injection.

3 DOSAGE FORMS AND STRENGTHS

Multiple-dose 30 mL and 50 mL glass vial containing 0.74 to 7.40 GBq/mL (20 to 200 mCi/mL) of Fludeoxyglucose F 18 Injection and 4.5 mg of sodium chloride with 0.1 to 0.5% w/w ethanol as a stabilizer (approximately 15 to 50 mL volume) for intravenous administration.

4 CONTRAINDICATIONS

None.

5 WARNINGS AND PRECAUTIONS

5.1 Radiation Risks

Radiation-emitting products, including Fludeoxyglucose F 18 Injection, may increase the risk for cancer, especially in pediatric patients. Use the smallest dose necessary for imaging and ensure safe handling to protect the patient and health care worker *[see Dosage and Administration (2.5)]*.

5.2 Blood Glucose Abnormalities

In the oncology and neurology setting, suboptimal imaging may occur in patients with inadequately regulated blood glucose levels. In these patients, consider medical therapy and laboratory testing to assure at least two days of normoglycemia prior to Fludeoxyglucose F 18 Injection administration.

6 ADVERSE REACTIONS

Hypersensitivity reactions with pruritus, edema and rash have been reported in the post-marketing setting. Have emergency resuscitation equipment and personnel immediately available.

7 DRUG INTERACTIONS

The interactions of Fludeoxyglucose F 18 Injection with other drugs taken by patients undergoing PET imaging has not been studied.

8 USE IN SPECIFIC POPULATIONS

8.1 Pregnancy

Risk Summary

Data from published case series and case reports describe Fludeoxyglucose F 18 Injection crossing the placenta with uptake by the fetus (see Data). All radiopharmaceuticals have the potential to cause fetal harm depending on the fetal stage of development and the magnitude of the radiation dose. However, published studies that describe Fludeoxyglucose F 18 Injection use in pregnant women have not identified a risk of drug-associated major birth defects, miscarriage, or adverse maternal or fetal outcomes. If considering Fludeoxyglucose F 18 Injection administration to a pregnant woman, inform the patient about the potential for adverse pregnancy outcomes based on the radiation dose from Fludeoxyglucose F 18 Injection and the gestational timing of exposure. The estimated background risk of major birth defects and miscarriage for the indicated population is unknown. All pregnancies have a background risk of birth defect, loss, or other adverse outcomes. In the U.S. general population, the estimated background risk of major birth defects and miscarriage in clinically recognized pregnancies are 2-4% and 15-20%, respectively.

Data

Human Data

Data from published case series and case reports describe Fludeoxyglucose F 18 Injection crossing the placental barrier and visualization of radioactivity throughout the body of the fetus. The estimated fetal absorbed radiation dose from the maximum labeled dose (370 MBq) of Fludeoxyglucose F 18 was 10 mGy with first trimester exposure to PET alone and 20 mGy with first trimester exposure to PET/CT scan combination. Long-term adverse radiation effects to a child exposed to Fludeoyxglucose F 18 Injection in utero are unknown. No adverse fetal effects or radiation-related risks have been identified for diagnostic procedures involving less than 50 mGy, which represents less than 20 mGy fetal doses.

8.2 Lactation

Risk Summary

A published case report and case series show the presence of Fludeoxyglucose F 18 Injection in human milk following administration. There are no data on the effects of Fludeoxyglucose F 18 Injection on the breastfed infant or the effects on milk production. Exposure of Fludeoxyglucose F 18 Injection to a breastfed infant can be minimized by temporary discontinuation of breastfeeding (see Clinical Considerations). The developmental and health benefits of breastfeeding should be considered along with the mother's clinical need for Fludeoxyglucose F 18 Injection, any potential adverse effects on the breastfed child from Fludeoxyglucose F 18 Injection or from the underlying maternal condition.

Clinical Considerations

To decrease radiation exposure to the breastfed infant, advise a lactating woman to pump and discard breastmilk and avoid close (breast) contact with the infant for at least 9 hours after the administration of Fludeoxyglucose F 18 Injection.

8.4 Pediatric Use

The safety and effectiveness of Fludeoxyglucose F 18 Injection in pediatric patients with epilepsy is established on the basis of studies in adult and pediatric patients. In pediatric patients with epilepsy, the recommended dose is 2.6 mCi. The optimal dose adjustment on the basis of body size or weight has not been determined. In the oncology or cardiology settings, the safety and effectiveness of Fludeoxyglucose F 18 Injection have not been established in pediatric patients.

11 DESCRIPTION

11.1 Chemical Characteristics

Fludeoxyglucose F 18 Injection is a positron emitting radiopharmaceutical that is used for diagnostic purposes in conjunction with positron emission tomography (PET) imaging. The active ingredient 2-deoxy-2-[^{18}F]fluoro-D-glucose has the molecular formula of $C_6H_{11}{}^{18}FO_5$ with a molecular weight of 181.26, and has the following chemical structure:

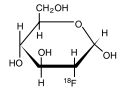

Fludeoxyglucose F 18 Injection is provided as a ready to use sterile, pyrogen free, clear, colorless solution. Each mL contains between 0.740 to 7.40GBq (20.0 to 200 mCi) of 2-deoxy-2-[^{18}F]fluoro-D-glucose at the EOS, 4.5 mg of sodium chloride and 0.1 to 0.5% w/w ethanol as a stabilizer. The pH of the solution is between 4.5 and 7.5. The solution is packaged in a multiple-dose glass vial and does not contain any preservative.

11.2 Physical Characteristics

Fluorine F 18 has a physical half-life of 109.7 minutes and decays to Oxygen O 16 (stable) by positron decay. The principal photons useful for imaging are the dual 511 keV "annihilation" gamma photons, that are produced and emitted simultaneously in opposite direction when the positron interacts with an electron (Table 2).

Table 2. Principal Radiation Emission Data for Fluorine F 18

Radiation/Emission	% Per Disintegration	Mean Energy
Positron (β+)	96.73	249.8 keV
Gamma (±)*	193.46	511.0 keV

*Produced by positron annihilation

From: Kocher, D.C. Radioactive Decay Tables DOE/TIC-I 1026, 89 (1981)

The specific gamma ray constant (point source air kerma coefficient) for fluorine F 18 is 5.7 R/hr/mCi (1.35 x 10^{-6} Gy/hr/kBq) at 1 cm. The half-value layer (HVL) for the 511 keV photons is 4 mm lead (Pb). The range of attenuation coefficients for this radionuclide as a function of lead shield thickness is shown in Table 3. For example, the interposition of an 8 mm thickness of Pb, with a coefficient of attenuation of 0.25, will decrease the external radiation by 75%.

Table 3. Radiation Attenuation of 511 keV Photons by lead (Pb) shielding

Shield thickness (Pb) mm	Coefficient of attenuation
0	0.00
4	0.50
8	0.25
13	0.10
26	0.01
39	0.001
52	0.0001

For use in correcting for physical decay of this radionuclide, the fractions remaining at selected intervals after calibration are shown in Table 4.

Table 4. Physical Decay Chart for Fluorine F 18

Minutes	Fraction Remaining
0*	1.000
15	0.909
30	0.826
60	0.683
110	0.500
220	0.250

*calibration time

12 CLINICAL PHARMACOLOGY

12.1 Mechanism of Action

Fludeoxyglucose F 18 is a glucose analog that concentrates in cells that rely upon glucose as an energy source, or in cells whose dependence on glucose increases under pathophysiological conditions. Fludeoxyglucose F 18 is transported through the cell membrane by facilitative glucose transporter proteins and is phosphorylated within the cell to [^{18}F] FDG-6-phosphate by the enzyme hexokinase. Once phosphorylated it cannot exit until it is dephosphorylated by glucose-6-phosphatase. Therefore, within a given tissue or pathophysiological process, the retention and clearance of Fludeoxyglucose F 18 reflect a balance involving glucose transporter, hexokinase and glucose-6-phosphatase activities. F 18 is used to assess glucose metabolism.

In comparison to background activity of the specific organ or tissue type, regions of decreased or absent uptake of Fludeoxyglucose F 18 reflect the decrease or absence of glucose metabolism. Regions of increased uptake of Fludeoxyglucose F 18 reflect greater than normal rates of glucose metabolism.

12.2 Pharmacodynamics

Fludeoxyglucose F 18 Injection is rapidly distributed to all organs of the body after intravenous administration. After background clearance of Fludeoxyglucose F 18 Injection, optimal PET imaging is generally achieved between 30 to 40 minutes after administration.

In cancer, the cells are generally characterized by enhanced glucose metabolism partially due to (1) an increase in activity of glucose transporters, (2) an increased rate of phosphorylation activity, (3) a reduction of phosphatase activity or, (4) a dynamic alteration in the balance among all these processes. However, glucose metabolism of cancer as reflected by Fludeoxyglucose F 18 accumulation shows considerable variability. Depending on tumor type, stage, and location, Fludeoxyglucose F 18 accumulation may be increased, normal, or decreased. Also, inflammatory cells can have the same variability of uptake of Fludeoxyglucose F 18.

In the heart, under normal aerobic conditions, the myocardium meets the bulk of its energy requirements by oxidizing free fatty acids. Most of the exogenous glucose taken up by the myocyte is converted into glycogen. However, under ischemic conditions, the oxidation of free fatty acids decreases, exogenous glucose becomes the preferred myocardial substrate, glycolysis is stimulated, and glucose taken up by the myocyte is metabolized immediately instead of being converted into glycogen. Under these conditions, phosphorylated Fludeoxyglucose F 18 accumulates in the myocyte and can be detected with PET imaging.

In the brain, cells normally rely on aerobic metabolism. In epilepsy, the glucose metabolism varies. Generally, during a seizure, glucose metabolism increases. Interictally, the seizure focus tends to be hypometabolic.

12.3 Pharmacokinetics

Distribution: In four healthy male volunteers, receiving an intravenous administration of 30 seconds induration, the arterial blood level profile for Fludeoxyglucose F 18 decayed triexponentially. The effective half-life ranges of the three phases were 0.2 to 0.3 minutes, 10 to 13 minutes with a mean and standard deviation (STD) of 11.6 (±) 1.1 min, and 80 to 95 minutes with a mean and STD of 88 (±) 4 min.

Plasma protein binding of Fludeoxyglucose F 18 has not been studied.

Metabolism: Fludeoxyglucose F 18 is transported into cells and phosphorylated to [^{18}F]-FDG-6-phosphate at a rate proportional to the rate of glucose utilization within that tissue. [^{18}F]-FDG-6-phosphate presumably is metabolized to 2-deoxy-2-[^{18}F]fluoro-6-phospho-D-mannose([^{18}F]FDM-6-phosphate).

Fludeoxyglucose F 18 Injection may contain several impurities (e.g., 2-deoxy-2-chloro-D-glucose (ClDG)). Biodistribution and metabolism of ClDG are presumed to be similar to Fludeoxyglucose F 18 and would be expected to result in intracellular formation of 2-deoxy-2-chloro-6-phospho-D-glucose (ClDG-6-phosphate) and 2-deoxy-2-chloro-6-phospho-D-mannose (ClDM-6-phosphate). The phosphorylated deoxyglucose compounds are dephosphorylated and the resulting compounds (FDG, FDM, ClDG, and ClDM) presumably leave cells by passive diffusion. Fludeoxyglucose F 18 and related compounds are cleared from non-cardiac tissues within 3 to 24 hours after administration. Clearance from the cardiac tissue may require more than 96 hours. Fludeoxyglucose F 18 that is not involved in glucose metabolism in any tissue is then excreted in the urine.

Elimination: Fludeoxyglucose F 18 is cleared from most tissues within 24 hours and can be eliminated from the body unchanged in the urine. Within 33 minutes, a mean of 3.9% of the administrated radioactive dose was measured in the urine. The amount of radiation exposure of the urinary bladder at two hours post-administration suggests that 20.6% (mean) of the radioactive dose was present in the bladder.

Special Populations:

The pharmacokinetics of Fludeoxyglucose F 18 Injection have not been studied in renally-impaired, hepatically impaired or pediatric patients. Fludeoxyglucose F 18 is eliminated through the renal system. Avoid excessive radiation exposure to this organ system and adjacent tissues.

The effects of fasting, varying blood sugar levels, conditions of glucose intolerance, and diabetes mellitus on Fludeoxyglucose F 18 distribution in humans have not been ascertained [*see Warnings and Precautions (5.2)*].

13 NONCLINICAL TOXICOLOGY

13.1 Carcinogenesis, Mutagenesis, Impairment of Fertility

Animal studies have not been performed to evaluate the Fludeoxyglucose F 18 Injection carcinogenic potential, mutagenic potential or effects on fertility.

14 CLINICAL STUDIES

14.1 Oncology

The efficacy of Fludeoxyglucose F 18 Injection in positron emission tomography cancer imaging was demonstrated in 16 independent studies. These studies prospectively evaluated the use of Fludeoxyglucose F 18 in patients with suspected or known malignancies, including non-small cell lung cancer, colo-rectal, pancreatic, breast, thyroid, melanoma, Hodgkin's and non-Hodgkin's lymphoma, and various types of metastatic cancers to lung, liver, bone, and axillary nodes. All these studies had at least 50 patients and used pathology as a standard of truth. The Fludeoxyglucose F 18 Injection doses in the studies ranged from 200 MBq to 740 MBq with a median and mean dose of 370 MBq.

In the studies, the diagnostic performance of Fludeoxyglucose F 18 Injection varied with the type of cancer, size of cancer, and other clinical conditions. False negative and false positive scans were observed. Negative Fludeoxyglucose F 18 Injection PET scans do not exclude the diagnosis of cancer. Positive Fludeoxyglucose F 18 Injection PET scans can not replace pathology to establish a diagnosis of cancer. Non-malignant conditions such as fungal infections, inflammatory processes and benign tumors have patterns of increased glucose metabolism that may give rise to false-positive scans. The efficacy of Fludeoxyglucose F 18 Injection PET imaging in cancer screening was not studied.

14.2 Cardiology

The efficacy of Fludeoxyglucose F 18 Injection for cardiac use was demonstrated in ten independent, prospective studies of patients with coronary artery disease and chronic left ventricular systolic dysfunction who were scheduled to undergo coronary revascularization. Before revascularization, patients underwent PET imaging with Fludeoxyglucose F 18 Injection (74 to 370 MBq, 2 to 10 mCi) and perfusion imaging with other diagnostic radiopharmaceuticals. Doses of Fludeoxyglucose F 18 Injection ranged from 74 to 370 MBq (2 to 10 mCi). Segmental, left ventricular, wall-motion assessments of asynergic areas made before revascularization were compared in a blinded manner to assessments made after successful revascularization to identify myocardial segments with functional recovery.

Left ventricular myocardial segments were predicted to have reversible loss of systolic function if they showed Fludeoxyglucose F 18 accumulation and reduced perfusion (i.e., flow-metabolism mismatch). Conversely, myocardial segments were predicted to have irreversible loss of systolic function if they showed reductions in both Fludeoxyglucose F 18 accumulation and perfusion (i.e., matched defects).

Findings of flow-metabolism mismatch in a myocardial segment may suggest that successful revascularization will restore myocardial function in that segment. However, false-positive tests occur regularly, and the decision to have a patient undergo revascularization should not be based on PET findings alone. Similarly, findings of a matched defect in a myocardial segment may suggest that myocardial function will not recover in that segment, even if it is successfully revascularized. However, false-negative tests occur regularly, and the decision to recommend against coronary revascularization, or to recommend a cardiac transplant, should not be based on PET findings alone. The reversibility of segmental dysfunction as predicted with Fludeoxyglucose F 18 PET imaging depends on successful coronary revascularization. Therefore, in patients with a low likelihood of successful revascularization, the diagnostic usefulness of PET imaging with Fludeoxyglucose F 18 Injection is more limited.

14.3 Neurology

In a prospective, open label trial, Fludeoxyglucose F 18 Injection was evaluated in 86 patients with epilepsy. Each patient received a dose of Fludeoxyglucose F 18 Injection in the range of 185 to 370 MBq (5 to 10 mCi). The mean age was 16.4 years (range: 4 months to 58 years; of these, 42 patients were less than 12 years and 16 patients were less than 2 years old). Patients had a known diagnosis of complex partial epilepsy and were under evaluation for surgical treatment of their seizure disorder. Seizure foci had been previously identified on ictal EEGs and sphenoidal EEGs. Fludeoxyglucose F 18 Injection PET imaging confirmed previous diagnostic findings in 16% (14/87) of the patients; in 34% (30/87) of the patients, Fludeoxyglucose F 18 Injection PET images provided new findings. In 32% (27/87), imaging with Fludeoxyglucose F 18 Injection was inconclusive. The impact of these imaging findings on clinical outcomes is not known.

Several other studies comparing imaging with Fludeoxyglucose F 18 Injection results to subsphenoidal EEG, MRI and/or surgical findings supported the concept that the degree of hypometabolism corresponds to areas of confirmed epileptogenic foci. The safety and effectiveness of Fludeoxyglucose F 18 Injection to distinguish idiopathic epileptogenic foci from tumors or other brain lesions that may cause seizures have not been established.

16 HOW SUPPLIED/STORAGE AND DRUG HANDLING

Fludeoxyglucose F 18 Injection is supplied in a multi-dose, capped 30 mL and 50 mL glass vial containing between 0.740 to 7.40 GBq/mL (20 to 200 mCi/mL), of no carrier added 2-deoxy-2-[^{18}F-fluoro-D-glucose, at end of synthesis, in approximately 15 to 50 mL. The contents of each vial are sterile, pyrogen-free and preservative-free.

NDC 40028-511-30; 40028-511-50

Receipt, transfer, handling, possession, or use of this product is subject to the radioactive material regulations and licensing requirements of the U.S. Nuclear Regulatory Commission, Agreement States or Licensing States as appropriate.

Store the Fludeoxyglucose F 18 Injection vial upright in a lead shielded container at 25°C (77°F); excursions permitted to 15-30°C (59-86°F).

Store and dispose of Fludeoxyglucose F 18 Injection in accordance with the regulations and a general license, or its equivalent, of an Agreement State or a Licensing State.

The expiration date and time are provided on the container label. Use Fludeoxyglucose F 18 Injection within 12 hours from the EOS time.

17 PATIENT COUNSELING INFORMATION

Instruct patients in procedures that increase renal clearance of radioactivity. Encourage patients to:

- drink water or other fluids (as tolerated) in the 4 hours before their PET study.
- void as soon as the imaging study is completed and as often as possible thereafter for at least one hour.

Pregnancy: Advise pregnant women of the risk of fetal exposure to radiation with Fludeoxyglucose F 18 Injection [see Use in Specific Populations (8.1)].

Lactation: Advise lactating women that exposure to Fludeoxyglucose F 18 Injection through breast milk can be minimized by pumping and discarding breast milk and avoiding close (breast) contact with the infant for 9 hours after Fludeoxyglucose F 18 Injection [see Use in Specific Populations (8.2)].

Manufactured and distributed by:
PETNET Solutions, Inc.
810 Innovation Drive
Knoxville, TN 37932

PETNET Solutions

Featured Talk

Dementia Imaging Update: Role of the Radiologist in the Era of Disease-Modifying Therapies

Ana M. Franceschi, MD, PhD

Lenox Hill Hospital; Donald and Barbara Zucker School of Medicine
at Hofstra/Northwell, Hempstead, NY, USA

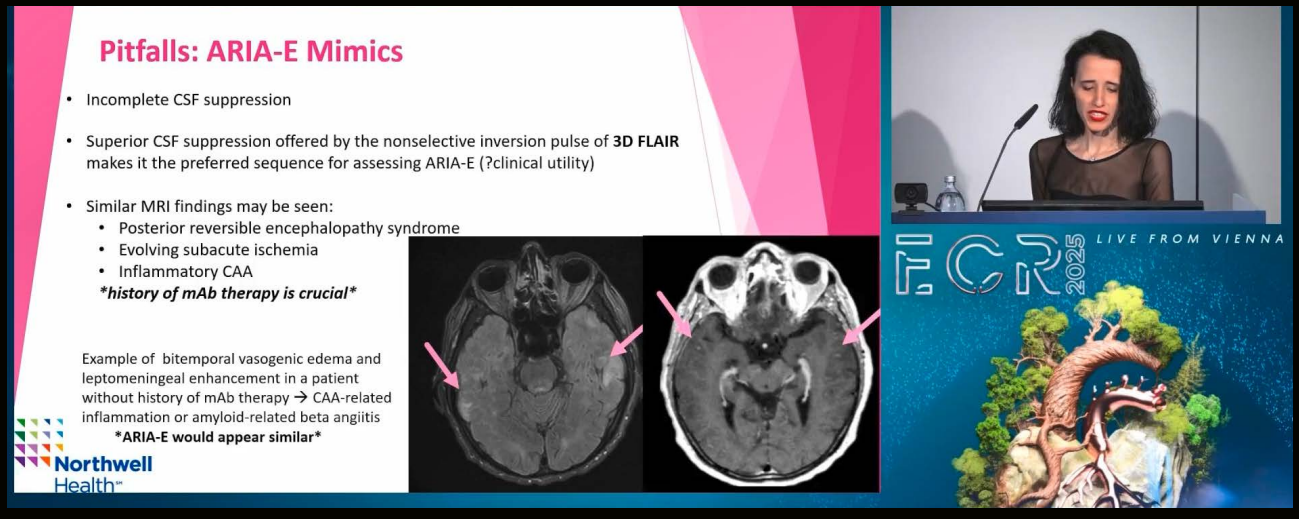

Scan the QR code to view the lecture

on MAGNETOM World > Clinical Corner > Clinical Talks

SIEMENS Healthineers

syngo.MI Neurology Cortical Analysis: Standardization of amyloid PET quantification using the Centiloid scale

Rachid Fahmi, PhD

Siemens Healthineers

Introduction

The value and utility of quantitative measures of beta-amyloid PET imaging have been shown to be relevant in the diagnosis, patient management, and in the design of clinical trials of disease modifying therapies (DMTs) of Alzheimer's disease (AD). However, variability in beta-amyloid PET quantification using standardized uptake value ratio (SUVr) makes it challenging to quantitatively compare amyloid-PET data acquired with different tracers and/or processed using different methods, including differences in cortical target and reference regions chosen to compute SUVrs.

The Centiloid (CL) method was proposed by Klunk et al [1] to standardize measures of beta-amyloid SUVrs for various amyloid PET tracers and analysis methods and providea standardized scale that can be used to improve comparability of amyloid PET quantification and define common normative ranges. The CL scale is anchored at 0 and 100, where the 0-anchor represents young, healthy amyloid-negative controls, and the 100-anchor represents amyloid-positive patients with confirmed AD diagnosis.

The amyloid PET quantification tool, *syngo*.MI Neurology Cortical Analysis, was calibrated to the Centiloid scale for the three commercially available amyloid radiotracers (^{18}F-florbetapir, ^{18}F-florbetaben, and ^{18}F-flutemetamol) to allow direct conversion of composite SUVr values to the CL scale for different tracer-specific cortical target and reference region combinations, as described in the following sections [2].

Centiloid equations

To generate tracer-specific SUVr-to-CL conversion equations, PET images corresponding to young control 0-anchor (YC-0) and AD 100-anchor (AD-100) patients for the selected tracer, and their corresponding paired ^{11}C-PiB images were obtained from the Global Alzheimer's Association Interactive Network (GAAIN) website [3].

For each tracer, GAAIN data consist of a pair of PiB and tracer datasets corresponding to 46 ^{18}F-florbetapir (13 YC and 33 AD), 35 ^{18}F-florbetaben (10 YC and 25 AD), and 74 ^{18}F-flutemetamol scans (24 YC and 50 AD).

Level 2 calibration analysis [1] was performed to generate direct SUVr-to-CL transformations using the three tracer-specific 'cortical target and reference region' combinations in *syngo*.MI Neurology Cortical Analysis, in addition to also using the whole cerebellum reference region to generate CL equations for florbetaben and flutemetamol (Table 2).

For each tracer, the obtained YC-0 and AD-100 images were processed using the *syngo*.MI Neurology Cortical Analysis workflow and the generated SUVr values ($^{Tracer}SUVr$) were regressed against their corresponding published ^{PiB}SUVr values ($^{PiB}SUVr$) [3]. The acceptance criterion for this regression is $R^2 > 0.7$ [1]. The resulting regression equation, with slope $^{Tracer}a$ and intercept $^{Tracer}b$,

$$^{Tracer}SUVr = {}^{Tracer}a \times {}^{PiB}SUVr + {}^{Tracer}b \qquad \text{(Equation 1)}$$

is then used to convert Tracer into calculated PiB SUVrs, Calc-PiB, as follows:

$$^{Calc\text{-}PiB}SUVr = \frac{^{Tracer}SUVr - {}^{Tracer}b}{{}^{Tracer}a} \qquad \text{(Equation 2)}$$

which can then be inserted in the Centiloid Equation 1:

$$^{Tracer}CL = \frac{^{Calc\text{-}PiB}SUVr - {}^{YC-0}_{PiB}SUVr}{{}^{AD-100}_{PiB}SUVr - {}^{YC-0}_{PiB}SUVr} \times 100 \qquad \text{(Equation 3)}$$

	Cerebellar cortex	Whole cerebellum	Pons
AD-100	2.428	2.076	1.535
YC-0	1.170	1.009	0.761

Table 1: Mean SUVr values, $^{AD-100}_{PiB}SUVr$ and $^{YC-0}_{PiB}SUVr$, for different reference regions.

Tracer	Reference regions*	$^{Calc\text{-}PiB}$SUV**	R^2 (a)	SUVr-to-CL equation	R^2 (b)
Florbetapir	WC	(^{Tracer}SUVr – 0.458) / 0.547	0.878	171.49 × ^{Tracer}SUVr – 173.04	0.969
Florbetaben	WC	(^{Tracer}SUVr – 0.448) / 0.517	0.939	181.42 × ^{Tracer}SUVr – 175.84	0.981
	CC	(^{Tracer}SUVr – 0.621) / 0.534	0.908	148.97 × ^{Tracer}SUVr – 185.52	0.960
Flutemetamol	WC	(^{Tracer}SUVr – 0.187) / 0.773	0.946	121.20 × ^{Tracer}SUVr – 117.24	0.968
	Pons	(^{Tracer}SUVr – 0.113) / 0.517	0.960	249.95 × ^{Tracer}SUVr – 126.66	0.959

Table 2: *syngo*.MI Neurology Cortical Analysis Centiloid calibration equations.

* *Tracer-specific cortical regions were used for each tracer.*
** *Calculated PiB value as given by Equation 2.*
a Corresponding to the regression of PiB calculated SUVRs (Equation 2) against published PiB SUVRs [3]. All values are > 0.7.
b Corresponding to the regression of syngo.MI Neurology Centiloid values against published GAAIN counterparts [1,3].
WC: whole cerebellum; CC: cerebellar cortex.

where the reference values $^{AD-100}_{PiB}SUVr$ and $^{YC-0}_{PiB}SUVr$ (Table 1) correspond to the mean PiB SUVr values for the young control 0-anchor (YC-0) (N = 34) and the AD 100-anchor (AD-100) (N = 45) subject sets, respectively. These mean values are determined using the 50-70 min PiB data and the standard cortical region published by GAAIN for different reference regions (Table 1) [1].

For example, if whole cerebellum is used as the reference region for SUVr calculation, then:

$$^{Tracer}CL = \frac{^{Calc\text{-}PiB}SUVr - 1.009}{2.076 - 1.009} \times 100 = \frac{^{alc\text{-}PiB}SUVr - 1.009}{1.067} \times 100$$

This allows the conversion of $^{Tracer}SUVr$ to $^{Tracer}CL$ for each YC-0 and AD-100 subject by substituting $^{Calc\text{-}PiB}SUVr$ given by Equation 2 and the appropriate mean values $^{YC-0}_{PiB}SUVr$ and $^{AD-100}_{PiB}SUVr$ (Table 1) in Equation 3. The final SUVr-to-CL conversion equation is then generated by regressing the SUVr values against the CL values for all YC-0 and AD-100 subjects.

This process was repeated for each tracer and each 'cortical target and reference' region combination to generate the conversion equations shown in Table 2.

The generated calibration equations were used to compare *syngo*.MI Neurology Centiloid values against their published GAAIN counterparts. Corresponding regression and Bland-Altman plots are shown in Figure 1 for each tracer using tracer-specific cortical regions and the whole cerebellum as the reference region for SUVr calculations. These plots show strong correlations and good agreements between the compared sets of CL values across all tracers.

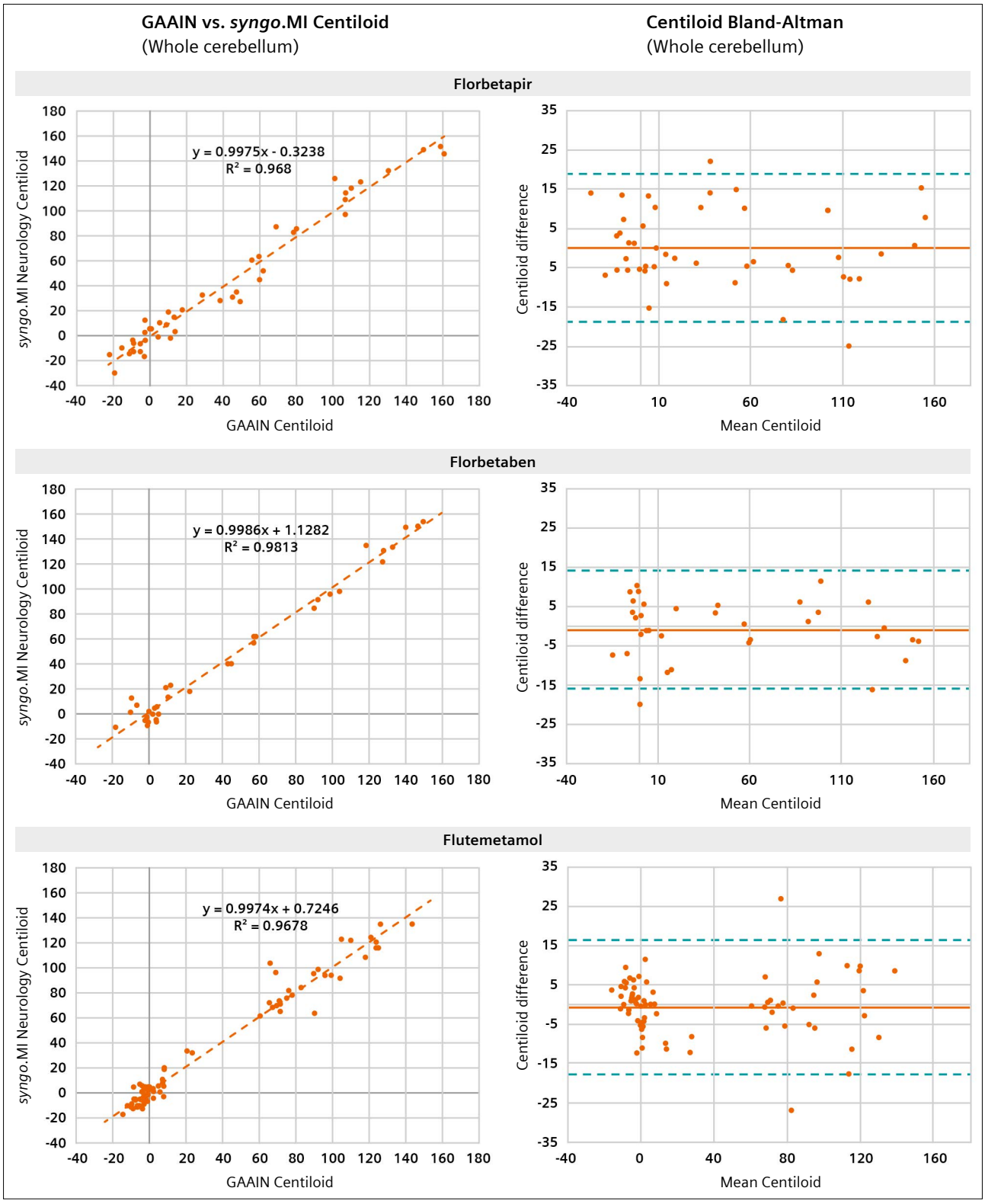

1 Performance evaluation of *syngo*.MI Neurology Centiloid analysis. Comparison of *syngo*.MI Neurology Centiloid values with published GAAIN counterparts for each tracer. Results calculated with *syngo*.MI Neurology correspond to tracer-specific cortical regions and whole cerebellum as reference region. Upper and lower limits (UL and LL) of Bland-Altman plots correspond to "bias ± 1.96 × SD of CL difference": (florbetapir: UL = 15.03 CL and -LL = 18.24 CL with bias = -0.044; florbetaben: UL = 20.34 CL and LL = -12.24 CL with bias = -1.005; and flutemetamol: UL = 16.56 CL and LL = -17.83 CL with bias = -0.60). SD: standard deviation.

Validation with independent datasets

Two experiments were performed to validate the derived Centiloid equations. In the first validation experiment, CL values were calculated with *syngo*.MI Neurology Cortical Analysis using a set of amyloid scans obtained from the Alzheimer's Disease Neuroimaging Initiative (ADNI) database and were compared to publicly available CL values calculated using ADNI processing pipeline with a whole cerebellum reference region [4]. The downloaded ADNI scans correspond to multi-timepoint exams from N = 289 subjects, including elderly healthy controls, patients with mild cognitive impairment (MCI), and AD patients, for a total of 162 ^{18}F-florbetapir and 150 ^{18}F-florbetaben scans. Each scan was processed using *syngo*.MI Neurology Centiloid workflow with the tracer-specific cortical target regions and the whole cerebellum as reference region. Exams were first spatially aligned with an amyloid Montreal Neurological Institute (MNI) template using an affine followed by a deformable registration, and then composite SUVr values were calculated and converted to Centiloid values using the appropriate conversion equation for each tracer (Table 2). The example of a processed florbetaben scan in Figure 2 shows regional and composite SUVrs as well as the corresponding Centiloid value calculated using the tracer-specific cortical regions normalized to the whole cerebellum.

Comparisons between the *syngo*.MI Neurology and corresponding ADNI Centiloid values are shown in Figure 3 with high correlations ($R^2 > 0.97$) and good agreements for both tracers.

The second validation experiment was performed in collaboration with a clinical institution using a multi-site cohort of patients clinically diagnosed with MCI (N = 162; 69 females, 93 males; age: 71.3 ± 6.2 years) [5]. Each patient underwent an amyloid PET exam using one of the three commercially available amyloid PET radiotracers with a total of 22 ^{18}F-florbetaben, 52 ^{18}F-flutemetamol, and 88 ^{18}F-florbetapir scans. Patients were visually classified as amyloid "positive" or "negative" through consensus between two trained nuclear medicine physicians using tracer-specific visual reading guidelines. Centiloid values were calculated using *syngo*.MI Neurology and tracer-specific 'cortical target and reference region combinations' (ie, the cerebellar cortex and the pons were used as reference regions for florbetaben and flutemetamol, respectively). A receiver operating characteristic (ROC) analysis was performed to discriminate patients in agreement with the visual reading used as gold standard.

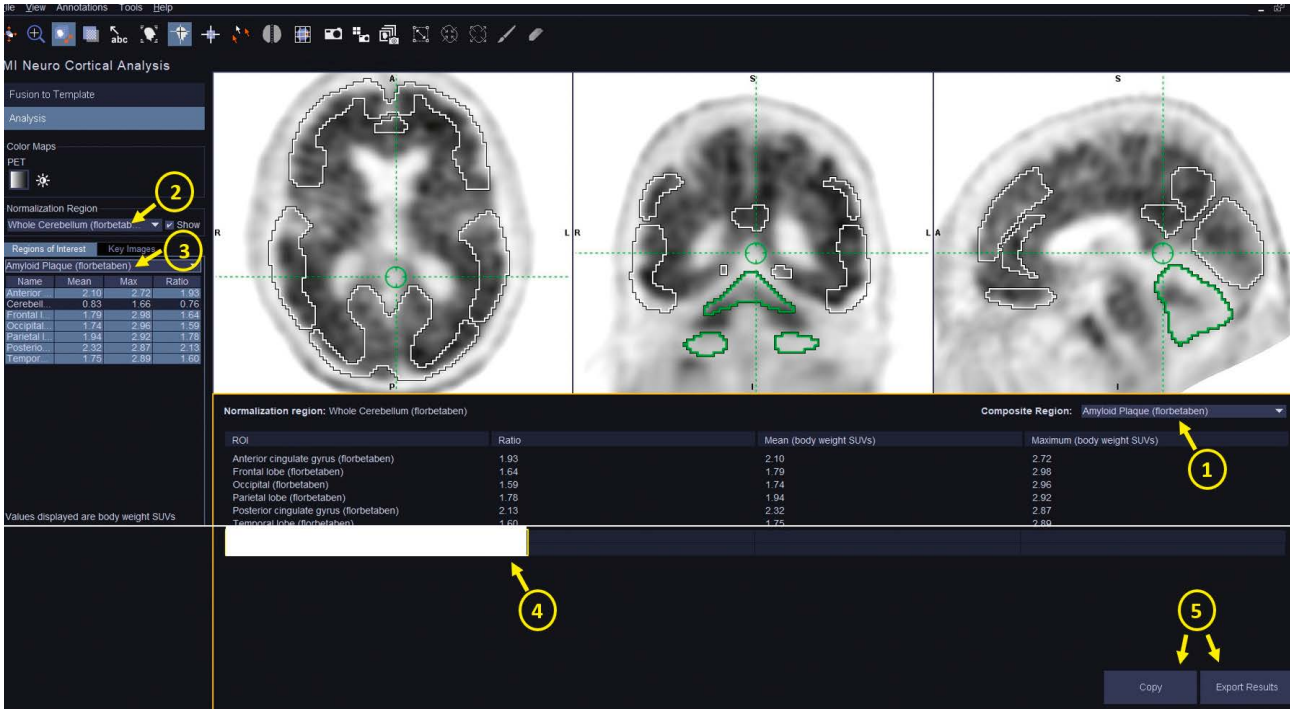

2 Example of a positive ^{18}F-florbetaben scan with a composite SUVr of 1.78 and a corresponding Centiloid value of 147.1 calculated using the tracer-specific cortical regions and the whole cerebellum as reference region. The user can use dropdown menus shown by arrows 1 and 2 to select one of the appropriate combinations of 'cortical target and reference' regions. If a configuration other than the five configurations represented in Table 2 is selected, then only the SUVr value is reported and the Centiloid value is left blank. Dropdown menu 3 can be used to match the composite region selection seen by arrow 1. Each of these regions can be shown overlaid on the PET image when clicked on (white outline: target regions; green: reference region). Calculated composite SUVr and corresponding Centiloid values are shown by arrow 4, which can be copied or exported as a .csv file using buttons shown by arrows 5.

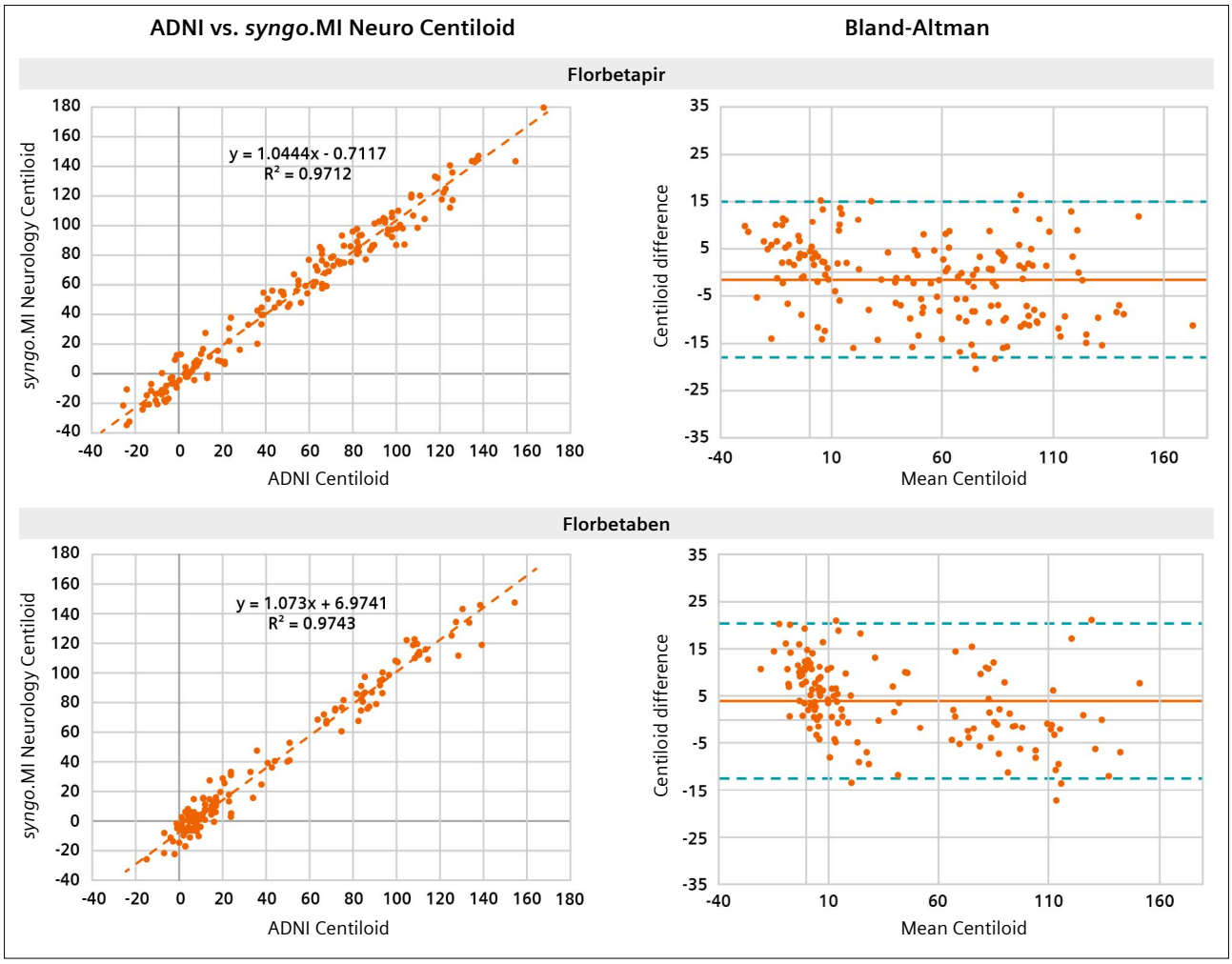

3 Comparison of Centiloid values calculated with *syngo*.MI Neurology Cortical Analysis against their publicly available ADNI counterparts [4]. *syngo*.MI Neurology Centiloid values were calculated using tracer-specific cortical regions with the whole cerebellum as reference region. The upper and lower limits (UL and LL) of Bland-Altman plots correspond to "bias ± 1.96 × SD of CL difference" (florbetapir: UL = 15.03 CL and LL = -18.24 CL with bias = -1.60; florbetaben: UL = 20.34 CL and LL = -12.24 CL with bias = 4.05). SD: standard deviation.

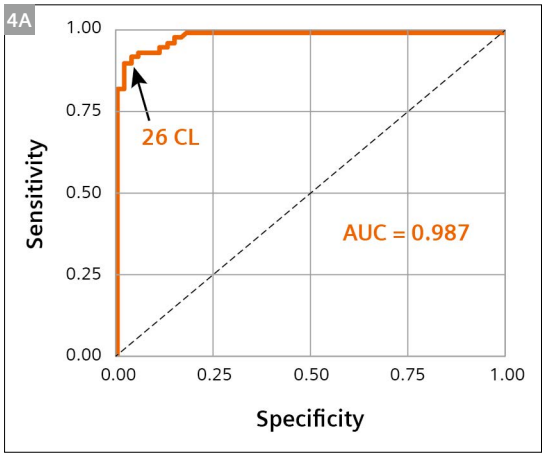

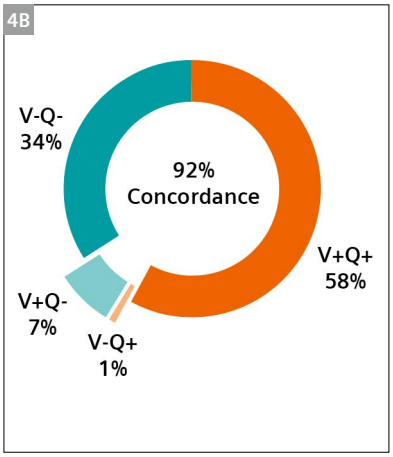

4 **4A:** receiver operating characteristic (ROC) curve showing strong agreement between Centiloid- and visual read-based classifications with an area under the curve of 0.987. **4B:** breakdown of concordant and discordant cases between visually and quantitatively classified subjects as amyloid positive or negative (using a cut-off point of 26 CL). A 92.2% concordance was achieved. V: visual read and Q: quantification.

A Centiloid cut-off value was determined as the value that maximized the Youden's J index of the ROC curve. The percentage of concordance between readers was 95% with eight discordant cases that were excluded from the ROC analysis. Majority of cases (N = 107 or 66%) were visually classified as "positive" (mean ± std: 60.8 ± 28.1 CL), while N = 55 (34%) subjects were visually classified as "negative" with significantly lower CL values (mean ± std: -7.5 ± 20.5 CL; $p < 0.05$). An area under the ROC curve of 0.987 was obtained with a corresponding Centiloid cut-off value of 26 CL (sensitivity 92.0% and specificity 96.3%), indicating high agreement with visual-based classification (Figure 4A). Figure 4B, on the other hand, shows the breakdown of concordant and discordant cases between visual and Centiloid-based classification into positive and negative amyloid scans using 26 CL as cut-off point. Based on the ROC analysis, a Centiloid 'gray zone' ranging between 11 and 39 CL was defined where both specificity and sensitivity are less than 100%. Individuals with a Centiloid value below 11 CL are often referred to as being "clearly negative" or as individuals with early amyloid accumulation, whereas those with a Centiloid value above 39 CL are referred to as "clearly positive" or as individuals with established pathology [6]. Centiloid values corresponding to most discordant cases (83%) (ie, V+Q- or V-Q+, see Figure 4) fall in the gray zone, whereas only 12% of concordant cases (ie, V+Q+ or V-Q-) have their Centiloid values in the gray zone range, indicating that scans with CL values in the gray zone are more challenging to interpret both visually and quantitatively.

The established Centiloid cut-off point, and the gray-zone range are comparable to those published previously [6].

Conclusion

The Centiloid scale provides a standardized framework for amyloid PET quantification and addresses the challenge of comparing SUVr values derived from scans acquired with different tracers and/or processed using different pipelines. Centiloid standardization also allows the derivation of generalizable CL cut-off points that can be used in clinical settings and in research.

The Cortical Analysis workflow within *syngo*.via MI Neurology provides a way to convert SUVr values to the Centiloid scale for all three commercially available PET amyloid tracers using five different combinations of cortical target and reference regions. Validation experiments show that the implemented SUVr-to-CL calibration equations result in reliable Centiloid values and cut-off points that are comparable to those previously published.

References

1 Klunk WE, Koeppe RA, Price JC, Benzinger TL, Devous MD Sr, Jagust WJ, et al. The Centiloid Project: standardizing quantitative amyloid plaque estimation by PET. Alzheimers Dement. 2015;11(1):1-15.e1-4.

2 Fahmi R. Centiloid calibration of a commercial amyloid quantitation software for different Fluorine-18 radiotracers. European Association of Nuclear Medicine (EANM) conference 2023, Vienna, Austria, September 9-13, 2023.

3 The Global Alzheimer's Association Interactive Network (GAAIN) Centiloid project. Available at https://www.gaain.org/centiloid-project.

4 Alzheimer's Disease Neuroimaging Initiative (ADNI). Available at https://adni.loni.usc.edu/.

5 Hirschmüller K, et al. Visual reading and centiloid scaling for the evaluation of brain amyloid PET imaging in patients with mild cognitive impairment: impact on conversion to Alzheimer's disease dementia. European Association of Nuclear Medicine (EANM) conference 2024, Hamburg, Germany, October 19-23, 2024.

6 de Souza GS, Andrade MA, Borelli WV, Schilling LP, Matushita CS, Portuguez MW, et al. Amyloid-β PET Classification on Cognitive Aging Stages Using the Centiloid Scale. Mol Imaging Biol. 2022;24(3):394-403.

Assessing Brain Volumes Using MorphoBox Prototype

Alexis Roche[1,2,3]; Bénédicte Maréchal[1,2,3]; Tobias Kober[1,2,3]; Gunnar Krueger[4]; Patric Hagmann[1]; Philippe Maeder[1]; Reto Meuli[1]

[1] Department of Radiology, University Hospital (CHUV), Lausanne, Switzerland
[2] Advanced Clinical Imaging Technology, Siemens Healthineers, Lausanne, Switzerland
[3] Signal Processing Laboratory (LTS 5), École Polytechnique Fédérale de Lausanne, Lausanne, Switzerland
[4] Siemens Medical Solutions USA, Boston, MA

Introduction

Brain morphometry from routine structural MR images is useful to detect abnormal regional brain volumes that may be indicative of a disease [1]. For instance, hippocampus atrophy is known to be associated with memory impairment commonly experienced by individuals with dementia [2]. When combined with other volumetric measurements such as frontal lobe atrophy and white matter lesions, it may help diagnose a particular form of dementia (Alzheimer's disease, fronto-temporal or vascular dementia among others).

The MorphoBox algorithm[1] was developed by the Advanced Clinical Imaging Technology group in Lausanne in close collaboration with the University Hospital's Radiology Department. As an integral part of a Siemens prototype sequence, it automatically estimates a number of brain volumes from a single T1-weighted MR image acquired with the MPRAGE sequence, and compares these volumes with normative ranges adjusted for head size, age, and sex. The results are presented to the user in the form of a DICOM report, where brain structures that are found to be abnormally small (or abnormally large, e.g. for ventricular structures) are indicated with an asterisk.

Owing to its full incorporation into the MRI system, MorphoBox runs during image reconstruction. Results can be read with the *syngo* standard viewers or sent to the PACS system in order to seamlessly integrate into the radiological workflow. As of early 2016, more than 10,000 patients had benefited from this prototype worldwide.

[1] *Aspects of this research application have been productized under the name AI Rad Companion Brain MR for Morphometry. AI-Rad Companion Brain MR is not commercially available in all countries. Its future availability cannot be guaranteed.*

Methodology

Image processing

MorphoBox implements a processing pipeline consisting of several steps, as outlined in Figure 1. After the incoming MR scan has been checked for protocol compliance with a widely accepted standard for MPRAGE sequences [3], it is submitted to different image quality checks based on both signal-to-noise ratio and contrast-to-noise ratio assessments

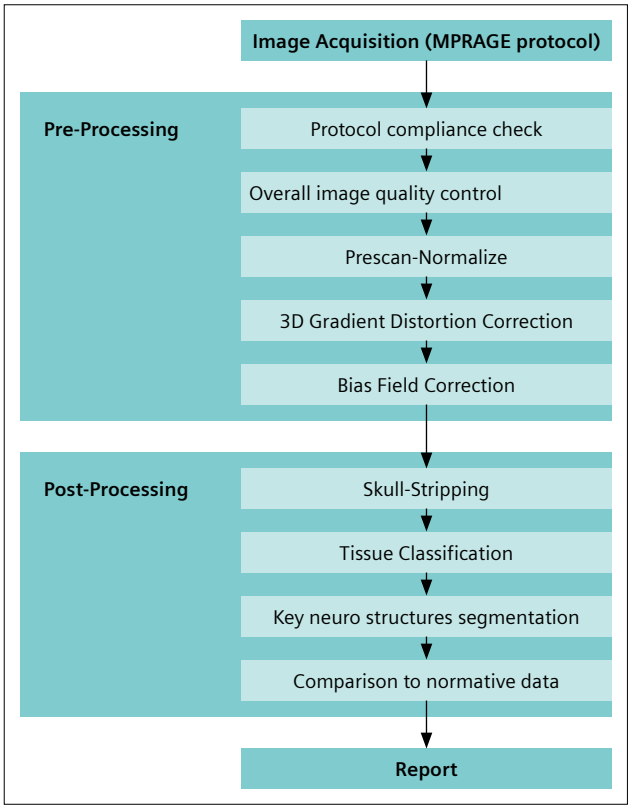

1 Flow diagram of the MorphoBox image processing algorithm.

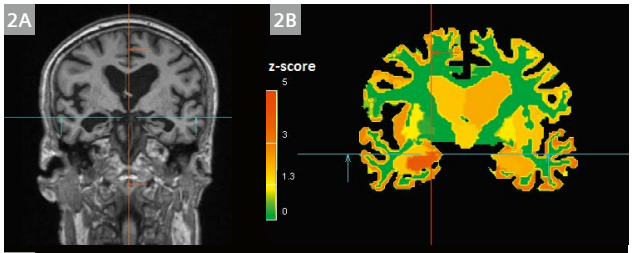

2C

Brain Morphometry Report - 3/7

Patient Demographics	80 yrs	Male	
Image quality	high	0.72	[0 - 0.82]
Segmentation Quality	high	0.82	[0.7 - 1]

Tissue	Absolute [ml]	Normalized^ [%]	Normative Range^^ [%]
TIV	1368.4		
GM	474.8	* 34.7	[37.6 - 43.9]
cortical GM	349.5	* 25.5	[28.3 - 33.6]
WM	426.3	31.2	[26.0 - 31.4]
WMab	0.3	0.0	
CSF	467.3	34.2	[26.7 - 35.3]

^ Percentage of TIV (Total Intracranial Volume)
^^ 10th and 90th percentiles of healthy age-matched population
* Out-of-range volumes

not approved for diagnostic purpose

Brain Morphometry Report - 4/7

Lobar GM/structure	Absolute [ml]	Normalized^ [%]	Normative Range^^ [%]
Frontal lobe			
GM left	67.4	* 4.93	[5.27 - 6.47]
GM right	64.2	* 4.69	[5.20 - 6.35]
Parietal lobe			
GM left	49.2	3.59	[3.48 - 4.46]
GM right	47.7	3.49	[3.41 - 4.31]
Occipital lobe			
GM left	15.4	* 1.12	[1.21 - 1.80]
GM right	15.9	* 1.16	[1.37 - 1.98]
Temporal lobe			
GM left	39.4	* 2.88	[3.32 - 4.00]
GM right	42.4	* 3.09	[3.52 - 4.30]
Cingulate gyrus			
GM left	6.3	0.46	[0.44 - 0.59]
GM right	6.5	0.47	[0.43 - 0.56]
Insula			
Left	3.8	* 0.28	[0.30 - 0.40]
Right	4.1	* 0.30	[0.34 - 0.44]

not approved for diagnostic purpose

Brain Morphometry Report - 3/7

Structure	Absolute [ml]	Normalized^ [%]	Normative Range^^ [%]
Hippocampus	4.3	* 0.31	[0.38 - 0.48]
Hippocampus left	2.3	* 0.17	[0.19 - 0.24]
Hippocampus right	2.0	* 0.14	[0.19 - 0.24]
Ventricles	107.4	* 7.85	[1.94 - 5.38]
lateral ventricle left	55.3	* 4.04	[0.81 - 2.56]
lateral ventricle right	44.1	* 3.22	[0.79 - 2.41]
3rd ventricle	4.6	* 0.34	[0.14 - 0.29]
4th ventricle	3.5	0.25	[0.13 - 0.26]

not approved for diagnostic purpose

2 Screenshots of MorphoBox results on the *syngo* viewer for an Alzeimer's Disease patient. **(2A)** an MRI coronal slice, **(2B)** the corresponding deviation map, and **(2C)** three pages from the report.

as well as motion-/aliasing-related artifact detection [4]. Subsequently, the images are corrected for gradient distortion [5] and radio-frequency field inhomogeneity [6, 7]. A tissue classification algorithm [8] is applied to the corrected image, the results of which are combined with a deformed anatomical template to segment various brain structures in the image [9], including: lobe-wise gray and white matter, insula, cingulate, hippocampi, central nuclei, subcortical white matter, corpus callosum, ventricular system, cerebellum, and different brainstem structures. Volumes are computed for each segmented structure.

Normative range analysis

A cohort of 437 subjects with balanced sex and age ranging from 19 to 91 years was used to construct normative ranges for each brain volume measure output by MorphoBox. Specifically, the volumes produced by MorphoBox on the normative cohort were divided by the corresponding total intra-cranial volume, also estimated by MorphoBox, and regressed against age and sex using a log-linear model [9]. The normative ranges were then defined depending on age and sex by the regression prediction intervals corresponding, respectively, to the 10th and 90th percentiles of the TIV-normalized volume distribution, as seen in Figures 2–7 for various brain structures.

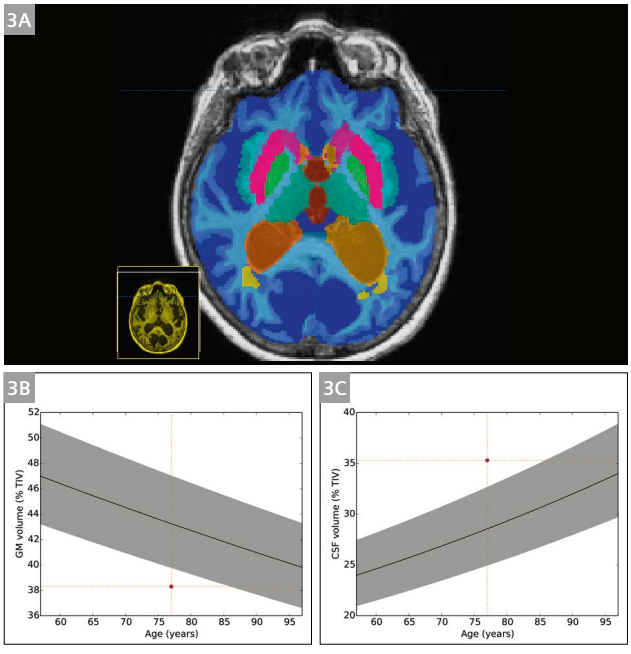

3 **(3A)** Axial slice of a 77-year-old woman with chronic vascular atrophy. Structures of interest segmented by MorphoBox and overlaid in color are the insula, putamen, pallidum, caudate nucleus, thalamus, lateral and third ventricles. In yellow are detected white matter lesions. **(3B–C)** Display of normative ranges for women as a function of age, respectively for the total normalized gray matter volume **(3B)** and the total normalized cerebrospinal fluid volume **(3C)**. The red dots indicate the volumes assessed by MorphoBox.

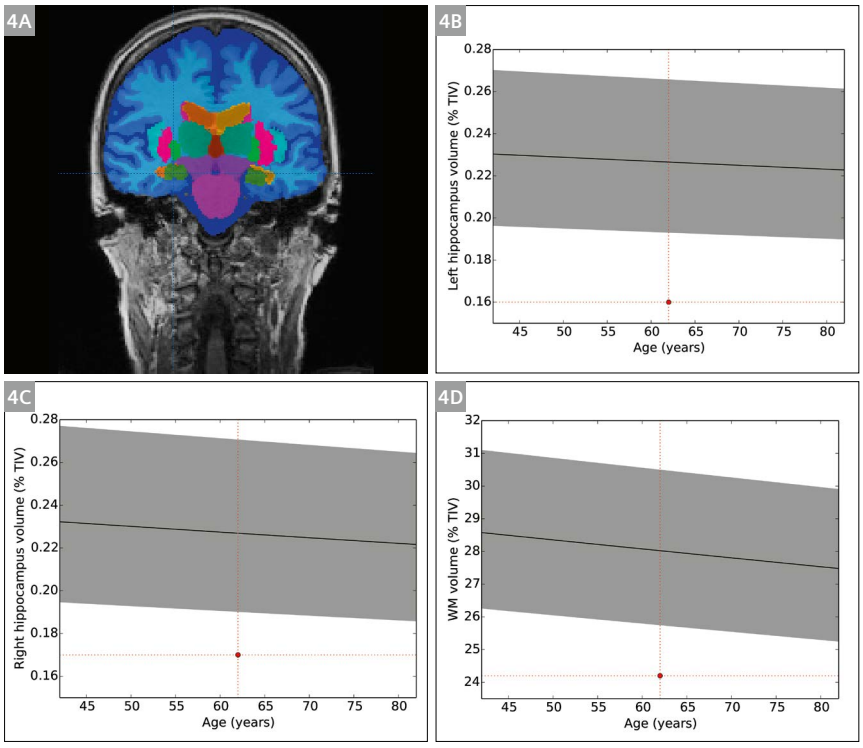

4 **(4A)** Coronal view of a 62-year-old woman with suspected Alzheimer's disease. The segmented hippocampi are shown in green. Other colored structures are the insula, putamen, pallidum, caudate nucleus, thalamus, lateral and third ventricles, mesencephalon, and pons. **(4B–D)** Display of normative ranges of TIV-normalized volumes for women as a function of age, **(4B)** for the left hippocampus, **(4C)** the right hippocampus and **(4D)** the total white matter, respectively.

Creation of report and deviation map

Finally, a report in form of a DICOM image is created containing patient identification, the result of the performed image quality assessment as well as a list of evaluated volumes, divided by hemispheres. Beside the absolute volumes, the TIV-normalized measures are reported and displayed in relation to the normative ranges. Detected deviations from the normative ranges are indicated with an asterisk (see Fig. 2). In addition, MorphoBox produces an image called "deviation map" displaying abnormal regions in hot colors (orange to red depending on the severity of deviation from normality). Since this information is stored as a DICOM image, it can be exported to the PACS like any other image and is available in other viewing software along with the imaging data.

Clinical examples

In the following examples, all brain MR slices are displayed in radiological convention (with the left hemisphere shown on the right of the image).

Results of applying MorphoBox on a 77-year-old female patient with chronic vascular atrophy are depicted in Figure 3A. Both global gray matter atrophy and global cerebrospinal fluid expansion, which are clearly visible in the MR scan, are appropriately detected by MorphoBox, as reflected in the normative range plots in Figure 3B. Other smaller structures are indicated as out-of-range in the MorphoBox report, including the ventricles, the frontal, temporal, parietal lobes, and the insula, in both hemispheres. Figure 4 shows the case of a 62-year-old woman with suspected Alzheimer's disease. Abnormal hippocampi are detected in both hemispheres, suggesting hippocampal atrophy. The total white matter volume is also flagged as abnormally low, which is common in early-age-of-onset Alzheimer's disease [10]. This case is in contrast with that of a 78-year-old woman with suspected early mild cognitive impairment, where the hippocampi like most brain structures are found normal, although insula atrophy is detected mainly on the left, see Figure 5.

As another example, the case of an 88-year-old man with probable cognitive disorder is shown in Figure 6A, for which cortical atrophy can be suspected from visual inspection of the MR scan. Quantitative analysis using MorphoBox (Fig. 6B) reveals that both frontal lobes are small, yet within the bounds of normality, and that both temporal lobes are clearly out-of-range, although the right hippocampus is normal and the left hippocampus is only slightly below the 10th percentile.

MorphoBox can also provide clinically relevant quantitative information on young patients, such as the 20-year-old woman with brain stem disorder shown in Figure 7A. The pons and medulla oblongata are found abnormal by MorphoBox, while the mesencephalon is borderline within normal range, as illustrated in Figure 7B.

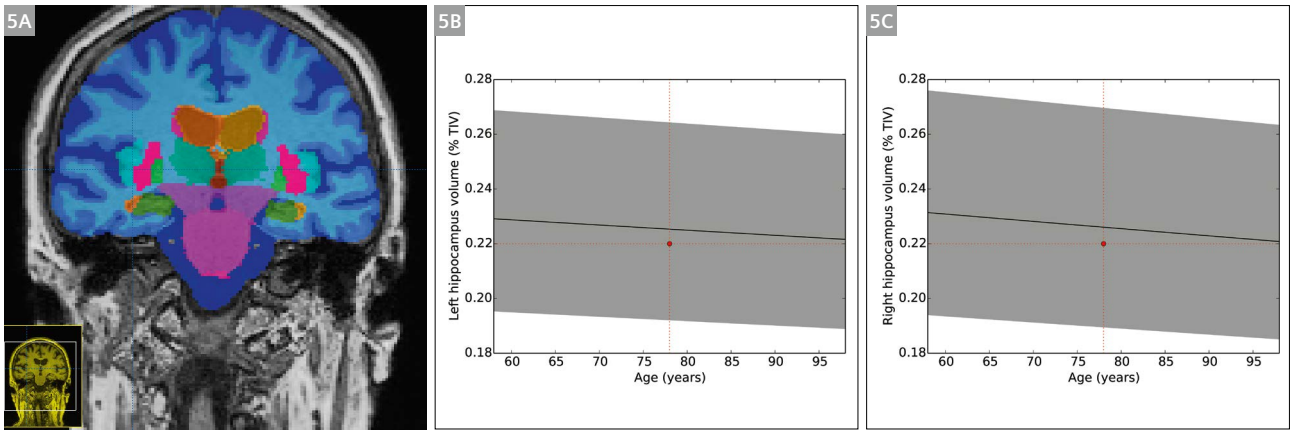

5 **(5A)** Coronal view of a 78-year-old woman with suspected MCI. The hippocampi (highlighted in green) are normal contrary to the left and right insulae (in light blue). Other structures shown in color (the central nuclei, ventricles, and brain stem) are normal. **(5B–E)** Display of normative ranges of TIV-normalized volumes for women as a function of age, **(5B)** for the left hippocampus, **(5C)** the right hippocampus, **(5D)** the left insula, and **(5E)** the right insula, respectively.

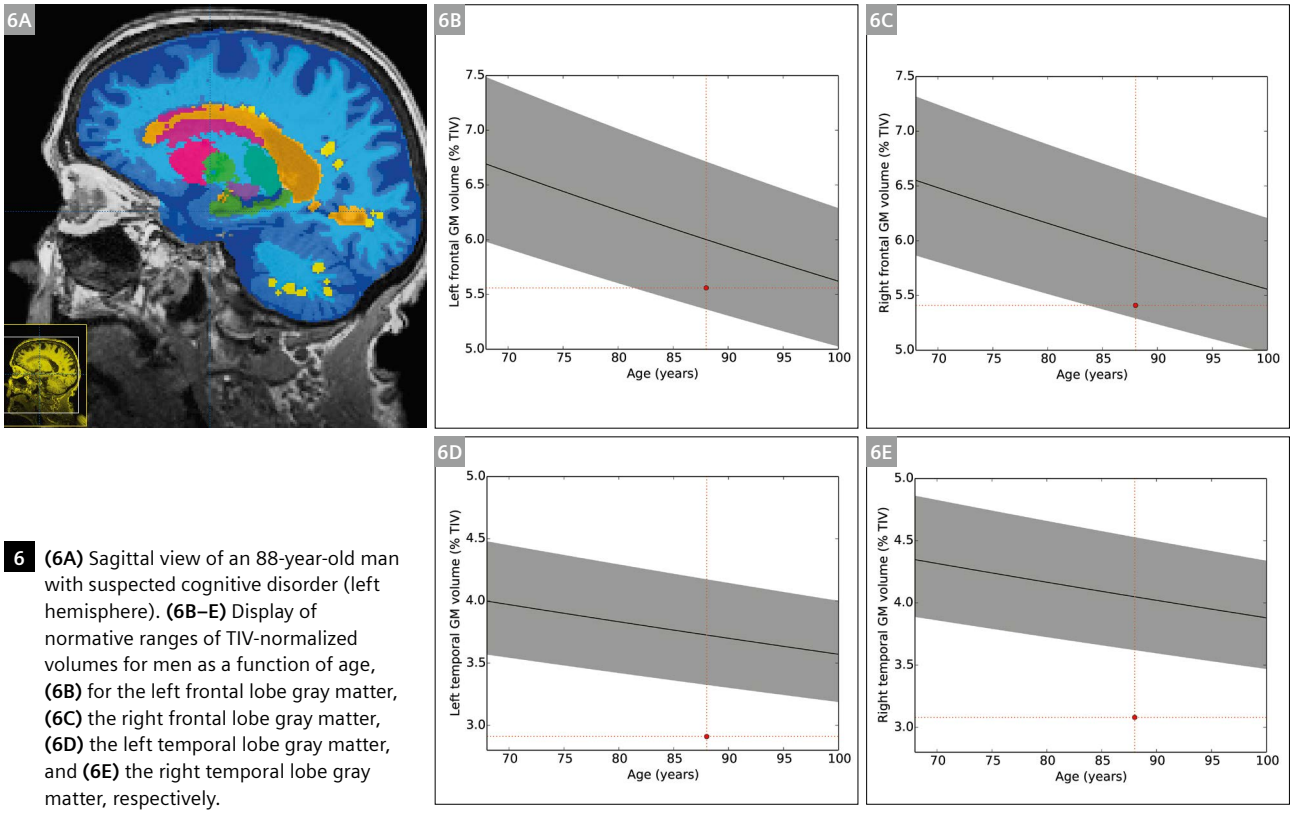

6 **(6A)** Sagittal view of an 88-year-old man with suspected cognitive disorder (left hemisphere). **(6B–E)** Display of normative ranges of TIV-normalized volumes for men as a function of age, **(6B)** for the left frontal lobe gray matter, **(6C)** the right frontal lobe gray matter, **(6D)** the left temporal lobe gray matter, and **(6E)** the right temporal lobe gray matter, respectively.

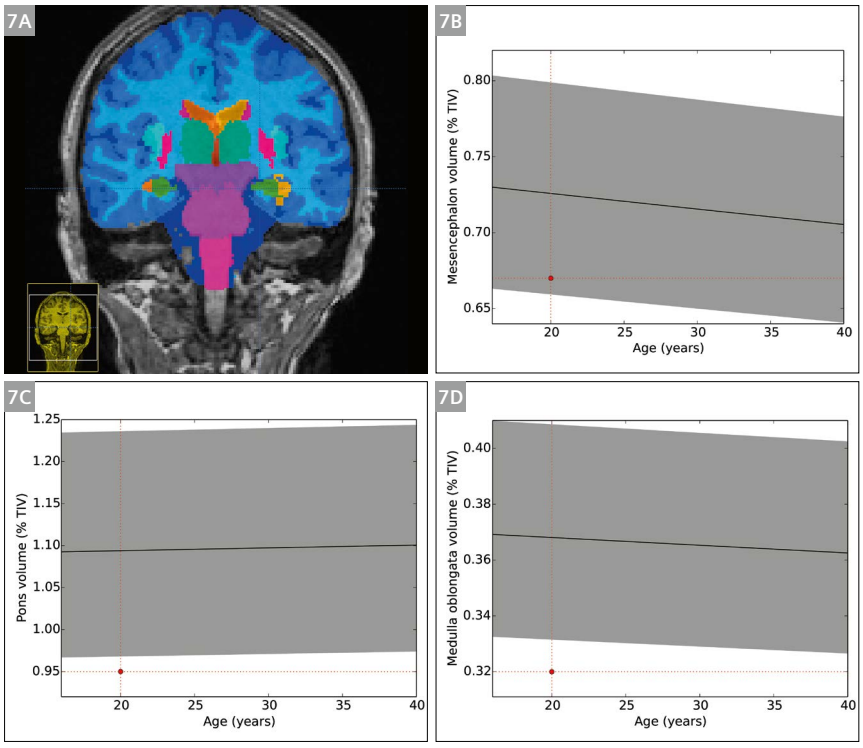

7 **(7A)** Coronal slice of a 20-year-old woman with brain stem disorder. The three brain stem substructures (mesencephalon, pons, medulla oblongata) are shown with distinct colors. **(7B–D)** Display of normative ranges of TIV-normalized volumes for women as a function of age, **(7B)** for the mesencephalon, **(7C)** the pons, and the medulla oblongata, **(7D)** respectively.

Conclusion

MorphoBox is a user-friendly brain volumetry prototype software compatible with clinical workflow constraints and intended for routine use. It provides quantitative information that can help radiological reading for patients with suspected neurodegeneration, as briefly exemplified in this article, and it is fully integrated in a clinical workflow. Our current objective is to further develop MorphoBox as a decision support tool for differential diagnosis of brain diseases.

References

1 D. Mietchen, and C. Gaser. Computational morphometry for detecting changes in brain structure due to development, aging, learning, disease and evolution. Frontiers in neuroinformatics 3: 25, 2009.

2 M.P. Laakso, et al. Hippocampal volumes in Alzheimer's disease, Parkinson's disease with and without dementia, and in vascular dementia: An MRI study. Neurology 46(3):678-681, 1996.

3 C.R. Jack, et al. The Alzheimer's disease neuroimaging initiative (ADNI): MRI methods. Journal of Magnetic Resonance Imaging 27(4):685-691, 2008.

4 B. Mortamet, M. Bernstein, J. C. Jack, J. Gunter, C. Ward, P. Britson, R. Meuli, J.-P. Thiran, and G. Krueger. Automatic Quality Assessment in Structural Brain Magnetic Resonance Imaging. Magnetic Resonance in Medicine 62:365–372, 2009.

5 P. Narayana, W. Brey, M. Kulkarni, and C. Sievenpiper. Compensation for surface coil sensitivity variation in magnetic resonance imaging. Magnetic Resonance Imaging 6:271–274, 1988.

6 K. Van Leemput, F. Maes, D. Vandermeulen, and P. Suetens. Automated model-based bias field correction of MR images of the brain. IEEE Transactions on Medical Imaging 18(10):885–896, 1999.

7 F. Schmitt. Correction of geometric distortion in MR Images. In Proceedings of the computer assisted radiology (CAR), pages 15–25. Springer, 1985.

8 A. Roche, D. Ribes, M. Bach-Cuadra, and G. Krueger. On the Convergence of EM-Like Algorithms for Image Segmentation using Markov Random Fields. Medical Image Analysis 15(6): 830–839, 2011.

9 D. Schmitter, A. Roche, B. Maréchal, D. Ribes, A. Abdulkadir, M. Bach-Cuadra, A. Daducci, C. Granziera, S. Klöppel, P. Maeder, R. Meuli, and G. Krueger. An evaluation of volume-based morphometry for prediction of mild cognitive impairment and Alzheimer's disease. NeuroImage: Clinical 7:7–17, 2014.

10 R. Migliaccio, et al. White matter atrophy in Alzheimer's disease variants. Alzheimer's & Dementia 8(5): S78-S87, 2012.

Contact

Alexis Roche, Ph.D.
Lead Clinical Research
Advanced Clinical Imaging Technology
Siemens Healthcare / CHUV / EPFL
HC CEMEA SUI DI BM PI
1015 Lausanne
Switzerland
Phone: +41 21 545 9972
alexis.roche@gmail.com

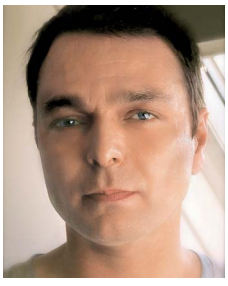

Arterial Spin Labeling as a Potential Biomarker in Imaging of Various Neuro-degenerative Disorders: A PET-MR / PCASL Study in a Tertiary Neuropsychiatric Institute

Sandhya Mangalore; Kavish Kumar Chaurasia; Venkatesh Murthy

Department of Neuroimaging and Interventional Radiology, National Institute of Mental Health and Neurosciences, Bengaluru, India

Introduction

The term "neurodegenerative disorders" refers to a wide range of neurological conditions that develop slowly and steadily over time. These conditions can manifest as problems with cognitive disorders, motor abnormalities, or psychiatric disorders affecting activities of daily living [1]. Clinically, there is a lot of overlap in these domains and hence there is need for imaging biomarkers in the management of neurodegenerative disorders [2].

Varied character, overlapping clinical symptomatology, and the absence of precise clinical, pathological, and molecular diagnoses are major obstacles in the clinical management of neurodegenerative disorders. Confirming a suspected clinical diagnosis is frequently not straightforward and may at times require invasive neuropathological evidence [3]. Non-invasive imaging adjuncts have achieved great advancements in morphological, metabolic, and functional research in recent years.

The current study focuses on the alteration of perfusion patterns studied in 3D Pseudo-Continuous Arterial Spin Labeling (PCASL) MRI in key neurodegenerative disorders, and on the correlation with established molecular imaging techniques ^{18}F-FDG PET and ^{18}F-FDOPA PET. Our optimized protocol at 3T using a research 3D ASL GRASE sequence[1] is shared in the table on the right.

Objectives

1. To correlate the clinical profile, 3D-PCASL and PET-MRI findings in cases of neurodegenerative disorder.
2. To explore the role of 3D-PCASL as a reliable biomarker in the workup of neurodegenerative disorders.

3D ASL protocol parameters	
TR	4600 ms
TE	22 ms
Flip angle	180°
Measurements	16
FOV read	250 mm
FOV phase	100.0%
Slice thickness	4.0 mm
Base resolution	64
Interpolation	On
Phase oversampling	0%
Slice oversampling	0.0%
Slices per slab	36
PAT mode	GRAPPA
Acceleration factor	PE 2
Prescan Normalize	On
AutoAlign	Head > Brain
Bandwidth	2442 Hz/Px
Echo spacing	0.5 ms
EPI factor	31
Turbo factor	12
Segments	3
Perfusion mode	PCASL
Label duration	1500 ms
Postlabel delay	1500 ms
Labeling gap	20.0 mm
PCASL flip angle	28.0°

[1]*Work in progress. The application is currently under development and is not for sale in the U.S. and in other countries. Its future availability cannot be ensured.*

Part 1

	Clinical presentation	PET-MRI and other investigations
Alzheimer's disease (AD) (Fig. 1)	Episodic memory affected early, progressively involved semantic memory, executive function and visuospatial function.	Hypoperfusion on PCASL and hypometabolism on FDG PET involving posterior cingulate gyri, precuneus, and posterior temporal and parietal cortices.
Posterior cortical atrophy variant of AD (Fig. 2)	Visual agnosia, apraxia, prosopagnosia, alexia, environmental disorientation, and Balint syndrome.	Predominant hypoperfusion and hypometabolism of posteromedial parietal and occipital lobes, with or without posterior cingulate hypometabolism.
Behavioral variant of frontotemporal dementia (FTD) (Fig. 3)	Cognitive dysfunction with changes in personality and social behavior. As the disease progresses involvement of language and memory may develop.	Hypoperfusion of dorsolateral prefrontal cortex, anterior cingulate cortex, with or without involvement of lateral and medial temporal lobes; pattern is unilateral and correlates with PET.
Semantic variant of FTD (Fig. 4)	Deficit in expressive and receptive language function, complaints of difficulty in remembering the names of places, people, or objects.	Hypoperfusion and hypometabolism is most marked in the left anterior temporal lobes, temporal pole, and anterior cingulate cortex.
Primary progressive aphasia variant of FTD (Fig. 5)	Agrammatism and effortful, halting speech with inconsistent speech (apraxia of speech).	Left posterior frontal lobe, including Broca's area hypoperfusion and hypometabolism with involvement of anterior cingulate cortex.
Dementia with Lewy bodies (Fig. 6)	Fluctuations in cognition especially in attention, executive function, and visuospatial orientation, visual hallucinations, REM sleep behavior disorder, bradykinesia / rest tremor / rigidity.	Hypoperfusion and hypometabolism in the primary visual cortex, cuneus, and the precuneus, with characteristic sparing of the posterior cingulate gyrus.
Corticobasal degeneration (Figs. 7 and 8)	Asymmetric movement abnormalities, myoclonus, cortical signs including ideomotor apraxia and alien limb phenomenon.	Disproportionate asymmetric cortical hypoperfusion and hypometabolism in the perirolandic posterior frontal (premotor, supplementary motor, primary motor) and superior parietal lobes, and also the basal ganglia.
Vascular dementia	Presenting signs and symptoms are dependent on the areas affected.	Perfusion patterns on PCASL suggesting internal / external watershed zones and normal metabolic uptake in neocortex. Areas of old infarcts in neocortex correspond on FDG PET with PCASL with an abrupt margin.

Table 1: Clinical details and FDG PET-MRI of dementia

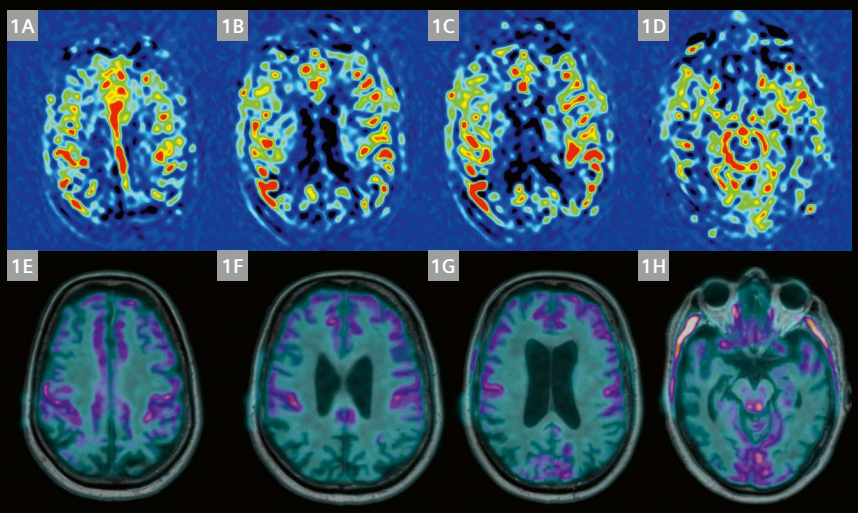

1 Alzheimer's disease (AD)
Patient presented with impaired memory and depression, there was also familial history of dementia in relatives. Upper row **(1A–D)** PCASL images, bottom row **(1E–H)** ^{18}F-FDG PET images demonstrating hypoperfusion on PCASL and hypometabolism on ^{18}F-FDG PET involving the posterior cingulate gyri, precuneus, and posterior temporal and parietal cortices.

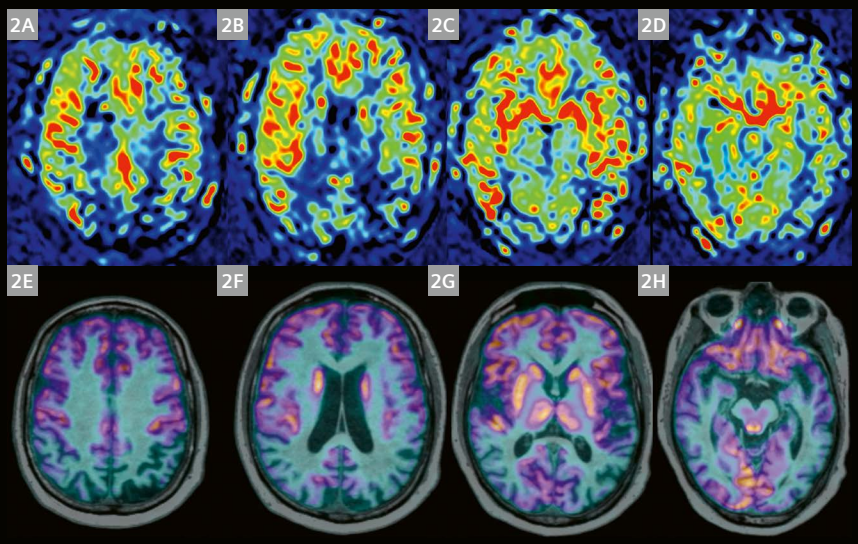

2 Posterior cortical atrophy variant of AD
Patient presented with difficulties in reading, getting dressed, identifying moving objects, identifying distance of objects, and differentiating left from right. Upper row **(2A–D)** PCASL images, bottom row **(2E–H)** ^{18}F-FDG PET images showing predominant hypoperfusion and hypometabolism of posteromedial parietal, and occipital lobes, with or without posterior cingulate hypometabolism.

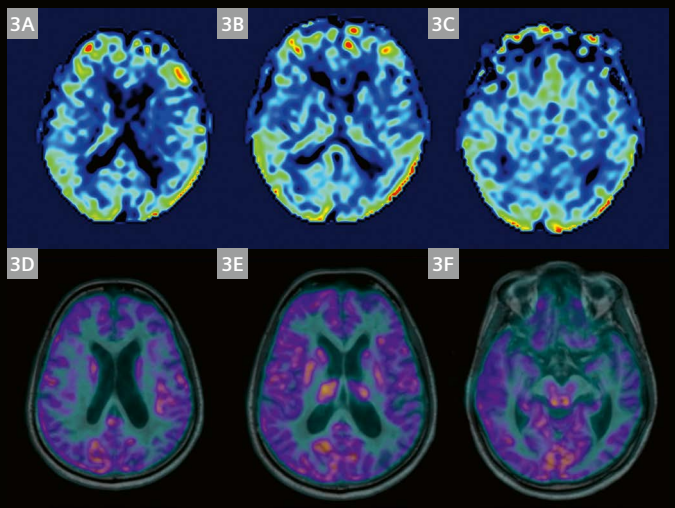

3 Behavioral variant of frontotemporal dementia (FTD)
Patient is chronic alcoholic and presented with impaired immediate and recent memory. Upper row **(3A–C)** PCASL images, bottom row **(3D–F)** ^{18}F-FDG PET images, demonstrating hypoperfusion and hypometabolism, respectively, in the dorsolateral prefrontal cortex, anterior cingulate cortex, and temporal lobes.

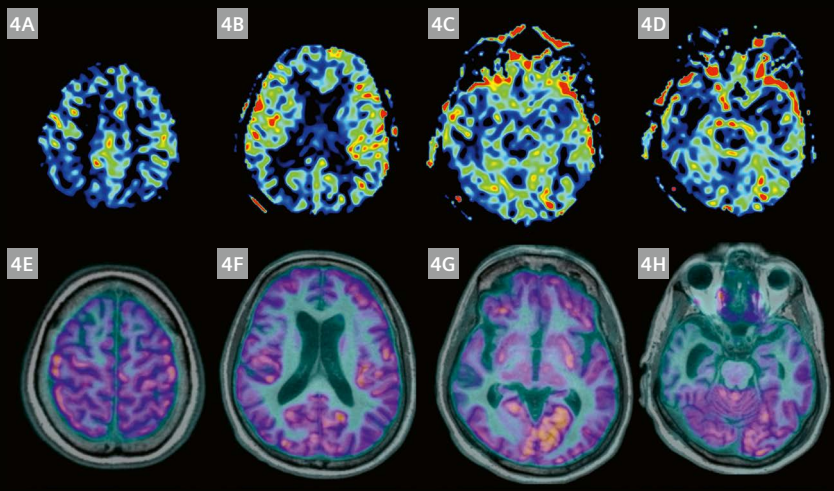

4 Semantic variant of FTD
Patient presented with complaints of decreased pace of movements, memory loss, not recognizing people, behavioral changes, and poor attention. Upper row **(4A–D)** PCASL images, lower row **(4E–H)** ^{18}F-FDG PET images, demonstrating that hypoperfusion and hypometabolism are particularly prominent in the left anterior temporal lobes, temporal pole, and anterior cingulate cortex.

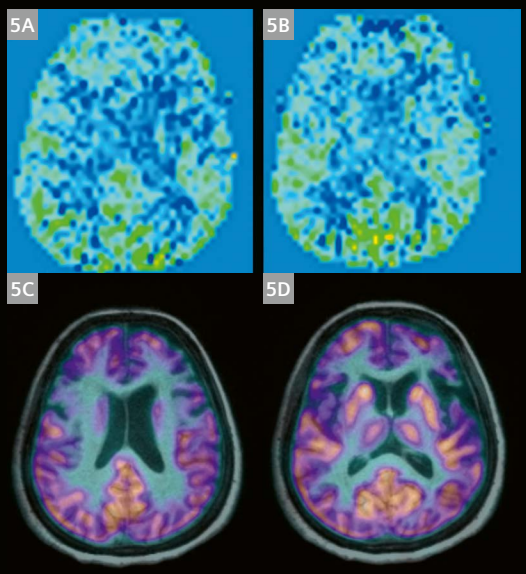

5 Primary progressive aphasia variant of FTD
Patient presented with memory disturbances, agrammatism, and effortful and halting speech for two years. Upper row **(5A, B)** PCASL images, lower row **(5C, D)** ^{18}F-FDG PET images demonstrating hypoperfusion and hypometabolism in the left posterior frontal lobe, including Broca's area, along with involvement of the anterior cingulate cortex.

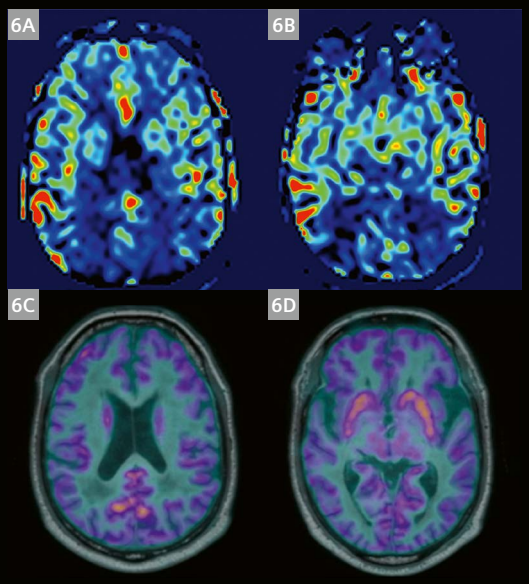

6 Dementia with Lewy bodies
Patient presented with two-year history of decreased pace of walking and cognitive decline, on further evaluation had attentional deficit, apathy, calculation difficulty, and REM sleep behavior disorder. Upper row **(6A, B)** PCASL images, lower row **(6C, D)** ^{18}F-FDG PET images, demonstrating hypoperfusion and hypometabolism in the primary visual cortex, cuneus, and the precuneus, with the characteristic sparing of the posterior cingulate gyrus.

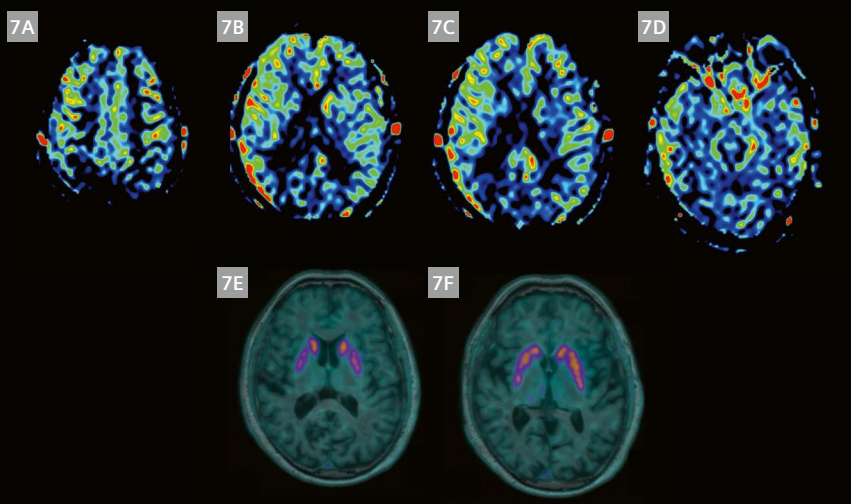

7 Corticobasal degeneration
Patient presented with features of atypical PD (left upper limb tremors, unable to button shirt, and difficulty in walking). Upper row **(7A–D)** PCASL images, lower row **(7E, F)** ^{18}F-FDOPA PET images, demonstrating asymmetric cortical hypoperfusion in the right perirolandic posterior frontal-motor cortex (7A), parietal lobe (7A–C), and temporal lobe (7D), as well as right putamen (7B). Hypometabolism in right putamen (7E, F).

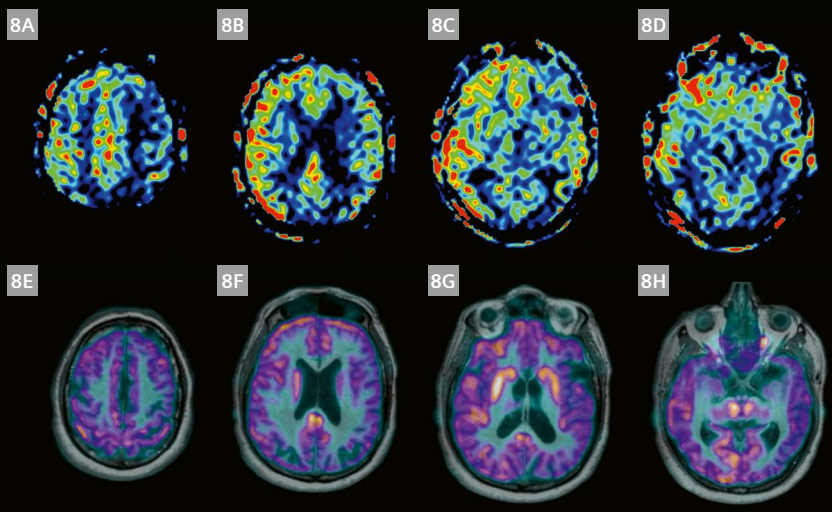

8 Corticobasal degeneration
Patient presented with gradual progressive recognition difficulty, visual spatial difficulty, calculation difficulty, decreased speech, and inability to recognize family members. Clinical examination revealed impaired cortical sensation, graphesthesia and apraxia. Upper row **(8A–D)** PCASL images; bottom row **(8E–H)** ^{18}F-FDG PET images showing disproportionate asymmetric cortical hypoperfusion and hypometabolism in the perirolandic posterior frontal (premotor, supplementary motor, primary motor) and superior parietal lobes, and also the basal ganglia.

Part 2

	Clinical presentation	PET-MRI and other investigations
Progressive supranuclear palsy (Fig. 9)	Early-onset postural and gait instability, dysfunction of vertical eye movements, ataxic or spastic dysarthria, dysphagia, levodopa non-responsive axial rigidity. In a subset of cases, frontal behavioral changes and subcortical dementia.	Hypoperfusion and hypometabolism noted in the bilateral putamen. Additionally, PCASL showed hypoperfusion in the bilateral frontal lobes and anterior cingulate cortex.
Idiopathic Parkinson's disease (Fig. 10)	Bradykinesia, rigidity, and resting tremor.	Hypoperfusion and hypometabolism in the uni-/bilateral posterior part of the putamen. Additionally, hypoperfusion was noted in the bilateral parietal lobe.
Drug-induced Parkinson's disease (Fig. 11)	Atypical tremors noted in background of functional and psychiatric disorders.	Normal perfusion and metabolism noted in the striatal structures. Additionally, normal perfusion noted in the neocortex.
Vascular Parkinson's disease	Diabetic / hypertensive presenting with tremors secondary to infarct / dopaminergic deficit.	Hypometabolism and hypoperfusion noted in the striatal infarcted areas. Additionally, infarcts in the neocortex and watershed zone, infarcts noted in PCASL.
Hypermanganese-induced tremors	Known case of exposure to manganese. MR showing T1 striatal hyperintensity.	Hypometabolism and hypoperfusion in the areas corresponding to T1 hyperintensity in the striatum.
MSA	Dysautonomia associated with either poorly levodopa-responsive parkinsonism (MSA-P), cerebellar ataxia (MSA-C), or both.	Hypometabolism and hypoperfusion in the putamen. Additionally, hypoperfusion noted in the cerebellum.

Table 2: Clinical details and FDOPA PET-MRI in movement disorders

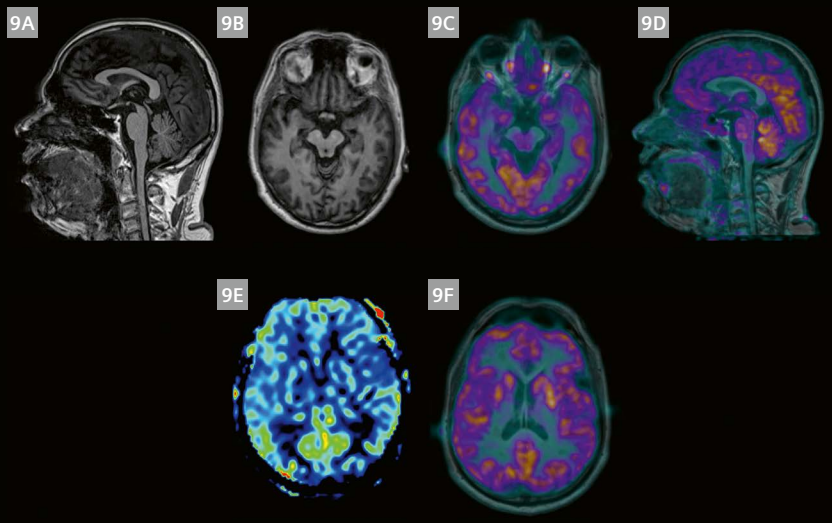

9 Progressive supranuclear palsy
Patient had visual hallucinations and was evaluated for drug-induced parkinsonism. Upper row: T1w sagittal and axial images **(9A, B)** showing significant midbrain atrophy; ^{18}F-FDG PET images **(9C, D, F)** and PCASL **(9E)** image showing hypoperfusion and hypometabolism in the bilateral putamen. Additionally, PCASL showed hypoperfusion in the bilateral frontal lobes, anterior cingulate cortex, and thalami.

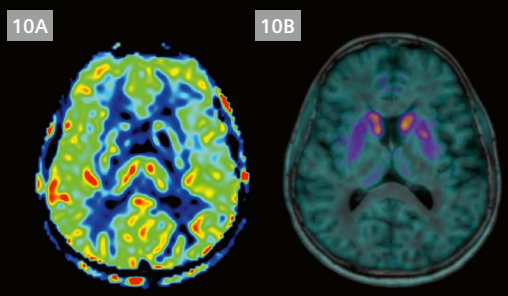

10 Idiopathic Parkinson's disease
Patient presented with stiffness of right arm and right leg, tremors, and numbness. Clinical examination revealed rigidity and micrographia. PCASL image at level of basal ganglia **(10A)** and corresponding ^{18}F-FDOPA image **(10B)** demonstrating hypoperfusion and hypometabolism, respectively, in the bilateral posterior putamen.

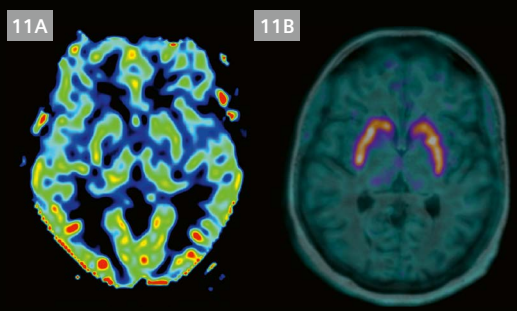

11 Drug-induced Parkinson's disease, post-COVID-19 infection
Patient had fearfulness, anxiety, autonomic hyperactivity, crying spells, symptoms of stress disorder, and had started on antipsychotic medications, after which developed parkinsonian features (rigidity, mask face, monotonous voice, and decreased hand movements). PCASL image at level of basal ganglia **(11A)** and corresponding ^{18}F-FDOPA image **(11B)** show normal perfusion in bilateral basal ganglia, thus demonstrating normal dopaminergic activities and suggesting secondary cause for parkinsonian symptoms.

Part 3

Clinical diagnosis	Clinical presentation
Parkinsonism	FTD-PSP
Parkinsonism	CBS then hemiparkinsonism
FTD	ASL suggestive of CBD-like pattern
	PET-MR findings suggestive of FTD-CBS phenotype
FTD	NPH with nonspecific global hypometabolism and hypoperfusion (Fig. 12)
	AD with CAA
FTD	FTD with vascular dementia
Atypical PD	CBS
FTD	CAA with atherosclerotic vessel disease
Huntington's chorea	FTD ALS / FTD-CBS
Young patient with tremors, anger outbursts, and depression suspected for functional / organic disease.	Structural MRI revealed no demonstrable abnormality. ^{18}F-FDOPA showed bilateral caudate hypometabolism. PCASL demonstrated hypoperfusion in bilateral caudate nuclei and fronto-temporal lobes, with hyperperfusion in occipital lobes similar to ^{18}F-FDG PET findings in Huntington's chorea. Case is under evaluation for Huntington's chorea / PSP / CBD (Fig. 13).

Table 3: Clinical details and FDG PET-MRI in complex neurodegenerative disorders
Abbreviations: AD, Alzheimer's disease; CAA, cerebral amyloid angiopathy; CBD, corticobasal degeneration; CBS, corticobasal syndrome; FTD, frontotemporal dementia; PSP, progressive supranuclear palsy; NPH, normal pressure hydrocephalus; PD, Parkinson's disease; MSA, multiple systemic atrophy.

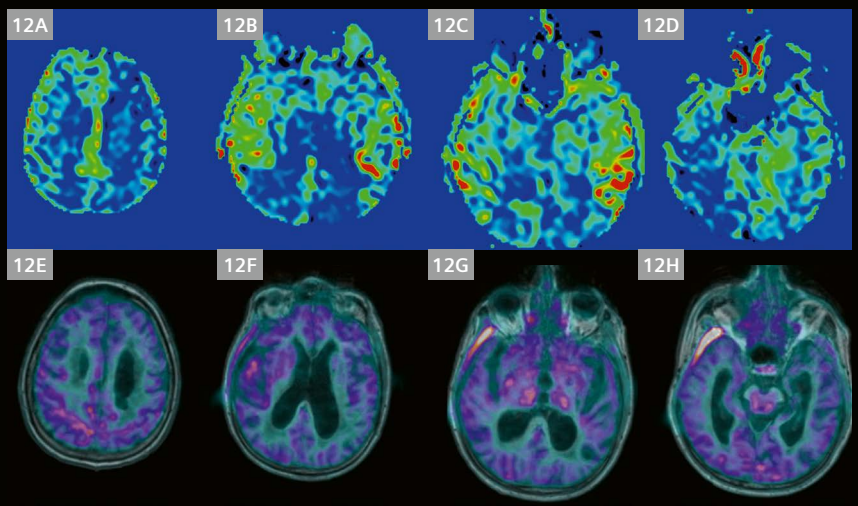

12 Normal pressure hydrocephalus
Patient presented with difficulty in walking, memory loss (recent and in the past), and decreased self-care. Structural MRI showed disproportionate dilation of lateral ventricles to sulcal spaces. Upper row **(12A–D)** PCASL images followed by bottom row **(12E–H)** ^{18}F-FDG PET images showing global hypometabolism in bilateral medial frontal lobes; anterior cingulate gyrus; bilateral parietal, temporal, and occipital lobes; and bilateral thalami.

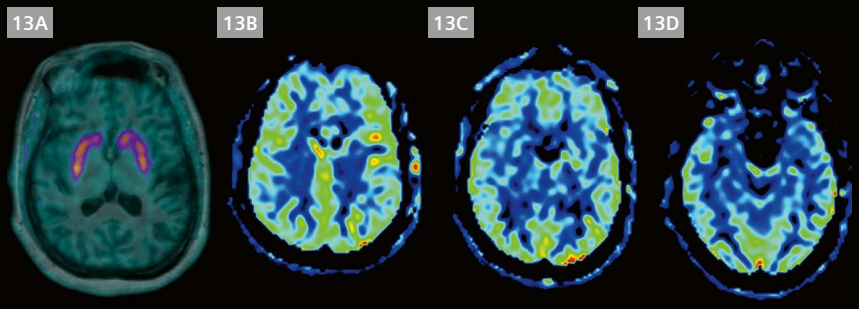

13 Middle-aged patient presented with tremors, anger outbursts, and depression. Evaluated for suspected functional / organic disease. Structural MRI revealed no demonstrable abnormality. ^{18}F-FDOPA showed bilateral caudate hypometabolism. PCASL demonstrated hypoperfusion in bilateral caudate nuclei and frontal-temporal lobes, with hyperperfusion in occipital lobes similar to ^{18}F-FDG PET findings in Huntington's chorea. Case is under evaluation for Huntington's chorea / PSP / CBD.

Materials and methods

This is a prospective observational study that included 108 patients who were referred to our molecular imaging center for imaging between 2020 and today. The study has been divided into three sections. The first section discusses cases of dementia in which FDG PET was correlated with PCASL. The second section discusses cases of movement disorders in which PCASL and FDOPA PET were correlated. The third section discusses how disorders with overlapping clinical symptoms and PET imaging findings can be diagnosed with high sensitivity and specificity using the perfusion pattern of PCASL. Images were acquired using a Biograph mMR PET-MRI scanner and a 3T MAGNETOM Vida (Siemens Healthcare, Erlangen, Germany).

Results

The PCASL perfusion pattern is correlated with clinical symptoms and metabolic patterns as summarized in Tables 1–3.

Learning points

1. PCASL and FDG PET get similar information regarding perfusion and metabolism patterns (Table 1).
2. PCASL correlates with FDOPA for perfusion and metabolism in the striatal structures.
3. When additional FDG-like pattern analysis in movement disorders referred for FDOPA is done, it has been found helpful as discussed in the case-wise pattern in Table 2.
4. Rare cases explored on FDOPA, such as hypermanganesemia, can be better confirmed by FDOPA and PCASL.
5. Vascular dementia is the most common confounder in developing countries. PET is used to diagnose dementia, while PCASL is used for diagnosing the dementia pattern and the vascular perfusion abnormalities, thereby emphasizing the need for simultaneous PET-MRI in overlapping pathologies.
6. In conditions with dual neurodegenerative disorders, such as FTD-ALS and FTD-CBS, PET-MRI helps to confirm the diagnosis, using metabolism and the perfusion pattern (Table 3).

Discussion and conclusion

Neuroimaging findings in neurodegenerative disorders are widespread and difficult, as imaging findings in patients with modest signs and symptoms are frequently subtle and ambiguous. In many cases, by the time imaging findings are obvious, the patient has already manifested clinically, and the diagnosis is already established or at least highly suspected.

The radiation-free PCASL-MRI approach helps, based on the perfusion profile, to achieve an early and accurate diagnosis prior to gross morphological alterations when standardized with PET in simultaneous PET-MRI acquisitions. PCASL and PET changes preceded structural atrophy patterns and could aid in establishing early clinical diagnosis. The combination of PET and PCASL boosted the sensitivity of structural MRI and PET by synergistically diagnosing disease conditions. The synergistic effect of PCASL and FDOPA boosted the sensitivity and specificity in classifying disorders with dopaminergic deficit into IPD/APD phenotypes without the need for additional FDG PET or D2-receptor imaging.

Our study highlights the role of simultaneous PCASL PET-MRI in the workup of complex neurodegenerative conditions with FDG in centers that do not have a cyclotron facility for producing non-FDG tracers. In clear-cut clinical neurodegenerative disorders, where structural changes are equivocal, an additional PCASL sequence can help in early diagnosis without the need for expensive and radioactive PET studies.

Moreover, studies such as ours in a PET-MRI center with a cyclotron facility and referrals of various neuropsychiatric disorders have expanded our understanding of these disorders at a molecular level with functional imaging using PCASL, ^{18}F-FDG, and ^{18}F-FDOPA. Though not displayed in this study, whole-body FDG-PET with DWI MRI has also aided in workups of neurodegenerative disorders by excluding any underlying inflammatory or neoplastic etiology.

References

1 Saba L. Imaging in Neurodegenerative Disorders. Oxford: Oxford University Press; 2015.
2 Nagesh Babu G, Gupta M. Therapeutics in Neurodegenerative Disorders: Emerging Compounds of Interest. In: Ramasami P, Gupta Bhowon M, Jhaumeer Laulloo S, Wah HLK. (eds) Emerging Trends in Chemical Sciences. Cham: Springer International Publishing; 2018, pp. 37–56.
3 Warren JD, Schott JM, Fox NC, Thom M, Revesz T, Holton JL, et al. Brain biopsy in dementia. Brain. 2005;128(Pt 9):2016–2025.
4 Benson DF, Davis RJ, Snyder BD. Posterior cortical atrophy. Arch Neurol. 1988;45(7):789–793.
5 Tripathi M, Tripathi M, Sharma R, Jaimini A, MD'Souza M, Saw S, et al. Functional neuroimaging using F-18 FDG PET/CT in amnestic mild cognitive impairment: A preliminary study. Indian J Nucl Med. 2013;28(3):129–133.
6 Tripathi M, Kumar A, Bal C. Neuroimaging in Parkinsonian disorders. Neurol India. 2018;66(7):68.

Contact

Sandhya Mangalore, M.D., DM
Additional Professor Neuro-Radiology
Molecular Imaging Centre
Division of Neuroradiology
Department of Neuroimaging and Interventional Radiology
National Institute of Mental Health and Neurosciences
Bengaluru 560029
India
Phone: 080 - 26995424/9480829866
sandhya@nimhans.ac.in

Advances in Susceptibility-Weighted Imaging (SWI) and Quantitative Susceptibility Mapping (QSM)

Josef Pfeuffer[1], Korbinian Eckstein[2], Ashley Wilton Stewart[2], Marcel Dominik Nickel[1], Jin Jin[3], Heiko Meyer[1], Steffen Bollmann[2], Kieran O'Brien[3]

[1]Application Development, Siemens Healthineers AG, Erlangen, Germany
[2]The University of Queensland, Brisbane, Australia
[3]Siemens Healthcare Pty Ltd, Brisbane, Australia

Objectives

- Demonstrate enhanced performance of susceptibility-weighted imaging (SWI) in high-susceptibility brain regions (e.g., frontal lobe, ear canals) through improved phase processing.
- Achieve signal-to-noise improvements in SWI via the utilization of multi-echo SWI acquisition and processing techniques.
- Provide a comprehensive overview of processing methodologies and algorithms applied in the generation of quantitative susceptibility mapping (QSM) and susceptibility map-weighted imaging (SMWI).
- Demonstrate the advantages gained from using 3D deep learning *k*-space-to-image reconstruction (Deep Resolve Boost).
- Enable visualization of nigrosome 1 "swallow tail" patterns in the substantia nigra using a 0.65 mm isotropic protocol, accomplished within a three-minute acquisition.

The data shown in this article uses research sequences and scanner inline reconstructions at 3 Tesla[1] with software version *syngo* MR XA60. The 3T MR scanners include MAGNETOM Vida, MAGNETOM Skyra, and MAGNETOM Prisma. Three-dimensional gradient-echo imaging (3D-GRE) and 3D echo-planar imaging (3D-EPI) sequences are used in this article.

Introduction

There has been a growing interest in image contrasts derived from phase images obtained from T2*-weighted gradient-echo (GRE) acquisitions. The fundamental principles of Susceptibility-Weighted Imaging (SWI) were comprehensively expounded by J. R. Reichenbach and E. M. Haacke [1] in 2001. SWI is now a highly valuable contrast for a wide range of clinical applications. Valuable insights into the evolution and application of SWI principles can be found in the related references [2–5]. The recently proposed treatments for Alzheimer's disease will likely increase the utilization of SWI to regularly monitor potential side effects. These "Disease-Modifying Therapies" (DMT) rely on serial MR imaging with T2*-weighted and/or SWI imaging to check for the presence of microhemorrhages and superficial siderosis known as Amyloid-Related Imaging Abnormalities of Hemorrhage (ARIA-H) [6]. The recent Wave-CAIPI SWI product, illustrated in Figure 1, could be a useful addition to this clinical application.

Another phase imaging-based technique known as Quantitative Susceptibility Mapping (QSM) [4, 7–9] can also provide additional information about the apparent magnetic susceptibility of underlying tissues. QSM can provide information about the "biometal" content in tissues, including paramagnetic iron (Fe^{2+}), contrast agents (Gd, Fe^{2+}), and diamagnetic calcium (Ca^{2+}). QSM has the potential to provide new clinical insights into a variety of diseases, allowing for enhanced understanding and diagnosis. Examples include the following:

- Inflammation and Multiple Sclerosis (MS) [4, 10–13]
- Calcification [4] versus hemorrhaging in the brain [14] and in tumors [15]
- Support for presurgical planning for Parkinson's disease [16, 17]
- Iron accumulation in normal aging and in neurodegenerative diseases [18–24]
- Iron overload in the liver [25]
- Bone mineralization [26]

QSM reconstruction involves several sophisticated processing steps which are currently relegated to offline execution instead of using streamlined inline processing on the scanner. Furthermore, even though both SWI and QSM rely on the same underlying data, the lack of compatibility

[1]*Work in progress: The research application is currently under development and is not for sale in the U.S. and in other countries. Its future availability cannot be ensured.*

between the various processing techniques in existing software pipelines has hindered the seamless dual application of SWI and QSM post-processing steps.

In this work, we will showcase results from a research implementation which explored further enhancements to clinical GRE acquisitions attainable through the incorporation of parallel imaging in both directions with CAIPIRINHA acceleration, and adopting multi-echo acquisitions with suitable echo combinations. The SWI reconstruction pipeline on the scanner was extended to enable compatibility with advanced acceleration techniques, including CAIPIRINHA. The pipeline also utilizes an additional Laplacian unwrapping pre-processing step before high-pass filtering, and supports multi-echo datasets.

Magnitude and phase images were previously exported for processing in offline QSM packages. The reconstruction pipeline of the research implementation sequence includes two research QSM methods: TGV and MEDI, as detailed below. These methods run parallel to SWI, providing SWI, QSM maps, and QSM-derived images inline.

Lastly, the benefits of more efficient 3D-EPI sequences are also showcased for both SWI and QSM. This is made possible by integrating a novel deep learning *k*-space-to-image-space reconstruction. Through the utilization of the new 3D Deep Resolve Boost and super-resolution 3D Deep Resolve Sharp features, now available on MAGNETOM scanners, the imaging capabilities for both SWI and QSM applications are further amplified.

Improved Susceptibility-Weighted Imaging (SWI)

The recently available product Wave-CAIPI SWI is an innovative SWI technique exclusive to Siemens Healthineers [27, 28]. Figure 1 compares the speed and image quality of Wave-CAIPI SWI to current standard SWI, obtained using a MAGNETOM Vida with a voxel size of 0.6 × 0.6 × 2.0 mm^3. This novel SWI approach allows for a substantial acceleration in diagnostic single-echo 3D-SWI, enabling imaging in half the acquisition time.

Multi-echo SWI data can be acquired with the research application, and it incorporates 3D Laplacian phase unwrapping for improved phase images. Imaging regions of high susceptibility result in phase shifts greater than ±π, characterized by black and white banding or aliasing in the phase image. This artifact is commonly seen above the paranasal sinuses and the ear canals. Adding a 3D Laplacian unwrapping pre-processing step before the conventional SWI reconstruction effectively removes the aliasing and reveals the smoother underlying phase change.

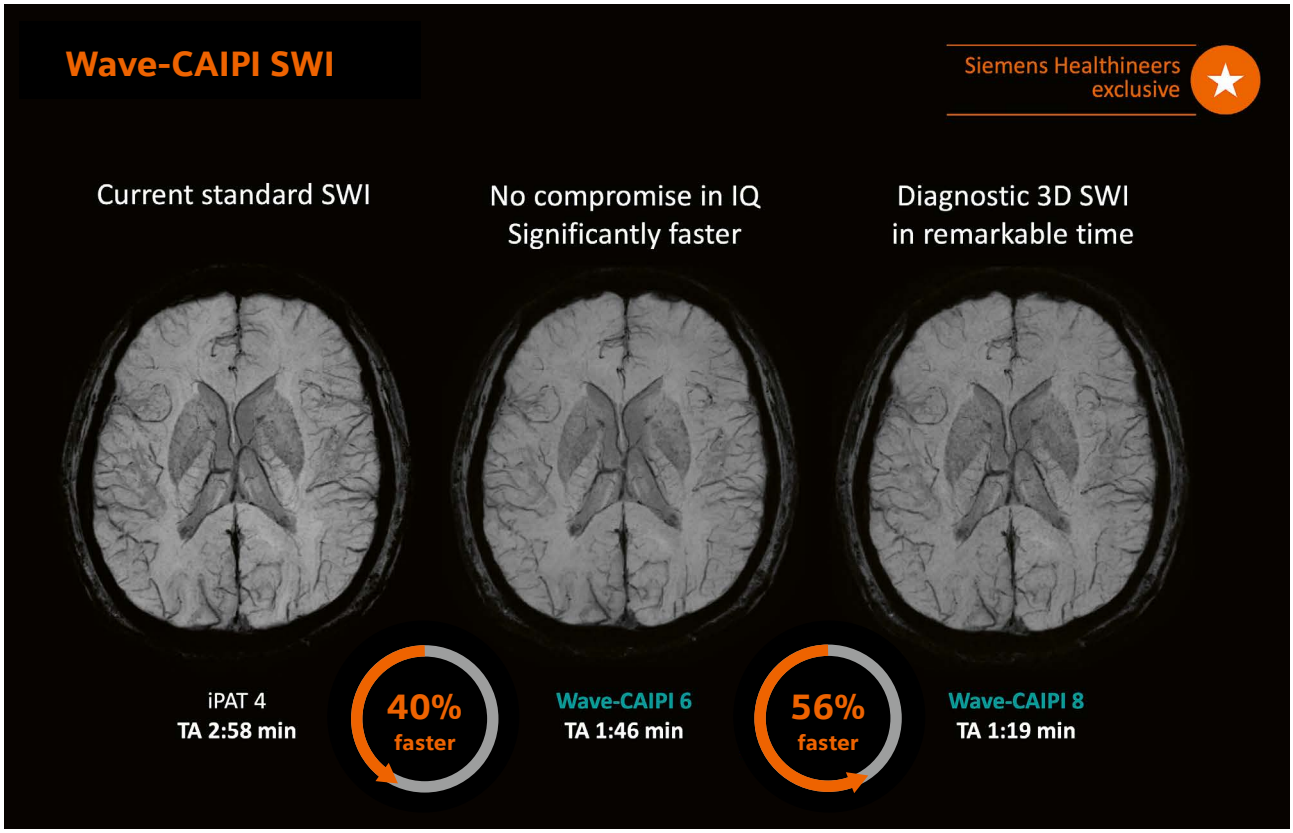

1 Comparison of product SWI and Wave-CAIPI SWI acquired on a 3T MAGNETOM Vida with a voxel size of 0.6 × 0.6 × 2.0 mm^3. This novel SWI technique, unique to Siemens Healthineers, can significantly accelerate diagnostic 3D-SWI and enables imaging twice as fast as standard SWI.

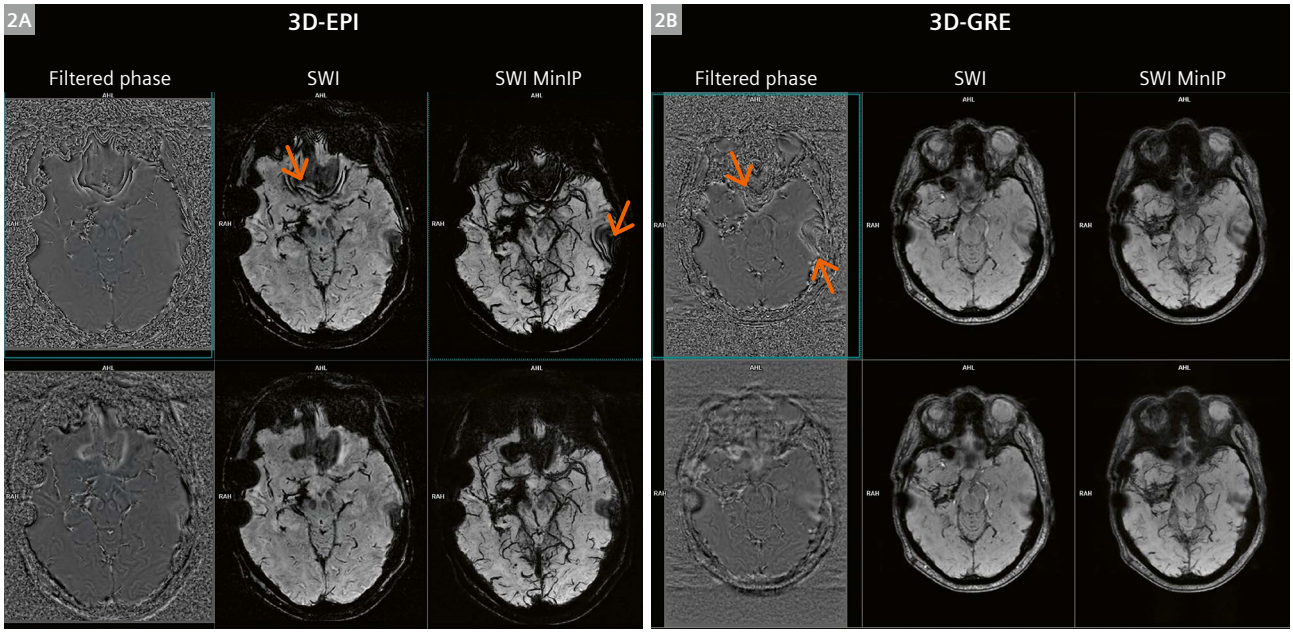

2 Effect of improved phase processing for susceptibility-weighted imaging (SWI): filtered phase (left), SWI image (middle) and minimum intensity projection MinIP (right). Artifacts are visible in regions with large off-resonances above the paranasal sinuses in the frontal lobe and ear canals (top row), causing sudden phase changes or aliasing (phase wraps). They are visibly improved using phase unwrapping (bottom row). The SWI images are from an MS patient scanned with 3D-EPI at an echo time of 40 ms **(2A)** and multi-echo 3D-GRE (ten TEs from 5 to 44 ms) **(2B)**.
Data courtesy of Dr. Sylvie Grand and Professor Alexandre Krainik (CHU Grenoble), and Marylene Delcey (Siemens Healthineers, France).

Imaging parameters:

3D-EPI: FOV 169 x 200 mm^2, 72 slices, resolution 0.39 × 0.39 × 1.5 mm^3 (interpolated), TE 40 ms, TR 80 ms, FA 20°, BW 369 Hz/px, no PAT, EF 11, TA 1:43 min.

3D-GRE: FOV 176 × 256 mm^2, 120 slices, resolution 0.41 × 0.39 × 1.0 mm^3 (interpolated), 10 TEs 5.3–44 ms, $TE_{average}$ 25 ms, TR 50 ms, FA 15°, BW 407 Hz/px, PAT 3, TA 5:25 min.

Consequently, the resultant SWI images show improved signal recovery with minimal artifacts in these areas of high susceptibility.

The impact of enhanced phase processing on SWI is illustrated in Figure 2. This MS patient was scanned using a product 3D-EPI at an echo time of 40 ms (Fig. 2A) and a product multi-echo 3D-GRE (ten echo times ranging from 5 to 44 ms) (Fig. 2B). In the first row, the filtered phase (left), SWI image (middle), and minimum intensity projection (MinIP) (right) depicts phase aliasing artifacts in regions with significant off-resonances (see arrows in the frontal lobe and ear canals). These artifacts result from the sudden phase wraps, which are difficult to resolve with conventional SWI processing. In the bottom row, the same images are presented after employing the Laplacian phase unwrapping pre-processing step. This process visibly improves the artifacts seen in the top row.

To further demonstrate the ability of the multi-echo 3D-GRE acquisition to enhance the signal-to-noise ratio compared to utilizing just a single echo, we present images from another MS patient. (Fig. 3A) SWI images (top panel) and SWI MinIP images (bottom) were captured using a multi-echo 3D-GRE acquisition with ten echoes ranging from 5 to 44 ms. Five out of the ten echo times are displayed, along with the combined images with an average echo time of 25 ms. A comparison is made with a single-echo acquisition on the left (Fig. 3B), highlighting the visibly improved signal- and contrast-to-noise observed in the combined images from the ten echoes. Various weightings for the echo combination can be chosen, such as equal weighting, echo-time-dependent weighting, or user-defined custom weighting.

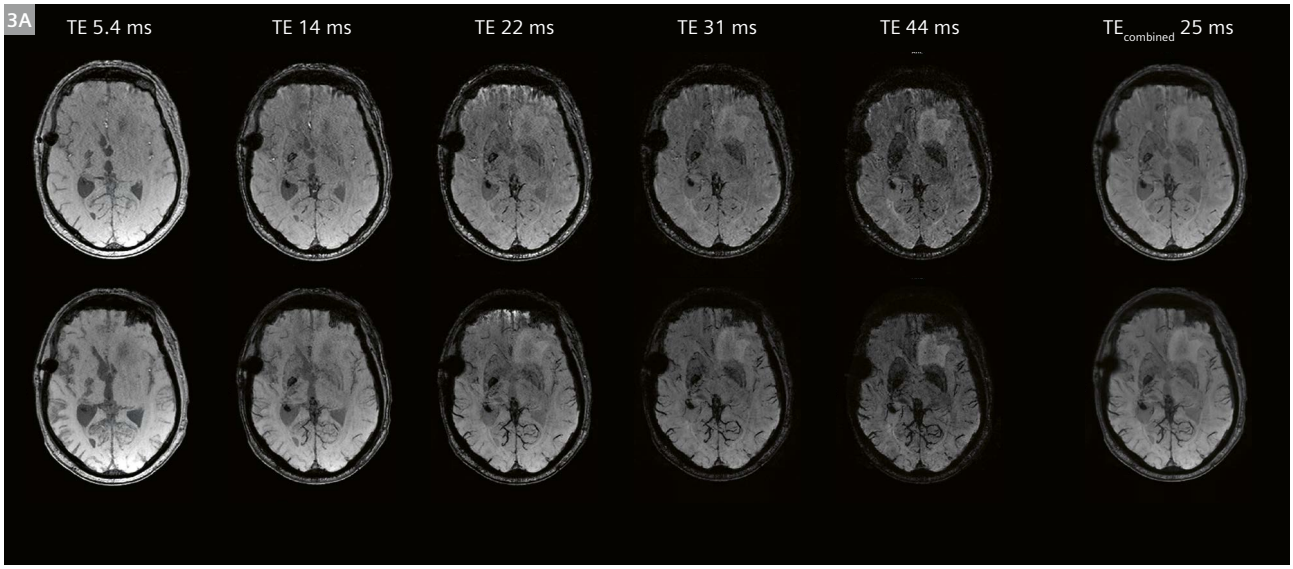

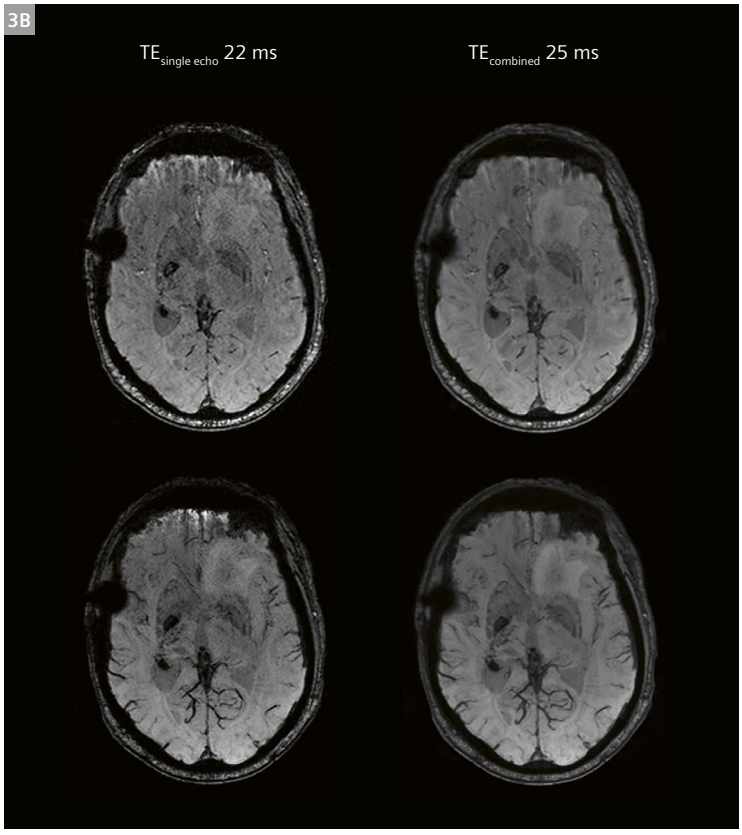

3 Signal-to-noise improvements for SWI using multi-echo 3D-GRE. **(3A)** SWI (top) and SWI MinIP (bottom) from an MS patient with a multi-echo 3D-GRE acquisition using ten echo times from 5 to 44 ms. Five images out of the ten echo times are shown, as well as the combined images with average TE 25 ms. **(3B**) Compared to a single-echo acquisition (left), the combined images from ten echoes show visibly improved signal- and contrast-to-noise.

Imaging parameters: Same 3D-GRE patient data as in Figure (2B) with a different slice shown.

Quantitative Susceptibility Mapping (QSM)

An overview of data acquisition and processing for SWI and QSM is shown in Figure 4. For QSM, the key steps include phase unwrapping, creating a mask from the magnitude image, and applying the background field correction and dipole inversion. In contrast, SWI involves filtering the signal phase, weighting it by the magnitude, and performing a MinIP across slices (Fig. 4A). In the SWI MinIP, the effects of susceptibility from the venous blood make it well-suited to visualizing veins in the brain. However, the processing steps required for SWI imaging make the data incompatible with the steps required to compute QSM. To overcome this, the research implementation reconstructs SWI and QSM in parallel pipelines.

This package now enables the inline post-processing of phase data to generate QSM data using two methods: **Total Generalized Variation (TGV)** [29–31] and **Morphology Enabled Dipole Inversion (MEDI)** [32]. For each method, either a morphological (for brain only) or phase-fidelity-based masking procedure like in ROMEO [31] is required to identify the region of interest for further processing. The package supports three different post processing methods:

- The **MEDI QSM algorithm** applies a choice of background field correction algorithms including the Projection onto Dipole Fields (PDF) and Laplacian Boundary Value (LBV) methods.
- The **TGV QSM algorithm** combines the Laplacian phase unwrapping, background phase removal, and dipole inversion into a single optimization problem. The TGV algorithm is implemented in the Compute Unified Device Architecture (CUDA, NVIDIA, Santa Clara, CA, USA) on the graphics processing unit (GPU) and can be configured by the number of iterations and the regularization parameters. GPU processing time for a 1 mm isotropic whole-brain data set is 5–10 seconds.
- In addition, the **two-step TGV QSM algorithm** [30] is a recent extension of the TGV method which performs two successive TGV reconstructions. The first reconstruction is processed with a mask that only contains reliable susceptibility sources. The second reconstruction applies an additional mask that includes both reliable and less-reliable sources. The different phase-based masks are determined using different thresholds applied to the phase-fidelity image — a normalized phase quality metric. The two-step TGV algorithm aims to be more robust to less-reliable or high-susceptibility sources, which often introduce streaking into the QSM image. The two successive reconstructions are subsequently combined to provide one resultant QSM image.

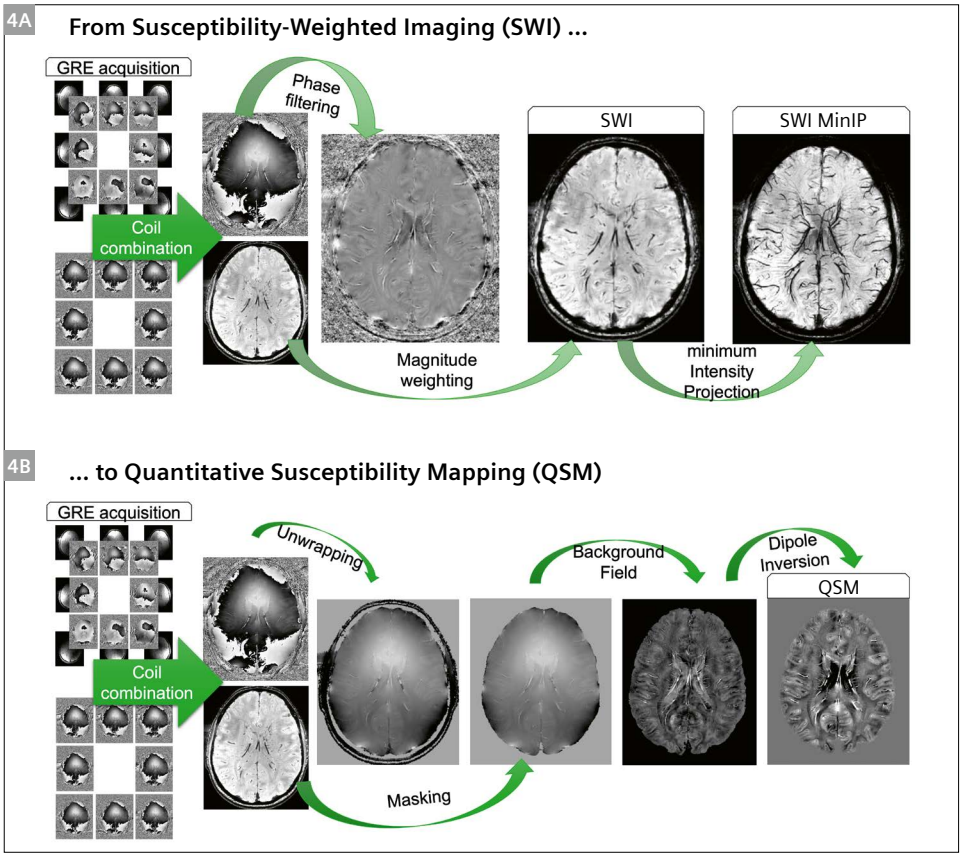

4 Overview of data acquisition and processing for SWI and QSM. **(4A)** SWI is computed from GRE data by filtering the signal phase, weighting it by the magnitude and then minimum intensity projection (MinIP) across slices. In the SWI MinIP, the susceptibility effects from the venous blood make it perfectly suited to visualizing veins in the brain. **(4B)** The steps that are typically required to compute QSM are phase unwrapping, calculating a brain mask, background field removal, and dipole inversion.

In Figure 5, three slices are presented, each processed with different QSM algorithms, along with a derived Susceptibility Map-Weighted Imaging (SMWI) contrast (see below). The QSM maps are scaled to the range of [-100, 300] ppb, which is equivalent to [-0.1, 0.3] ppm. In Figure 5A, the two-step TGV algorithm is featured. The processing mask is created from a phase fidelity map and is thereby independent from brain anatomy. In Figure 5B, the MEDI algorithm is employed, utilizing brain masking with slight erosion of image edges to mitigate artifacts in the dipole inversion process. The overall representation of deep brain structures is well-preserved in both QSM modalities, with MEDI showing a tendency for increased QSM values compared to TGV, while TGV images appear less regularized (smoothed) in comparison to MEDI.

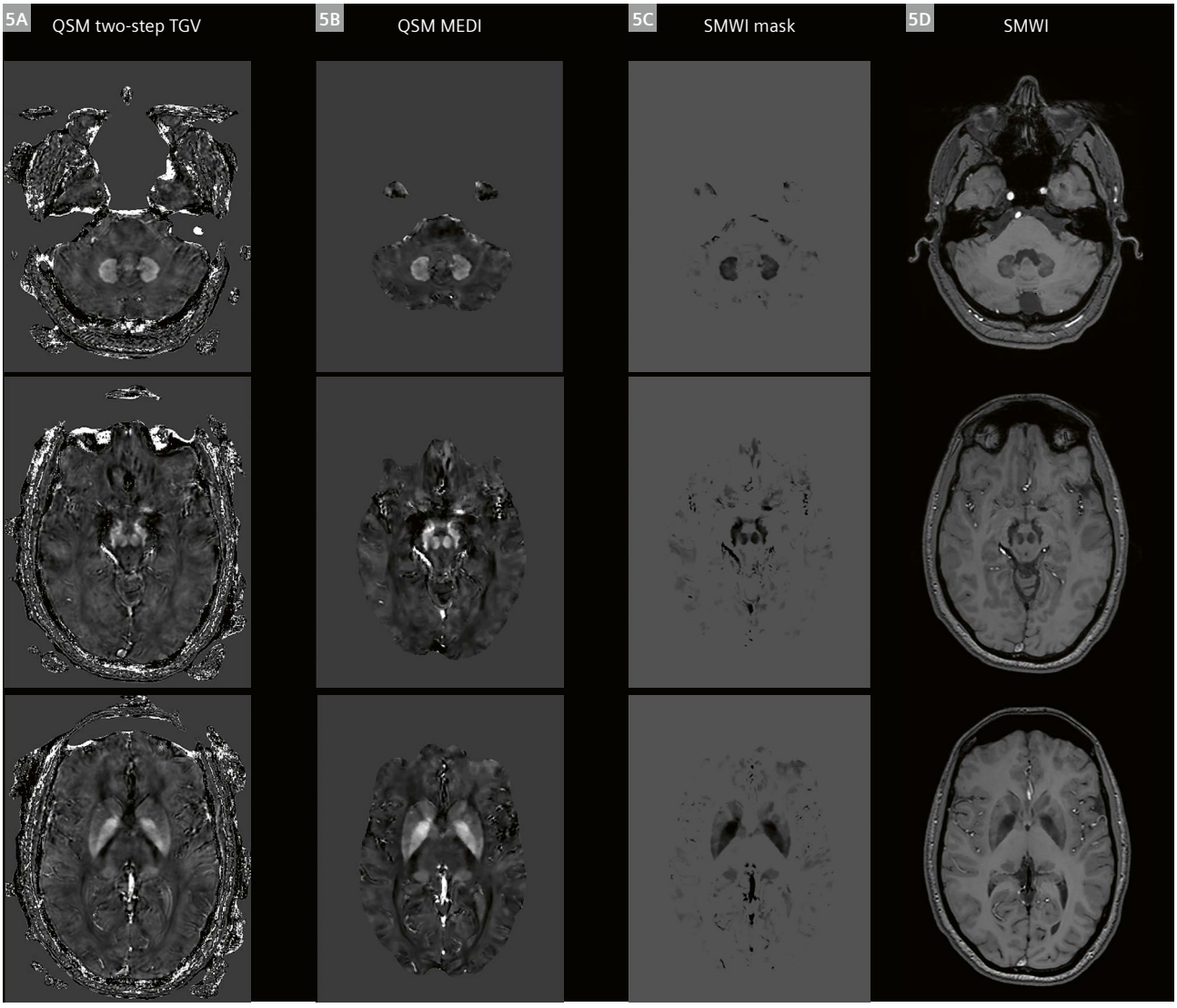

5 Three slices processed with different QSM algorithms and the derived SMWI contrast. The QSM maps are scaled to [-100, 300] ppb, equivalent to [-0.1, 0.3] ppm. **(5A)** The two-step TGV algorithm creates the processing mask from a phase fidelity map and is thus independent from brain anatomy. **(5B)** The MEDI algorithm uses brain masking, and the image edges are somewhat eroded to avoid artifacts in the dipole inversion process. Overall, deep brain structures are represented well in both QSM modalities. MEDI has a tendency for increased QSM values compared to TGV, while the TGV images appear less regularized (smoothed) compared to MEDI. **(5C)** SMWI mask with a weighting factor between [0, 1] calculated from Figure 5B, QSM MEDI images. **(5D)** SMWI images derived from the SMWI mask and the underlying magnitude image.

Imaging parameters:

3D-GRE: FOV 178 × 256 mm^2, 128 slices, resolution 0.5 × 0.5 × 1.0 mm^3 (interpolated), 6 s TE 5.4–27 ms, $TE_{average}$ 16 ms, TR 31 ms, FA 20°, BW 407 Hz/px, PAT 2, Deep Resolve Boost and Sharp, TA 4:25 min.

Susceptibility Map-Weighted Imaging (SMWI)

SMWI has recently been proposed to enhance the contrast-to-noise ratio for visualizing structures containing iron. Recent studies, such as the one conducted by Sung and colleagues in 2022, have demonstrated that SMWI surpasses SWI in assessing nigral hyperintensity at 3T [33].

SMWI images are generated from the QSM image, following the method outlined by Sung-Min Gho et al. in 2014 [34]. This involves combining the magnitude image with a QSM-based weighting factor, introducing an alternative yet analogous contrast to SWI.

The paramagnetic susceptibility mask (with positive susceptibility values, $th_{value} > 0$) is designed as follows [34]:

$$S_{mask}(x) = \begin{cases} 0 & th_{value} < S_{value}(x) \\ (th_{value} - S_{value}(x)) / th_{value} & 0 < S_{value}(x) \leq th_{value} \\ 1 & otherwise \end{cases}$$

By default, SMWI employs a paramagnetic susceptibility mask (pSMWI) with a preset threshold of 1 ppm (1000 ppb) and a multiplication factor denoted as m = 4. In the context of different pathologies, the utilization of a diamagnetic susceptibility mask (dSMWI) with negative susceptibility values is considered advantageous, although it is not explicitly illustrated in the present context.

The pSMWI mask is shown in Figure 5C and is characterized by a weighting factor within the range [0, 1], and is computed from the QSM MEDI images illustrated in Figure 5B. The SMWI images in Figure 5D are subsequently generated by combining the SMWI mask with the underlying magnitude image.

3D deep learning *k*-space-to-image reconstruction

The standard image reconstruction of the 3D-GRE and 3D-EPI sequences include GRAPPA and CAIPIRINHA. The research 3D-EPI application herein allows for flexible EPI train lengths, segmentation, and acceleration factors [35, 36]. Both sequences also include the 3D deep learning *k*-space-to-image reconstruction method Deep Resolve Boost, and the super-resolution method Deep Resolve Sharp.

The deep learning reconstruction comprises two independent, sequential processing steps. Firstly, Deep Resolve Boost images are generated on the acquired resolution using a variational network architecture with six iterations that alternate between parallel imaging reconstruction and 3D image regularizations using U-nets. The network parameters were determined through supervised training based on several hundreds of fully sampled 3D datasets of healthy volunteers from various body regions. Secondly, for Deep Resolve Sharp, the obtained images were interpolated using a deep learning-based super-resolution algorithm, with a factor-of-two interpolation. Both steps were implemented in PyTorch trained on a dedicated GPU cluster and with networks exported for prospective use in the scanner reconstruction pipeline.

Figure 6 displays QSM maps scaled within the [-100, 300] ppb range, obtained from the two sequences 3D-GRE and 3D-EPI, employing different image reconstructions. The QSM algorithm applied in this context was TGV.

The 3D-EPI protocol parameters were matched to those of the five-echo 3D-GRE, with an echo time set to 20 ms. The five-echo 3D-GRE had echo times ranging from 6.6 to 34 ms, with an average echo time of 20 ms. The acquisition time (TA) for the 3D-GRE sequence was 5:35 min. To align with the five echoes of the 3D-GRE, the EPI factor for 3D-EPI was set to five, rendering this sequence approximately four times faster (TA 1:41 min). The minimum repetition time (TR) was selected, specifically TR 39 ms for 3D-GRE, and TR 56 ms for 3D-EPI, respectively.

The signal- and contrast-to-noise ratio in the QSM maps exhibits a slight decrease when comparing 3D-GRE to the faster 3D-EPI acquisitions, as depicted in Figure 6A from left to right. This reduction aligns with our anticipated outcome from signal-to-noise calculations. However, when the data is reconstructed using the 3D deep learning *k*-space-to-image reconstruction method (Deep Resolve Boost), the QSM image quality and structural features are comparable to standard reconstruction. This holds true even with the approximate four-fold increase in speed, as illustrated in Figure 6B from left to right.

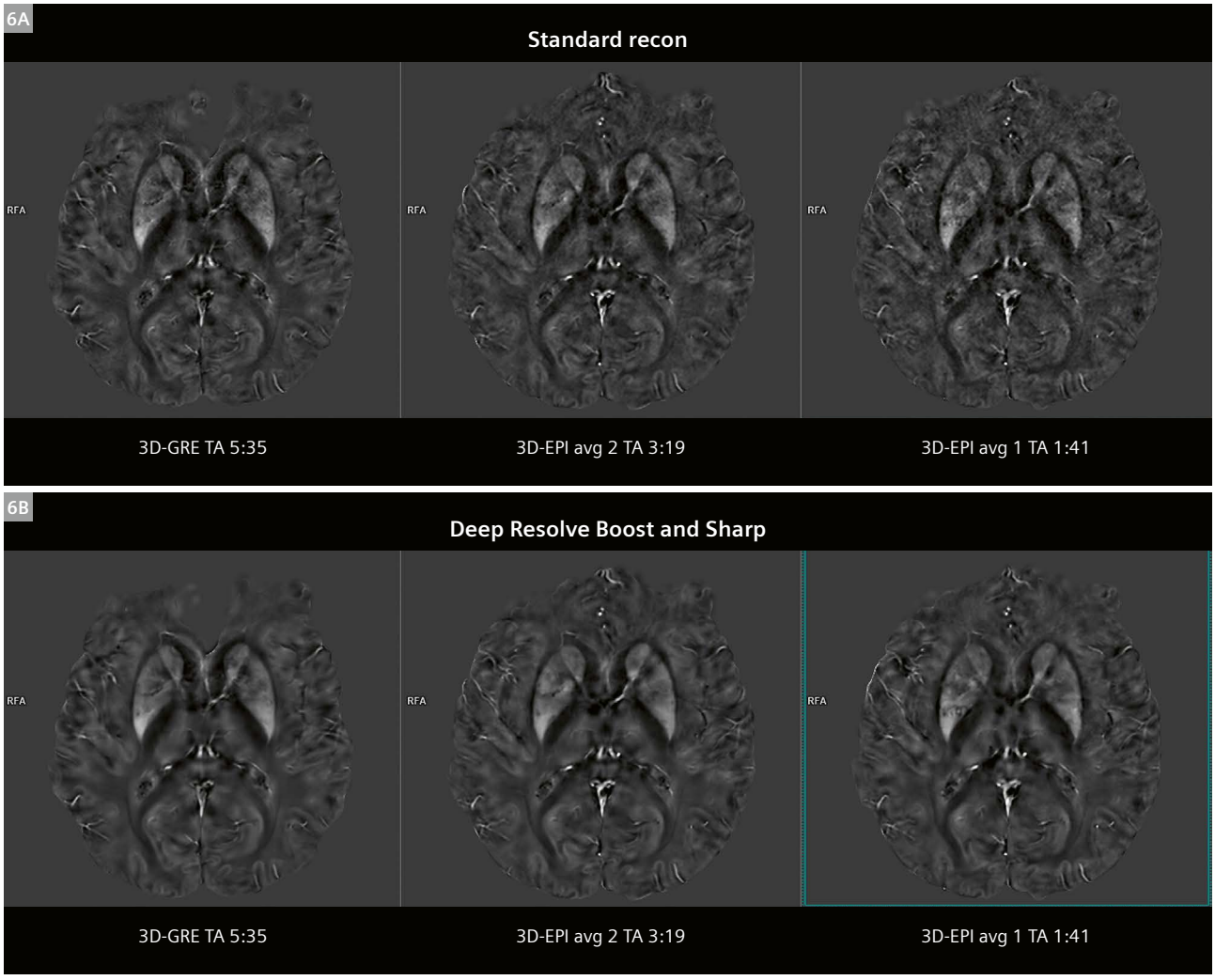

6 QSM maps scaled to [-100, 300] ppb from different sequences, 3D-GRE and 3D-EPI, and different image reconstructions. **(6A)** 3D-EPI used matched parameters with an echo time of 20 ms compared to 3D-GRE. The EPI factor of five in 3D-EPI compared to five echoes with 3D-GRE makes this sequence approx. four times faster. The QSM contrast-to-noise ratio decreases with the faster acquisition (left to right). **(6B)** Using the 3D deep learning *k*-space-to-image reconstruction (Deep Resolve Boost) could mostly preserve the QSM image quality even with an approx. 4-time increase in speed.

Imaging parameters: FOV 224 × 224 mm², 64 slices, resolution 0.35 × 0.35 × 2.0 mm³ (interpolated), PAT 3, standard reconstruction vs. Deep Resolve Boost and Sharp, TGV algorithm.
3D-GRE: 5 TEs 6.6 – 34 ms, $TE_{average}$ 20 ms, TR 39 ms, FA 15°, BW 200 Hz/px, TA 5:35 min.
3D-EPI: TE 20 ms, TR 56 ms, FA 21°, BW 284 Hz/px, EF 5, TA 3:19 / 1:41 min with avg 2 / 1.

Nigrosome 1 ("swallow tail") imaging in substantia nigra

Publications hint that SWI at 3T or 7T could potentially function as a novel imaging biomarker for idiopathic Parkinson's disease (IPD) [33] by improving the ability to observe the nigral hyperintensity or nigrosome 1. Recent studies [33] also propose that the novel SMWI methods may further enhance the ability to observe changes to nigrosome 1. These studies also provide evidence that the robust diagnostic performance of the novel SMWI methods remains consistent in a multicenter setting with various MRI scanners, indicating the potential applicability of SMWI in assessing nigrostriatal degeneration in individuals with parkinsonism.

Figure 7 displays QSM and SMWI images of a healthy subject, with slices planned along the AC–PC line. The nigrosome 1 "swallow tail" in the substantia nigra is clearly highlighted in both QSM and SMWI images (Fig. 7A). The SMWI image is presented in 3D orthogonal planes of nigrosome 1 (Fig. 7B).

Notably, using a 64-channel head-neck coil, the 0.65 mm isotropic dataset with whole-brain coverage was acquired in a total time of 3:12 min. This efficiency is achieved through (1) effective sampling with 3D-EPI and (2) employing 3D deep learning *k*-space-to-image reconstruction (Deep Resolve Boost).

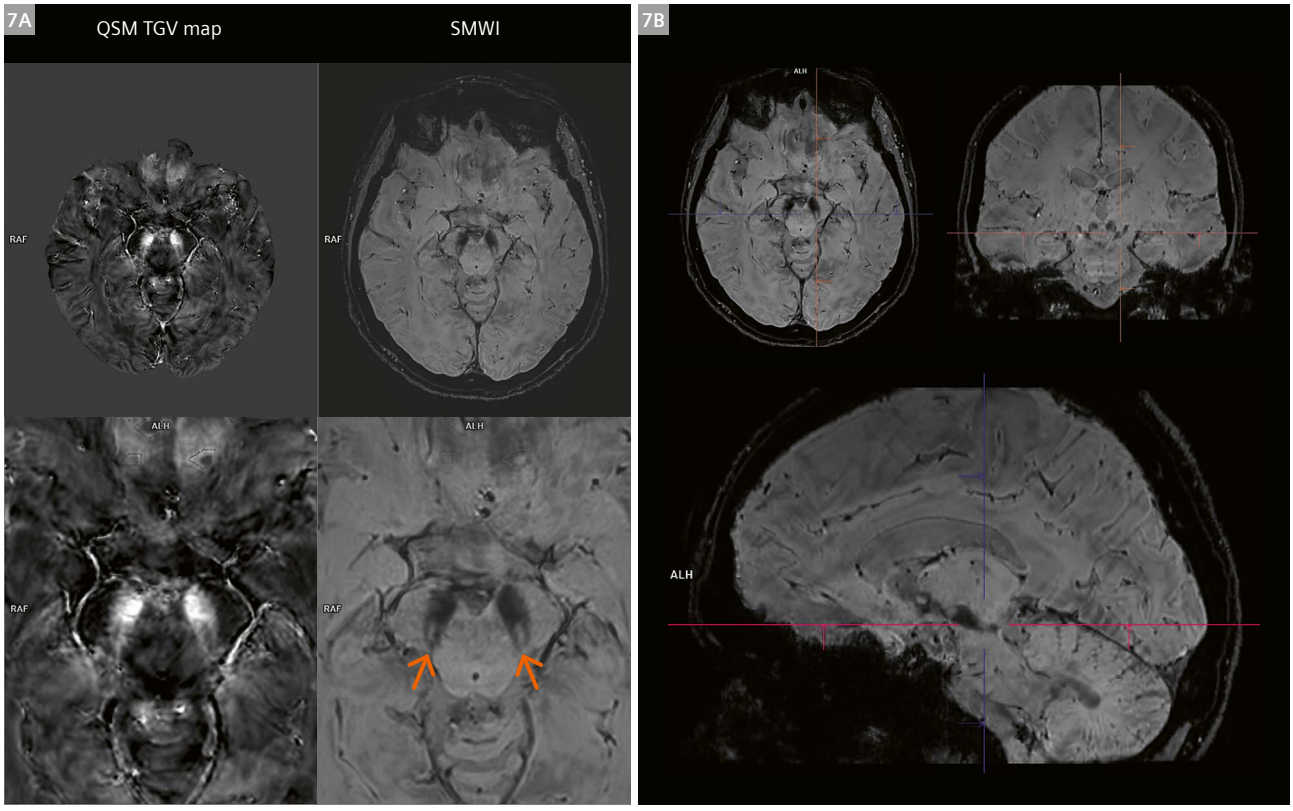

7 QSM and SMWI of a healthy subject with slices planned along the AC–PC line. **(7A)** The nigrosome 1 "swallow tail" in the substantia nigra is nicely contrasted in both QSM and SMWI images. **(7B)** SMWI image in 3D orthogonal planes of nigrosome 1. Remarkably, the 0.65 mm^3 isotropic dataset with whole-brain coverage could be acquired in 3:12 min using a 64-channel head-neck coil. This is made possible by using (1) efficient sampling with 3D-EPI and (2) 3D deep learning *k*-space-to-image reconstruction (Deep Resolve Boost).

Imaging parameters:

3D-EPI: FOV 250 × 250 mm^2, 196 slices, resolution 0.33 × 0.33 × 0.65 mm^3 (interpolated), TE 27 ms, TR 51 ms, FA 15°, BW_{RO} 651 Hz/px, BW_{PE} 30 Hz/px (46 Hz/mm), EF 19, slcOS 14%, slcPF 6/8, PAT 2, Deep Resolve Boost and Sharp, avg 2, TA 3:12 min.

Conclusions

In conclusion, this article showcases significant advancements in Susceptibility-Weighted Imaging (SWI) and Quantitative Susceptibility Mapping (QSM) techniques, offering notable improvements in image quality and diagnostic potential. Through utilization of 3D Laplacian phase unwrapping, SWI processing demonstrates enhanced signal recovery and reduced artifacts in areas of high susceptibility. The implementation of multi-echo 3D-GRE techniques further enhances signal-to-noise ratio in SWI images.

The introduction of QSM and SMWI emerges as a promising approach to achieve superior diagnostic performance compared to SWI alone. The synergy of efficient sampling techniques such as 3D-EPI and 3D deep learning *k*-space-to-image reconstruction (Deep Resolve Boost) can significantly accelerate the image acquisition while preserving image quality for these novel clinical imaging techniques.

These advancements contribute to the evolving landscape of neuroimaging, paving the way for enhanced diagnostic accuracy and efficiency in evaluating neurodegenerative disorders. The search for and validation of clinically valuable biomarkers, such as the improved visualization of nigrosome 1 and the "swallow tail" sign for idiopathic Parkinson's disease, are now more accessible through this research.

Acknowledgments

The collaborative development of the QSM and 3D-EPI research package involved Professor Markus Barth and his team at the Center for Advanced Imaging, The University of Queensland, Australia, which includes Monique Tourell and Saskia Bollmann.

Jinsuh Kim from Emory University School of Medicine, Atlanta, USA (present address), played a pivotal role in developing the TGV GPU code in collaboration with Christian Langkammer and Kristian Bredies from the University of Graz, Austria.

The ROMEO code was developed through a collaboration with Professor Simon Robinson from the High Field MR Center, Medical University of Vienna, Austria, and Barbara Dymerska from the Wellcome Centre for Human Neuroimaging, University College London, UK.

Professors Pascal Spincemaille and Yi Wang from the Cornell MRI Research Lab, NY, USA, provided the QSM MEDI code.

Dr. Sylvie Grand and Professor Alexandre Krainik from CHU Grenoble, France, and Marylene Delcey, Siemens Healthineers, France, contributed the patient SWI data presented in Figure 2. Protocol optimization and subject data for Figure 7 were provided by Melanie Adam, master's student at Siemens Healthineers, Erlangen, Germany.

The authors express their gratitude to Professor Jongho Lee from the Department of Electrical and Computer Engineering, and to Professor Eung Yeop Kim from Radiology at Samsung Medical Center, Seoul, Korea, for their insightful discussions about Susceptibility Map-Weighted Imaging.

References

1 Reichenbach JR, Haacke EM. High-resolution BOLD venographic imaging: a window into brain function. NMR Biomed. 2001; 14(7–8):453–67.
2 Haacke EM, Mittal S, Wu Z, Neelavalli J, Cheng YC. Susceptibility-weighted imaging: technical aspects and clinical applications, part 1. AJNR Am J Neuroradiol. 2009;30(1):19–30.
3 Mittal S, Wu Z, Neelavalli J, Haacke EM. Susceptibility-weighted imaging: technical aspects and clinical applications, part 2. AJNR Am J Neuroradiol. 2009;30(2):232–52.
4 Wang Y, Spincemaille P, Liu Z, Dimov A, Deh K, Li J, et al. Clinical quantitative susceptibility mapping (QSM): Biometal imaging and its emerging roles in patient care. J Magn Reson Imaging. 2017;46(4):951–971.
5 Eckstein K, Bachrata B, Hangel G, Widhalm G, Enzinger C, Barth M, et al. Improved susceptibility weighted imaging at ultra-high field using bipolar multi-echo acquisition and optimized image processing: CLEAR-SWI. Neuroimage. 2021;237:118175.
6 Cummings J, Rabinovici GD, Atri A, Aisen P, Apostolova LG, Hendrix S, et al. Aducanumab: Appropriate Use Recommendations Update. J Prev Alzheimers Dis. 2022;9(2):221–230.
7 Duyn J. MR susceptibility imaging. J Magn Reson. 2013;229: 198–207.
8 Haacke EM, Liu S, Buch S, Zheng W, Wu D, Ye Y. Quantitative susceptibility mapping: current status and future directions. Magn Reson Imaging. 2015;33(1):1–25.
9 Wang Y, Liu T. Quantitative susceptibility mapping (QSM): Decoding MRI data for a tissue magnetic biomarker. Magn Reson Med. 2015;73(1):82–101.
10 Chen W, Gauthier SA, Gupta A, Comunale J, Liu T, Wang S, et al. Quantitative susceptibility mapping of multiple sclerosis lesions at various ages. Radiology. 2014;271(1):183–92.
11 Langkammer C, Liu T, Khalil M, Enzinger C, Jehna M, Fuchs S, et al. Quantitative susceptibility mapping in multiple sclerosis. Radiology. 2013;267(2):551–9.
12 Li X, Harrison DM, Liu H, Jones CK, Oh J, Calabresi PA, et al. Magnetic susceptibility contrast variations in multiple sclerosis lesions. J Magn Reson Imaging. 2016 Feb;43(2):463–73.
13 Rahmanzadeh R, Galbusera R, Lu PJ, Bahn E, Weigel M, Barakovic M, et al. A New Advanced MRI Biomarker for Remyelinated Lesions in Multiple Sclerosis. Ann Neurol. 2022;92(3):486–502.
14 Schweser F, Deistung A, Lehr BW, Reichenbach JR. Differentiation between diamagnetic and paramagnetic cerebral lesions based on magnetic susceptibility mapping. Med Phys. 2010;37(10):5165–78.
15 Straub S, Laun FB, Emmerich J, Jobke B, Hauswald H, Katayama S, et al. Potential of quantitative susceptibility mapping for detection of prostatic calcifications. J Magn Reson Imaging. 2017;45(3): 889–898.
16 Alkemade A, de Hollander G, Keuken MC, Schäfer A, Ott DVM, Schwarz J, et al. Comparison of T2*-weighted and QSM contrasts in Parkinson's disease to visualize the STN with MRI. PLoS One. 2017;12(4):e0176130.
17 Devos D, Moreau C, Devedjian JC, Kluza J, Petrault M, Laloux C, et al. Targeting chelatable iron as a therapeutic modality in Parkinson's disease. Antioxid Redox Signal. 2014;21(2):195–210.

18 Bilgic B, Pfefferbaum A, Rohlfing T, Sullivan EV, Adalsteinsson E. MRI estimates of brain iron concentration in normal aging using quantitative susceptibility mapping. Neuroimage. 2012;59(3): 2625–35.
19 Acosta-Cabronero J, Williams GB, Cardenas-Blanco A, Arnold RJ, Lupson V, Nestor PJ. In vivo quantitative susceptibility mapping (QSM) in Alzheimer's disease. PLoS One. 2013;8(11):e81093.
20 Moon Y, Han SH, Moon WJ. Patterns of Brain Iron Accumulation in Vascular Dementia and Alzheimer's Dementia Using Quantitative Susceptibility Mapping Imaging. J Alzheimers Dis. 2016;51(3): 737–45.
21 Hwang EJ, Kim HG, Kim D, Rhee HY, Ryu CW, Liu T, et al. Texture analyses of quantitative susceptibility maps to differentiate Alzheimer's disease from cognitive normal and mild cognitive impairment. Med Phys. 2016;43(8):4718.
22 van Bergen JM, Hua J, Unschuld PG, Lim IA, Jones CK, Margolis RL, et al. Quantitative Susceptibility Mapping Suggests Altered Brain Iron in Premanifest Huntington Disease. AJNR Am J Neuroradiol. 2016;37(5):789–96.
23 Deistung A, Stefanescu MR, Ernst TM, Schlamann M, Ladd ME, Reichenbach JR, et al. Structural and Functional Magnetic Resonance Imaging of the Cerebellum: Considerations for Assessing Cerebellar Ataxias. Cerebellum. 2016;15(1):21–25.
24 Schweitzer AD, Liu T, Gupta A, Zheng K, Seedial S, Shtilbans A, et al. Quantitative susceptibility mapping of the motor cortex in amyotrophic lateral sclerosis and primary lateral sclerosis. AJR Am J Roentgenol. 2015;204(5):1086–92.
25 Sharma SD, Fischer R, Schoennagel BP, Nielsen P, Kooijman H, Yamamura J, et al. MRI-based quantitative susceptibility mapping (QSM) and R2* mapping of liver iron overload: Comparison with SQUID-based biomagnetic liver susceptometry. Magn Reson Med. 2017;78(1):264–270.
26 He Q, Liu Z, Wang Y, Du J. Ultrashort Echo Time Quantitative Susceptibility Mapping (UTE-QSM) of Cortical Bone. Proceedings of the 23rd Annual Meeting ISMRM Toronto, ON, Canada. 2015. Vol. 1725.
27 Polak D, Cauley S, Bilgic B, Wald L, Setsompop K. Ultrafast Multi-contrast High-resolution 3D Brain MRI: a Technical Description of Wave-CAIPI. ↗ MAGNETOM Flash.2020;76(1):17–20.
28 Filho ALG, Conklin J, Rapalino O, Schaefer P, Huang S. Ultrafast Multi-Contrast High-Resolution 3D Brain MRI: Clinical Evaluation of Wave-CAIPI Acceleration in SWI, MPRAGE, FLAIR, SPACE. ↗ MAGNETOM Flash.2020;76(1):21–27.
29 Langkammer C, Bredies K, Poser BA, Barth M, Reishofer G, Fan AP, et al. Fast quantitative susceptibility mapping using 3D EPI and total generalized variation. Neuroimage. 2015;111:622–30.
30 Stewart AW, Robinson SD, O'Brien K, Jin J, Widhalm G, Hangel G, et al. QSMxT: Robust masking and artifact reduction for quantitative susceptibility mapping. Magn Reson Med. 2022;87(3):1289–1300.
31 Dymerska B, Eckstein K, Bachrata B, Siow B, Trattnig S, Shmueli K, et al. Phase unwrapping with a rapid opensource minimum spanning tree algorithm (ROMEO). Magn Reson Med. 2021;85(4): 2294–2308.
32 Liu J, Liu T, de Rochefort L, Ledoux J, Khalidov I, Chen W, et al. Morphology enabled dipole inversion for quantitative susceptibility mapping using structural consistency between the magnitude image and the susceptibility map. Neuroimage. 2012;59(3): 2560–8.
33 Sung YH, Kim JS, Yoo SW, Shin NY, Nam Y, Ahn TB, et al. A prospective multi-centre study of susceptibility map-weighted MRI for the diagnosis of neurodegenerative parkinsonism. Eur Radiol. 2022;32(5):3597–3608.
34 Gho SM, Liu C, Li W, Jang U, Kim EY, Hwang D, et al. Susceptibility map-weighted imaging (SMWI) for neuroimaging. Magn Reson Med. 2014;72(2):337–46.
35 Jin J, Tourell M, Sati P, Liu K, Derbyshire J, O'Brien K, et al. Segmented 3D EPI with CAIPIRINHA for Fast, High-Resolution T2*-weighted Imaging. Proceedings of the Annual Meeting ISMRM 2021.
36 Jin J, Nickel D, Pfeuffer J, Tourell M, Stewart A, Bollmann S. Fast, High-resolution Whole Brain SWI and QSM with CAIPIRINHA 3D-EPI and Deep Learning Reconstruction. Proceedings of the Annual Meeting ISMRM 2024.

Contact

Dr. Josef Pfeuffer
Siemens Healthineers AG
SHS DI MR RCT CLS NEUR
Erlangen
Germany
josef.pfeuffer@siemens-healthineers.com


Josef Pfeuffer


Steffen Bollmann


Korbinian Eckstein


Ashley Wilton Stewart

Insights from 7T: GRE T2*-weighted Sequences Uncover Biomarkers in Neurological Diseases

Jing Jing[1,2]; Zhe Zhang[1]; Decai Tian[2]; Tao Feng[2]; Hua Pan[2]; Yuan Li[3]; Xiaoye Wang[3]; Jianxun Qu[3]

[1] Tiantan Neuroimaging Center of Excellence, China National Clinical Research Center for Neurological Diseases, Beijing Tiantan Hospital, Capital Medical University, Beijing, China
[2] Department of Neurology, Beijing Tiantan Hospital, Capital Medical University, Beijing, China
[3] Siemens Healthineers, Beijing, China

Introduction

MRI is the cornerstone for imaging neurological disease. Clinical diagnostic routines typically employ 3T MRI, but difficulties persist in distinguishing similar signs from multiple neurodegenerative disorders and providing precise biomarkers for a specific disease.

The emergence of ultra-high-field magnetic resonance imaging (UHF MRI) at 7T holds promise for tackling these obstacles, given its capacity to generate higher-resolution images and offer distinct contrasts due to a higher susceptibility effect and different relaxation time constants. Both enhancing diagnostic precision and introducing novel applications in neuro imaging are possible with this advancement. Previous publications [1–5] have demonstrated the advantages of UHF in diagnostics, leading to recognition by physicians of the clinical use of 7T.

GRE T2*-weighted imaging (T2*WI) is a fast, convenient, noninvasive, and feasible technique that exhibits advantages in clinical settings. T2*W sequences make it easier to identify lesions in the local magnetic field, such as bleeding and hemosiderin accumulation. Structures with slightly different magnetic properties introduce detectable field variations at high B0, which leads to a noticeable increase in lesion identification in 7T.

SWI in Wilson disease [6]

Wilson disease (WD), also known as hepatolenticular degeneration, is a rare inherited autosomal recessive disorder caused by variants in ATP7B, leading to pathologic copper accumulation mainly in the liver and brain [7]. WD patients with neurologic manifestations such as parkinsonism, dysarthria, and postural tremor are classified as neurologic WD (NWD) [8–10]. Early diagnosis of NWD is crucial because early treatment can prevent irreversible neurologic sequelae.

With submillimeter spatial resolution and increased tissue contrast, susceptibility-weighted imaging in ultra-high-field 7T MRI is superior to 3T MRI [11, 12]. 7T SWI could be used to identify a distinctive pattern of metal deposition in NWD, which could increase the accuracy of NWD diagnosis.

In this cross-sectional diagnostic study, we identified a distinctive pattern of metal deposition in NWD using 7T SWI, termed “hyperintense globus pallidus rim sign,” which demonstrated excellent diagnostic performance.

Figure 1 shows the distinct pattern between Parkinson's disease (PD) and WD. For a visible lateral border of the globus pallidus in WD patients, a clear and continuous boundary and a profound increase in the signal of the

lateral border of the globus pallidus and internal border of the putamen were identified as the standard of score 2, while an unclear or discontinuous boundary and a mild increase were identified as score 1.

Figure 2 demonstrates the distinct hyperintense globus pallidus rim sign among NWD, PD, and nNWD patients.

In our detailed study, more specific neurological diseases were compared with NWD [6]. It was observed in 38 of the 41 patients with NWD and was absent in all patients with nNWD, early-onset Parkinson's disease (EOPD), multiple system atrophy (MSA), progressive supranuclear palsy (PSP), and neurodegeneration with brain iron accumulation (NBIA), as well as monoallelic ATP7B variant carriers and HC in our study. Moreover, the scoring criteria of the hyperintense globus pallidus rim sign proved useful in monitoring neurologic severity of NWD. The hyperintense globus pallidus rim sign demonstrated excellent diagnostic sensitivity and specificity (92.7% and 100%, respectively). Although efforts have been made to identify specific imaging characteristics of WD, such as the "face of the giant panda," "miniature panda," "split thalamus," "bright claustrum," and "whorl" signs, these features have been associated with edema, demyelination, gliosis, and brain atrophy, all of which are common among neurodegenerative metabolic diseases [13–15]. T2/SWI hypointensity was also detected in nNWD, EOPD, MSA, PSP, and NBIA patients, indicating its low diagnostic specificity compared with the hyperintense globus pallidus rim sign. In addition, we found high prevalence of the hyperintense globus pallidus rim sign in drug-naive NWD subgroups, reflecting its high diagnostic efficacy. As brain MRI is used in the current diagnostic process of NWD [16], the novel hyperintense globus pallidus rim sign can improve the diagnostic accuracy of NWD.

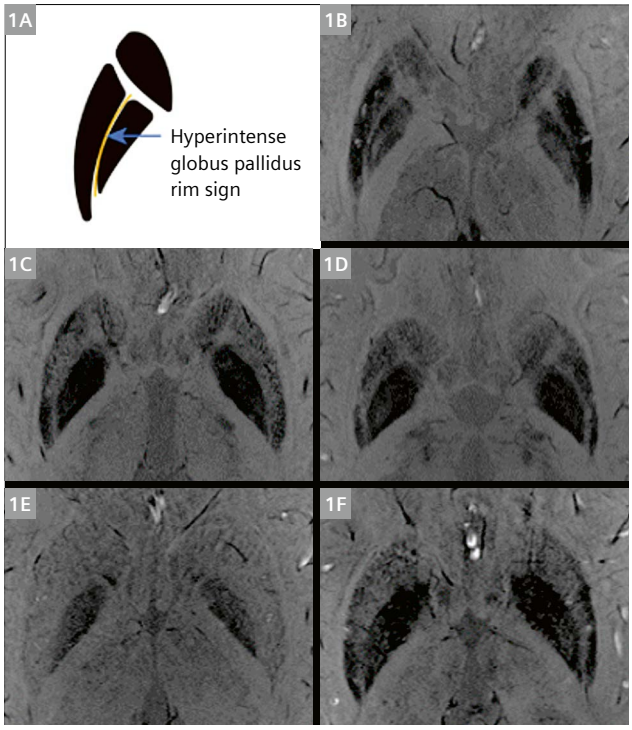

1 **(1A)** A diagram of the hyperintense globus pallidus rim sign with a linear hyperintensity (arrow) at the lateral border of the globus pallidus and a hypointense signal of the globus pallidus and putamen on the axial SWI image of the basal ganglia. **(1B)** Scoring criteria of the hyperintense globus pallidus rim sign show NWD patients with a score of 1 **(1C)** and a score of 2 **(1D)** on both sides, and nNWD **(1E)** and PD patients **(1F)** with a score of 0 on both sides.
PD = Parkinson's disease; nNWD = nonneurologic Wilson disease; NWD = neurologic Wilson disease; SWI = susceptibility-weighted imaging

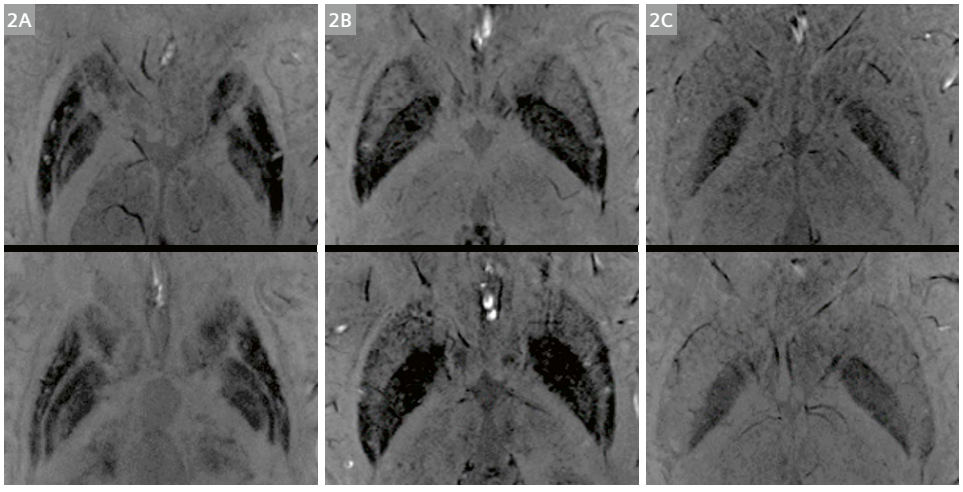

2 Axial 7T SWI images of the basal ganglia in typical patients with NWD **(2A)**, PD **(2B)**, and nNWD patients **(2C)**. The hyperintense globus pallidus rim sign is only observed in patients with NWD.
PD = Parkinson's disease; NWD = neurologic Wilson disease; nNWD = nonneurologic Wilson disease; SWI = susceptibility-weighted imaging.

SWI in primary angiitis of the central nervous system [2]

Primary angiitis of the central nervous system (PACNS) is an inflammatory disorder of the central nervous system (CNS) characterized by an unexplained vasculitis confined to the brain, spinal cord, and leptomeninges, with an estimated annual incidence of 2.4 per million [17–19]. Biopsy-confirmed PACNS typically affects small vessels and is more likely to have normal magnetic resonance angiography (MRA) [20].

7T MRI, with its increased signal-to-noise ratio and enhanced contrast in susceptibility-sensitive sequences, such as susceptibility-weighted imaging (SWI), offers new possibilities.

All patients presented with supratentorial lesion. Parietal, frontal, and temporal lobe involvement was frequently observed. Cortical microhemorrhage presentation in patients with PACNS has been under-characterized, mainly being limited to single-case reports [21, 22]. In our cohort, patients with microhemorrhages accounted for 57.14%, which was higher than the hemorrhagic manifestation in most previous reports [23–26]. This discrepancy may be attributed to the increased sensitivity of 7T MRI in detecting hemorrhages, as well as the historical underuse of SWI in MRI protocols. Figure 3 demonstrates that subtle gyriform microhemorrhages were significantly conspicuous on 7T MRI [27]. These microhemorrhages were not visible on 3T MRI. The detailed portrayal of hemorrhage morphology achievable with 7T MRI suggests that microhemorrhages have relatively higher specificity and warrant further in-depth investigation.

The high spatial resolution of 7T MRI allowed us to identify a coral-like sign (Fig. 3), characterizing the microhemorrhages in SV-PACNS as cortical clusters of petechiae or ribbons, rarely appearing as isolated punctures. This capability to improve the delineation of small anatomical structures and subtle pathologies, especially with SWI, underscores the benefits of high magnetic field characteristics. Our findings suggest that 7T MRI may enhance diagnostic reliability among multiple readers. Many diseases mimicking PACNS also have cerebral microhemorrhages, such as small vessel disease, chronic hypertension, immunoglobulin (Ig) G4-related disease, Susac syndrome, lupus anticoagulant-hypoprothrombinemia syndrome, neurosarcoidosis, Sneddon's syndrome, cerebral amyloid angiopathy (CAA), and intravascular lymphoma [19, 28–35]. Distinguishing PACNS from other conditions that also present with cerebral microhemorrhages requires detailed imaging. Clinical characteristics, other examinations, and prognoses are also necessary for differential diagnoses. Further investigation is needed to determine whether intracortical vessels distributed in the cortex have distinctive immunological properties.

T2*W in multiple sclerosis (MS)[3]

Cranial nerve involvement is a prominent characteristic of multiple sclerosis (MS) lesions, with the optic nerve being the most frequently affected, followed by the trigeminal nerve. The prevalence of trigeminal involvement varies widely, ranging from 2.9% to 23%, depending on MRI resolution, sequence selection, and also disease duration [36–43]. Additionally, patients with MS have a 15-fold increased risk of developing trigeminal neuralgia (TN), compared with the general neurological outpatient population. Histologic evidence has demonstrated focal demyelination at the root entry zone (REZ) in MS-related TN. A general consensus exists on the close association of the trigeminal nerve root with the vascular anatomy, which may trigger TN [44].

The utilization of ultra-high-field 7T MRI, with its increased SNR and enhanced susceptibility effects, yields superior visualization of the lesions and provides further insights into their possible pathology. Previous studies

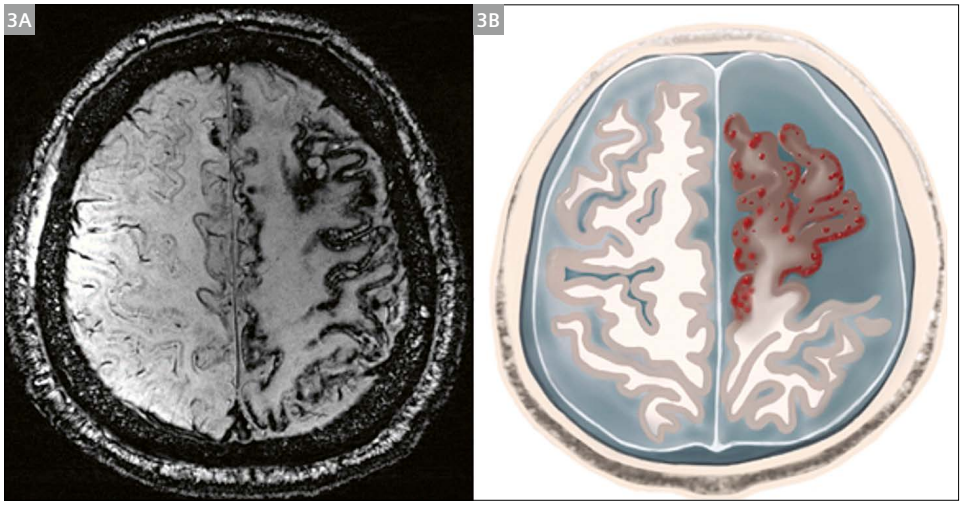

3 The "coral-like sign" is defined as a cerebral cortical diffuse microhemorrhage with cortical atrophy in the axial gradient echo sequence, which is related to small vessel primary angiitis of the central nervous system (SV-PACNS). **(3A)** Microhemorrhage restricted to the cortices on the susceptibility-weighted imaging. **(3B)** Pattern diagram of coral-like sign.

have mainly focused on MS-related TN with consecutive routine MRI scans, leading to potential underestimation of the prevalence of trigeminal nerve lesions in asymptomatic patients.

Figure 4 shows that FLAIR* axial images identified a dark vein located centrally in the majority of the trigeminal lesion (arrowheads), especially in the REZ. The bottom MPRAGE-MRA and T2*-weighted images on the axial plane demonstrate neurovascular compression.

In this pioneering 7T MRI consecutive cohort of patients with early MS in China, we observed a notable proportion of trigeminal involvement, with 15.8% of patients exhibiting such lesions with most of these lesions being clinically silent. Moreover, a central vein sign (CVS) was detected in 26.9% of lesions of the REZ. Notably, our study highlights the presence of MRI detectable CVS in linearly shaped demyelinating plaque located along the intramedullary trigeminal root, indicative of a central (oligodendroglia type of) myelin lesion. 57.8% of the lesions were located in the REZ, of which 26.9% had a CVS.

The prevalence of trigeminal nerve involvement in previous MS research varies from 2.9% to 23%, owing to differences in selection bias in various cohorts and MRI resolution. In fact, in most cohorts, studying the prevalence of trigeminal involvement primarily focused on a history of MS-related TN, which introduces potential bias [37, 38, 42]. Indeed, some patients with trigeminal nerve lesions may not manifest symptoms until several years after the lesion is detected on MRI, which is consistent with our finding that some patients had trigeminal nerve lesions without having TN [38]. While prior studies used the whole range from 0.1 to 3T MRI, we used 7T MRI, which has high SNR and significantly improves spatial resolution, thereby enabling the accurate detection of anatomical and pathological features.

Sequence	TE/TR ms	Parallel imaging factor	FA degree	Slice number	Voxel size mm^3	Acquisition time min:s
SWI for WD	12/19	3	14	104	0.15 × 0.15 × 1.2	6:47
SWI for PACNS	12/19	3	14	120	0.15 × 0.15 × 1.2	7:45
Multi-echo T2*W	(10, 20, 30)/2500	3	50	56	0.14 × 0.14 × 1.2	9:34

Table 1: Method

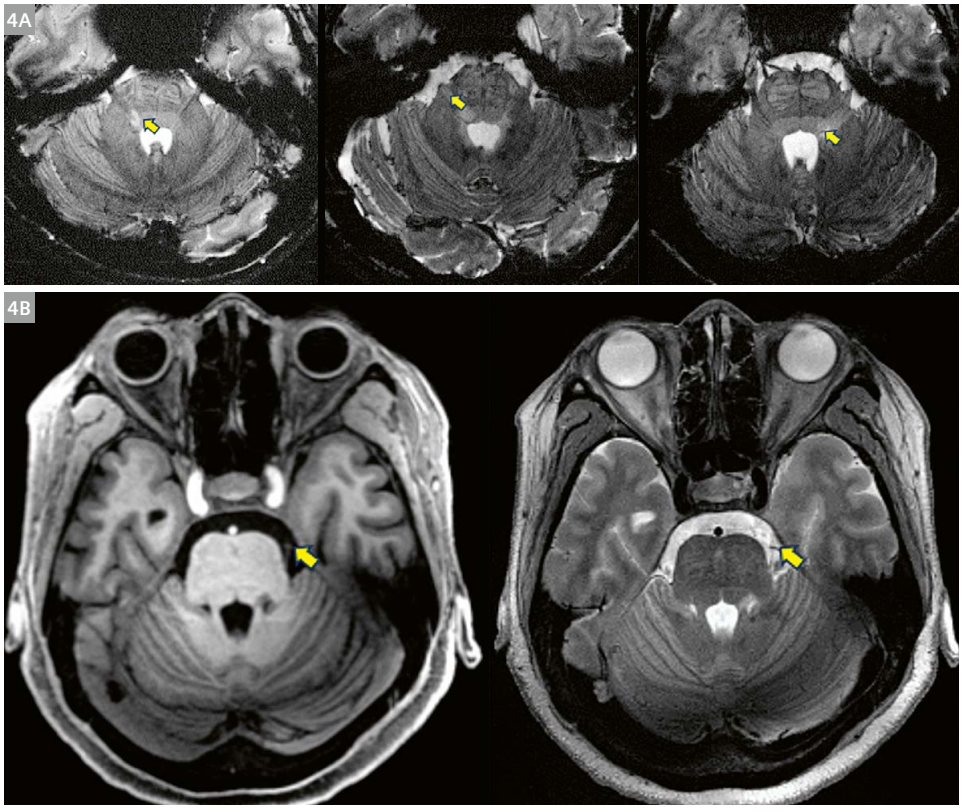

4 **(4A)** 7T FLAIR* axial images demonstrate a dark vein located centrally in the majority of the trigeminal lesion (arrowheads), especially in the REZ. **(4B)** 7T MPRAGE-MRA on the axial plane demonstrates neurovascular compression. The arrowhead indicates the vessels touching the trigeminal nerve. MPRAGE-MRA, magnetization-prepared rapid acquisition with gradient echo-magnetic resonance angiography.

Other biomarkers

Other biomarkers are e.g., motor band sign in amyotrophic lateral sclerosis (ALS) patients.

The motor band sign, defined as hypointensities in the primary motor cortex on T2-, T2*- or susceptibility-weighted imaging (SWI), is associated with degenerative iron accumulations in the cortical regions. Figure 5 demonstrated clear bilateral motor band sign on one ALS patient. Higher resolution and susceptibility effect in 7T MRI enabled superior visualization of this biomarker. A larger patient cohort will be included in the future study.

Conclusion and perspectives

T2*W GRE sequences in 7T MRI notably enhance resolution, providing greater confidence for identifying clinical biomarkers. Several biomarkers for neurological disorders emerged from the collaboration between Siemens Healthineers and Tiantan Hospital. These imaging biomarkers augment the current clinical norm and could be used to initiate investigation of pathological pathways. We will need to do more research that combines comprehensive prospective and longitudinal research to find out how often, how sensitive, and how suggestive these biomarkers are and how well they work as a prognostic indicator.

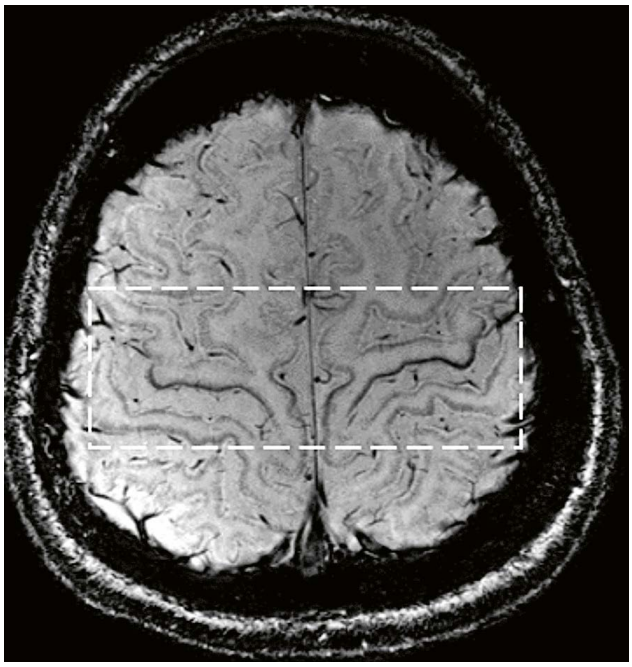

5 Bilateral motor band sign on the cortices on SWI.

References

1 Burkett BJ, Fagan AJ, Felmlee JP, Black DF, Lane JI, Port JD, et al. Clinical 7-T MRI for neuroradiology: strengths, weaknesses, and ongoing challenges. Neuroradiology. 2021;63(2):167–177.
2 Guo A, Zhang Z, Dong GH, Su L, Gao C, Zhang M, et al. Cortical Microhemorrhage Presentation of Small Vessel Primary Angiitis of the Central Nervous System. Ann Neurol. 2024;96(1):194–203.
3 Jing J, Zhang Z, Su L, Gao C, Guo A, Liu X, et al. Central vein sign and trigeminal lesions of multiple sclerosis visualised by 7T MRI. J Neurol Neurosurg Psychiatry. 2024;95(8):761–766.
4 Kidwell CS, Saver JL, Villablanca JP, Duckwiler G, Fredieu A, Gough K, et al. Magnetic resonance imaging detection of microbleeds before thrombolysis: an emerging application. Stroke. 2002;33(1):95–8.
5 Zhang Z, Kong Q, Zhang Y, Zhu W, Wei N, Xu Y, et al. Improved characterization of lenticulostriate arteries using compressed sensing time-of-flight at 7T. Eur Radiol. 2023;33(10):6939–6947.
6 Su D, Zhang Z, Zhang Z, Zheng S, Yao T, Dong Y, et al. Distinctive Pattern of Metal Deposition in Neurologic Wilson Disease: Insights From 7T Susceptibility-Weighted Imaging. Neurology. 2024;102(12):e209478.
7 Członkowska A, Litwin T, Dusek P, Ferenci P, Lutsenko S, Medici V, et al. Wilson disease. Nat Rev Dis Primers. 2018;4(1):21.
8 Ferenci P, Caca K, Loudianos G, Mieli-Vergani G, Tanner S, Sternlieb I, et al. Diagnosis and phenotypic classification of Wilson disease. Liver Int. 2003;23(3):139–42.
9 Shribman S, Poujois A, Bandmann O, Czlonkowska A, Warner TT. Wilson's disease: update on pathogenesis, biomarkers and treatments. J Neurol Neurosurg Psychiatry. 2021;92(10):1053–1061.
10 Walter U, Krolikowski K, Tarnacka B, Benecke R, Czlonkowska A, Dressler D. Sonographic detection of basal ganglia lesions in asymptomatic and symptomatic Wilson disease. Neurology. 2005;64(10):1726–32.
11 Cong F, Liu X, Liu CJ, Xu X, Shen Y, Wang B, et al. Improved depiction of subthalamic nucleus and globus pallidus internus with optimized high-resolution quantitative susceptibility mapping at 7 T. NMR Biomed. 2020;33(11):e4382.
12 Yao B, Li TQ, Gelderen Pv, Shmueli K, de Zwart JA, Duyn JH. Susceptibility contrast in high field MRI of human brain as a function of tissue iron content. Neuroimage. 2009;44(4):1259–66.
13 Prashanth LK, Sinha S, Taly AB, Vasudev MK. Do MRI features distinguish Wilson's disease from other early onset extrapyramidal disorders? An analysis of 100 cases. Mov Disord. 2010;25(6):672–8.

14 Rędzia-Ogrodnik B, Członkowska A, Antos A, Bembenek J, Kurkowska-Jastrzębska I, Przybyłkowski A, et al. Pathognomonic neuroradiological signs in Wilson's disease - Truth or myth? Parkinsonism Relat Disord. 2023;107:105247.
15 Zhong W, Huang Z, Tang X. A study of brain MRI characteristics and clinical features in 76 cases of Wilson's disease. J Clin Neurosci. 2019;59:167–174.
16 European Association for Study of Liver. EASL Clinical Practice Guidelines: Wilson's disease. J Hepatol. 2012;56(3):671–85.
17 Hajj-Ali RA, Singhal AB, Benseler S, Molloy E, Calabrese LH. Primary angiitis of the CNS. Lancet Neurol. 2011;10(6):561–72.
18 Salvarani C, Brown RD Jr, Calamia KT, Christianson TJ, Weigand SD, Miller DV, et al. Primary central nervous system vasculitis: analysis of 101 patients. Ann Neurol. 2007;62(5):442–51.
19 Twilt M, Benseler SM. The spectrum of CNS vasculitis in children and adults. Nat Rev Rheumatol. 2011;8(2):97–107.
20 Schuster S, Bachmann H, Thom V, Kaufmann-Buehler AK, Matschke J, Siemonsen S, et al. Subtypes of primary angiitis of the CNS identified by MRI patterns reflect the size of affected vessels. J Neurol Neurosurg Psychiatry. 2017;88(9):749–755.
21 Arias M, Osorio X, Dapena D, Arias-Rivas S, Vázquez F. Recurrent leukoencephalopathy with microhemorrhages: gradient-echo MRI study diagnostic value in CNS primary angiitis. Mult Scler. 2008;14(8):1139–41.
22 Ay H, Sahin G, Saatci I, Söylemezoğlu F, Saribaş O. Primary angiitis of the central nervous system and silent cortical hemorrhages. AJNR Am J Neuroradiol. 2002;23(9):1561–3.
23 Beuker C, Strunk D, Rawal R, Schmidt-Pogoda A, Werring N, Milles L, et al. Primary Angiitis of the CNS: A Systematic Review and Meta-analysis. Neurol Neuroimmunol Neuroinflamm. 2021;8(6):e1093.
24 de Boysson H, Parienti JJ, Mawet J, Arquizan C, Boulouis G, Burcin C, et al. Primary angiitis of the CNS and reversible cerebral vasoconstriction syndrome: A comparative study. Neurology. 2018;91(16):e1468–e1478.
25 Salvarani C, Brown RD Jr, Christianson TJH, Huston J 3rd, Giannini C, Hunder GG. Long-term remission, relapses and maintenance therapy in adult primary central nervous system vasculitis: A single-center 35-year experience. Autoimmun Rev. 2020;19(4):102497.
26 Salvarani C, Brown RD Jr, Hunder GG. Adult primary central nervous system vasculitis. Lancet. 2012;380(9843):767–77.
27 Haacke EM, Xu Y, Cheng YC, Reichenbach JR. Susceptibility weighted imaging (SWI). Magn Reson Med. 2004;52(3):612–8.
28 Yao M, Zhao J, Jiang N, Li L, Ni J. Superficial Siderosis and Microbleed Restricted in Cortex Might Be Correlated to Atrophy and Cognitive Decline in Sneddon's Syndrome. Front Neurol. 2020;11:1035.
29 Richie MB, Guterman EL, Shah MP, Cha S. Susceptibility-Weighted Imaging of Intravascular Lymphoma of the Central Nervous System. JAMA Neurol. 2022;79(1):86–87.
30 Charidimou A, Boulouis G, Gurol ME, Ayata C, Bacskai BJ, Frosch MP, et al. Emerging concepts in sporadic cerebral amyloid angiopathy. Brain. 2017;140(7):1829–1850.
31 Kammeyer R, Schreiner T. Cortical Vein Thrombosis, Tortuous Venous Vasculature, and Microhemorrhages in Neurosarcoidosis. JAMA Neurol. 2021;78(4):491–492.
32 Muccioli L, Nicodemo M, Rinaldi R, Vornetti G, Spinardi L. Hemorrhagic cerebral vasculopathy in Susac syndrome. Acta Neurol Belg. 2022;122(6):1599–1600.
33 Ukai K. Two cases of IgG4-related disease accompanied by many cerebral microbleeds and a review of the literature: can IgG4-related disease cause cerebral small vessel vasculitis/vasculopathy? Nagoya J Med Sci. 2021;83(3):649–654.
34 Viswanathan A, Chabriat H. Cerebral microhemorrhage. Stroke. 2006;37(2):550–5.
35 Jadhav AP, Aghaebrahim N, Jankowitz BT, Jovin TG. Cerebral microbleeds in lupus anticoagulant-hypoprothrombinemia syndrome. JAMA Neurol. 2013;70(11):1452–3.
36 Sugiyama A, Mori M, Masuda H, Uchida T, Muto M, Uzawa A, et al. Trigeminal root entry zone involvement in neuromyelitis optica and multiple sclerosis. J Neurol Sci. 2015;355(1-2):147–9.
37 da Silva CJ, da Rocha AJ, Mendes MF, Maia AC Jr, Braga FT, Tilbery CP. Trigeminal involvement in multiple sclerosis: magnetic resonance imaging findings with clinical correlation in a series of patients. Mult Scler. 2005;11(3):282–5.
38 Dilwali S, Mark I, Waubant E. MRI lesions can often precede trigeminal neuralgia symptoms by years in multiple sclerosis. J Neurol Neurosurg Psychiatry. 2023;94(3):189–192.
39 Swinnen C, Lunskens S, Deryck O, Casselman J, Vanopdenbosch L. MRI characteristics of trigeminal nerve involvement in patients with multiple sclerosis. Mult Scler Relat Disord. 2013;2(3):200–3.
40 Nakashima I, Fujihara K, Kimpara T, Okita N, Takase S, Itoyama Y. Linear pontine trigeminal root lesions in multiple sclerosis: clinical and magnetic resonance imaging studies in 5 cases. Arch Neurol. 2001;58(1):101–4.
41 van der Meijs AH, Tan IL, Barkhof F. Incidence of enhancement of the trigeminal nerve on MRI in patients with multiple sclerosis. Mult Scler. 2002;8(1):64–7.
42 Truini A, Prosperini L, Calistri V, Fiorelli M, Pozzilli C, Millefiorini E, et al. A dual concurrent mechanism explains trigeminal neuralgia in patients with multiple sclerosis. Neurology. 2016;86(22):2094–9.
43 Mills RJ, Young CA, Smith ET. Central trigeminal involvement in multiple sclerosis using high-resolution MRI at 3 T. Br J Radiol. 2010;83(990):493–8.
44 Love S, Coakham HB. Trigeminal neuralgia: pathology and pathogenesis. Brain. 2001;124(Pt 12):2347–60. Erratum in: Brain 2002;125(Pt 3):687.

Contact

Jing Jing, M.D.
Vice director, Tiantan Neuroimaging Center of Excellence
No. 119 West South Fourth Ring Road
Fengtai District, Beijing
China
jingj_bjttyy@163.com

Zhe Zhang, Ph.D.
Core faculty, Tiantan Neuroimaging Center of Excellence
No. 119 West South Fourth Ring Road
Fengtai District, Beijing
China
emailzhangzhe@gmail.com

ASNR-Recommended AD Therapeutic Imaging Protocols

Tammie L.S. Benzinger, M.D., Ph.D.; et al.

Washington University School of Medicine in St. Louis,
Mallinckrodt Institute of Radiology, St. Louis, MO, USA

Washington University School of Medicine shares their imaging protocols for 1.5T and 3T MRI systems at

MAGNETOM World > Clinical Corner > Protocols > Neurology / Neurography

The battle against Alzheimer's disease (AD) has been long and challenging. However, in recent years, novel Disease Modifying Therapies (DMTs) using monoclonal antibodies (mAbs) have been developed. While promising, these DMTs require careful monitoring of patients against adverse effects once the treatment begins. On brain MRI, these adverse effects present as Amyloid Related Imaging Abnormalities (ARIA) with vasogenic edema and/or sulcal effusion (ARIA-E) and/or microhemorrhages or superficial siderosis (ARIA-H). Standardized, appropriate protocols for dementia therapeutic imaging are important. The American Society for Neuroradiology (ASNR) has partnered with equipment manufacturers to present optimized AD therapeutic imaging protocols.

SIEMENS Healthineers

Using MR-Guided Focused Ultrasound in the Brain: Past, Present, and Future

Lain H. Gonzalez-Quarante, M.D.[1]; Alana A. Arcadi Da Silva, M.D.[1]; Pablo D. Domínguez, M.D., Ph.D.[2]; Marta Vidorreta, Ph.D.[3]; Giulia Frazzetta, M.Sc.[4]; Tessa Case, M.Sc.[4]; Marta Macias de la Corte Hidalgo, M.D.[5]; Arantza Gorospe, M.D.[5]; Iciar Aviles-Olmos, M.D., Ph.D.[5]; Carlos A. Sanchez-Catasus, Ph.D.[5,6]; Maria C. Rodriguez-Oroz, M.D., Ph.D.[5]; Jorge Guridi, M.D., Ph.D.[1]

[1] Department of Neurosurgery, Clínica Universidad de Navarra, Pamplona, Spain
[2] Department of Radiology, Clínica Universidad de Navarra, Pamplona, Spain
[3] Siemens Healthineers, Madrid, Spain
[4] Insightec Ltd, Haifa, Israel
[5] Department of Neurology, Clínica Universidad de Navarra, Pamplona, Spain
[6] Department of Nuclear Medicine and Molecular Imaging, University of Groningen, University Medical Center Groningen, Netherlands

What is MR-guided focused ultrasound (MRgFUS)?

Lesional brain surgery is a fundamental technique in the functional neurosurgery world. It has been investigated for decades and presented promising results long before novel pharmacological agents were introduced to treat movement disorders, psychiatric disorders, pain, and epilepsy. Ablative procedures were partially replaced by effective drugs during the 1960s and by deep brain stimulation (DBS) in the 1990s as a neuromodulation technique that might be partly reversible. In the last 10 to 15 years, however, the popularity of brain lesioning is experiencing a phoenix-like resurgence, due to the introduction and development of magnetic resonance-guided focused ultrasound (MRgFUS).

Little did Jacques and Pierre Curie (the latter won in 1903 the Physics Nobel Price together with his wife Marie Skłodowska-Curie and Henri Bequerel) know that their discovery of the piezoelectric effect* would have such groundbreaking consequences as MRgFUS. The use of focused ultrasound in medicine has been studied and investigated since the 1930s. The first ultrasound transducers were capable of creating thermal lesions, but there was no imaging technique that could give it anatomical precision or even a thermography system that could inform the treating team about the reached temperature, especially when a deep lesion was intended. Another important hurdle that was encountered in these early days of focused ultrasound lesioning, or ablation techniques, was the bone. In brain experiments, the investigators were forced to open a window in the skull (either a burr hole or a craniotomy) in order to deliver the ultrasound beams with control and accuracy. All these obstacles have been overcome gradually in the last 20–30 years, by advancements in phased array ultrasound transducers, algorithms accommodating skull penetration by sound waves, and the integration of MR imaging for accurate targeting and thermometry. The result is the ability of MRgFUS to perform brain lesions with sub-millimeter precision [1].

The remarkable targeting accuracy and incisionless nature of this modality have created a paradigm shift in the management of conditions such as chronic neuropathic pain (CNP), essential tremor (ET), and Parkinson's disease (PD). Furthermore, an expanding body of clinical evidence supports the efficacy and safety of MRgFUS ablation in treating psychiatric disorders and epilepsy [2–8]. Ongoing investigative trials are also exploring the use of medium-intensity or low-intensity focused ultrasound (LIFU) for blood-brain barrier (BBB) disruption, facilitating the targeted delivery of drugs, genes, and other therapeutic agents for autoimmune, neurodegenerative, and malignant diseases [1].

A downside of ablative techniques such as MRgFUS, in comparison to modulatory techniques such as DBS, is that ablation has been mostly done in a unilateral-only or staged bilateral approach due to a high incidence of speech and balance dysfunction with simultaneous bilateral thalamic lesions for tremor [9]. Some groups argue that this complication rate could be much lower today, due to advanced imaging, targeting, and patient selection methods [9]. Thus, an extremely important and evolving component in MRgFUS is target selection. Direct targeting

*Curie, Jacques; Curie, Pierre (1880). "Développement par compression de l'électricité polaire dans les cristaux hémièdres à faces inclinées" [Development, via compression, of electric polarization in hemihedral crystals with inclined faces]. Bulletin de la Société Minérologique de France. 3 (4): 90–93.

refers to identifying the desired structure based on direct imaging-based visualization, while indirect targeting refers to the use of stereotactic coordinates. For example, using diffusion tensor imaging (DTI) tractography to guide MRgFUS for ET, the dentatorubrothalamic tract (DRT) can be directly targeted, while avoiding the pyramidal tract and medial lemniscus, in order to improve clinical effect (tremor reduction) and minimize motor and sensory adverse events, respectively [10]. Tractography-based direct targeting is an evolving field that may improve patient outcomes using personalized neurophysiological findings.

Treatment planning is patient-specific and nowadays requires a CT and MRI head scan, which can be performed beforehand. The procedure itself is guided in real-time by MRI, providing updated patient information and continuous temperature monitoring to ensure safety and efficacy.

During the initial stage of sonication, a low amount of energy is used to attain a temperature within the range of 40–45°C. This stage is referred to as the "alignment phase" and serves to verify if the intended target area experiences a temperature increase. Subsequently, the power is gradually increased to achieve a moderate temperature (between 46–50°C). At this point, the treating team moves to the "verify phase", wherein the patient's symptoms are assessed, as they typically show a transient response under these temperatures. Safety is also evaluated with an examination ruling out adverse events (such as paresthesia, paresis, dysarthria, or dysmetria). Following the confirmation of effectiveness (i.e., tremor suppression) without any accompanying adverse events, the temperature is further raised to 55–60°C, in the final and definitive "treatment phase".

In spite of being regarded as a safe procedure, the following points should be noted regarding the eligibility of patients for MRgFUS. In terms of age, patients should be at least 18 years old, because there is a lack of experience in pediatric patients. A history of any implanted device that is not compatible with MRI, and/or severe claustrophobia, are other possible contraindications for undergoing MRgFUS. The use of antiplatelet or anticoagulant therapy has been classically considered a contraindication for MRgFUS, and the treating teams recommended discontinuing these drug therapies prior to MRgFUS treatments, similar to the advice with open procedures. Interestingly, a recent paper by Caston et al. reports a retrospective series of 40 patients who were safely treated with MRgFUS and did not interrupt their blood thinning therapy, either antiplatelet or anticoagulant drugs [11]. Another essential condition is that the patients are required to lie supine in the scanner for 2 to 3 hours and to communicate during the procedure, due to the need for clinical feedback from the patient. There are also some anatomical considerations to take into account, such as the skull density ratio (SDR), an average value of the ratio between the Hounsfield units of the cancellous bone and the cortical bone for each ultrasound beam trajectory; and the average skull thickness, measured in millimeters. The lower the SDR, the more difficult the treatment can become, both from a heating-efficiency and patient-tolerability point of view. The threshold value of SDR may vary between institutions and also throughout the learning curve of the treating team. In our center, we initially considered 0.35 as the cutoff value to consider a patient suitable for MRgFUS thermal ablation. In more recent cases, we have lowered this threshold to 0.30. A detailed interview with the patient is mandatory when addressing low-SDR cases, as the treatment can be longer and more uncomfortable for the patient. We have observed that a good skull thickness (the thinner the better; we usually consider a good thickness to be under 6–7 mm) may partially outweigh or compensate for a bad SDR score, although this observation warrants a well-designed study of all these technical and anatomical variables to draw appropriate conclusions.

Given the incisionless nature and safety profile of MRgFUS therapy, patients can be treated in an ambulatory or short-admission (24-hour) setting.

MRgFUS thalamotomy for essential tremor

Essential tremor (ET) is arguably one of the most common neurological condition, and its cause is still unknown. It has a worldwide prevalence of over 5% in people older than 60, although it can affect people of any age [12]. This progressive disease causes involuntary and uncontrollable rhythmic shaking, most frequently of the hands, but it can also involve the head and other body parts. The International Parkinson and Movement Disorder Society proposed a consensus statement on the classification of tremors in 2018, in which ET is defined as follows:

1) isolated tremor syndrome of bilateral upper limb action tremor,
2) having at least 3 years duration, with or without tremor in other locations (e.g., head, voice, lower limbs), and
3) absence of other neurological signs that could imply a different diagnosis [13].

Severe ET can interfere with the patient's essential daily activities such as eating, drinking, and writing, and thus can be disabling. In such cases, most patients seek medical attention to improve their condition. Surgical treatment is recommended when medication is no longer effective or not possible for the patient.

In accordance with Macchi and Jones's article on motor thalamic terminology [14], the primary afferents, from anterior to posterior, within the ventral and lateral nuclei include the ventralis oralis anterior (Voa), receiving input from the internal globus pallidus (GPi); the ventralis oralis posterior (Vop), receiving cerebellar afferents; the

ventral intermediate nucleus (VIM), receiving deep sensitivity from contralateral joints and muscles; and the ventrocaudalis (VC), receiving sensitivity from the medial lemniscus. VIM, also referred to as the posterior part of the ventral lateral nucleus (VLp) by Hirai and Jones, stands out as a prominent target in functional neurosurgery due to its exceptional response in tremor management. Cerebellar afferents, originating from the dentate, fastigial, and interpositus nuclei, traverse the superior cerebellar peduncle in the midbrain, passing laterally to the red nucleus and largely decussating to reach the thalamus from its ventral aspect. Cerebellothalamic terminations may synapse with one or several neurons or dendrites simultaneously, using the excitatory neurotransmitter, glutamic acid [15]. From the thalamus, cerebellar afferents project onto the primary motor cortex.

The VIM, a relatively small nucleus measuring 8–9 mm ventrodorsally, 3–3.5 mm anteroposteriorly, and approximately 2–3 mm mediolaterally, has been neurophysiologically characterized through unit recordings [16]. Neurons within the VIM have been identified in patients exhibiting responses to contralateral joint movements and muscle pressure, both active and passive, defining a kinesthetic or deep sensitivity. Anatomically, these neurons are situated anterior to the cutaneous sensitivity, corresponding to the VC, thus delineating a distinct region outside the motor thalamus. This phenomenon has been extensively documented in neurophysiological literature [17] and surgical procedures [18]. In patients with tremor, both ET and/or tremor-dominant PD, VIM neurons fire synchronously with the tremor. Thus, lesioning these neurons conveys a reduction in tremor severity.

The most common surgical approach for intractable disabling tremor has been thalamic DBS. The obvious advantages of DBS include its adjustability for optimizing efficacy and minimizing adverse effects, as well as its feasibility for bilateral treatment. However, some disadvantages of DBS include the need for ongoing adjustment, battery replacement, device-related issues, and the surgical risks of intracranial bleeding and infection. Patients with significant medical illness, elderly patients, or patients who are unwilling to have an invasive neurosurgical procedure with permanently implanted hardware might consider MRgFUS as an appropriate alternative to DBS if the safety and efficacy profiles were similar.

MRgFUS for Parkinson's disease

Tremor is one of the common motor symptoms of Parkinson's Disease (PD). Parkinsonian tremor is classified as rest tremor when trembling is suppressed while performing voluntary movements, or as action tremor if it manifests during voluntary muscle contraction. Parkinsonian tremor is thought to arise from aberrant oscillatory activity in the cerebello-thalamo-cortical circuit triggered by an abnormal activity in the basal ganglia-cortical loop circuits. Therefore, surgical targets like the VIM, the subthalamic nucleus (STN), the internal GPi or the posterior subthalamic area (STA or PSA) have demonstrated their efficacy at suppressing or improving tremor in patients with PD [19]. Other PD symptoms, like rigidity and bradykinesia, can also show improvements after surgical treatment in these areas. Intuitively, VIM lesioning with MRgFUS was the first therapeutic approach in patients with PD, and the first initial clinical results were published in a seminal paper by Bond et al. [20].

However, PD is more than tremor and many patients exhibit severe rigidity and bradykinesias. In these patients, lesions in other targets such as the STN or GPi based on the thousands of patients treated with DBS in these structures are more appropriate. As experience grew and the Exablate 4000 (Insightec Ltd, Haifa, Israel) device[1] was installed in centers with notable experience in subthalamic nucleus lesioning with radiofrequency, STN lesioning with MRgFUS began to be used and thoroughly studied with significant published studies [21, 22]. Almost simultaneously to this, MRgFUS pallidotomy (lesioning the GPi) was also performed in several centers in the world, including our own. The results of a multi-center clinical trial lesioning GPi with MRgFUS have been published in the paper written by Krishna et al. [23]. Interestingly, other lesional targets that were used in the past, such as the pallidothalamic tract (PTT), have also been proposed and used for patients with PD, dystonia, and X-linked parkinsonism-dystonia [24–26]. This cornucopia of articles, trials, and publications is a clear representation of the versatility of MRgFUS and how it allows clinicians to choose an individualized and tailor-made target for each patient with PD, hinging on their main clinical features or complaints.

We strongly believe that each of the published targets for PD has its pros and cons, so a thorough evaluation of the patient and detailed information of the expected outcome and risks must be provided to the patient and their family. For instance, pallidotomy or PTT seems to be a very valuable target for patients who mainly complain about dyskinesia and/or dystonia, whereas STN can be a good target for patients with rigidity, bradykinesia, and tremor who respond well to levodopa and have no limiting or significant dyskinesia. STN would also be an excellent option for PD patients with a predominance of rigidity and akinesia as the main complaint. On the other hand, VIM is still a very good target for patients with tremor-dominant PD who still have good control of the other motor symp-

[1] *The information shown herein refers to products of 3rd party manufacturers and thus are in their regulatory responsibility. Please contact the 3rd party manufacturer for further information.*

toms with levodopa medication, or who have some cognitive, behavioral, or psychiatric comorbidity that may be negatively impacted by a lesion in the STN and/or GPi. There are a lot of nuances about these last statements that could yield a very long discussion, but we believe that this would be out of the scope of the present article.

The use of MRgFUS for PD stands out as an alternative to other invasive therapies, particularly DBS, with a few advantages but also some drawbacks. Firstly, MRgFUS offers an incisionless approach, eliminating the need for surgical procedures involving electrode implantation. This significantly reduces the risk of infection, complications related to surgery, and the overall burden on patients undergoing open interventions. This is a key point when offering advanced therapies for elderly patients, as it is common practice (at least in our country) to refrain from indicating DBS surgery to patients who are older than 75. MRgFUS does not have such an age limit on its indication, so the population of PD patients who can be treated is significantly bigger. Secondly, MRgFUS allows precise targeting of specific brain regions with high accuracy, ensuring focused treatment on areas implicated in PD pathology. This precision minimizes the likelihood of unintended effects on neighboring structures and enhances the safety profile of the treatment. Another crucial advantage (although in this case it is more applicable when comparing MRgFUS to radiosurgery) is the real-time monitoring capability of MRgFUS and instantaneous assessment of effectiveness. Continuous MRI during the procedure enables clinicians to monitor and adjust the treatment parameters as needed, ensuring optimal therapeutic outcomes while maintaining safety. Lastly, a presumably better cost-efficiency ratio, and the clearly lower number of follow-up visits required with MRgFUS are characteristics that may make us err on the side of MRgFUS in the debate around DBS vs. MRgFUS.

Deep brain stimulation is still a very crucial treatment for movement disorders and it still has advantages when we compare it to MRgFUS. The fact that the treatment can be done bilaterally in one session or treatment day is clearly an advantage, since many PD and/or ET patients seek treatment with bilateral involvement of their disease (or perhaps not as asymmetric as we would like for MRgFUS). The reversibility of stimulation-induced side effects as compared to the potential irreversibility of lesion-induced side effects is also a feature that favors DBS. DBS also has a stronger point in the patient selection process, as it has no limitations in terms of skull characteristics (skull density ratio, skull thickness) or conditions that are incompatible with MRI. All things considered, we believe that both techniques should be indicated and used in patients with movement disorders. It is therefore not a question of MRgFUS vs DBS, but rather of which treatment is best for each patient.

Other therapeutic indications for MRgFUS

MRgFUS has expanded its medical applications beyond PD and ET, showcasing versatility and efficacy in various therapeutic areas. As in the case of other surgical techniques, it is important to note that the first experiences with high-frequency MRgFUS were treatments for patients with chronic neuropathic pain [27–30]. Ongoing investigations are exploring the utility of MRgFUS in epilepsy, psychiatric conditions such as major depressive disorder (MDD), obsessive-compulsive disorder (OCD), and dystonia [2–8, 26].

Beyond the lesional interventions, the horizon of high-frequency MRgFUS is far broader when we consider the applications and the future of LIFU. With slight modifications in the hardware and software, Insightec has developed the MR-guided LIFU that has proved capable of opening the BBB in a series of studies for diseases such as amyotrophic lateral sclerosis (ALS), Parkinson's-associated dementia, Alzheimer's disease, and neuro-oncologic conditions [31–34]. This feature facilitates targeted drug delivery to the brain, implying a promising future for these hitherto lethal or highly impairing diseases. The possibility to achieve neuromodulation with LIFU is also exciting, as a great deal of therapeutic, physiological, and anatomical research can emerge from the early published papers [35–38].

As research and clinical trials continue to unfold, the applications of MRgFUS across diverse medical domains highlight its versatility and its potential to revolutionize treatment approaches in various specialties.

New technical stepping stones

High-quality MRI is key in MRgFUS, as both precise target positioning and MR thermometry monitoring are imperative to achieve safe and successful treatments. The large size of the HIFU transducer prevents the use of routine MR coils. Until recently, treatments could only be performed with the magnet bore body coil, resulting in long scan times to improve the signal-to-noise ratio, and therefore longer treatment times.

As MRgFUS treatments become more prevalent, it is creating a need for dedicated multi-channel coils that are compatible with this set-up. An improvement in the MR signal reception directly translates to reduced scan times, better visualization of anatomical brain structures, more precise thermometry measurements, and increased temporal and spatial resolution during temperature monitoring.

A two-channel receive-only RF coil (Fig. 1) has been recently developed (Insightec Ltd, Haifa, Israel). This head coil consists of two flexible loop elements that are fully integrated in the silicone membrane that contains the patient's skin-cooling water.

The Insightec software has undergone significant enhancements since our first ↗MAGNETOM Flash article [39]. Noteworthy improvements in the latest software version include automatic segmentation and marking of calcifications and air sinuses as non-pass regions, strategically guiding ultrasound beams away from these areas. Additionally, the software now features a redesigned archive dialog for convenient retrieval and selection of CT and MR images, streamlining the pre-operative image upload process. Moreover, advancements aimed at enhancing patient safety and refining targeting control have been implemented through updates to movement detection algorithms and adjustments to temperature limit thresholds.

In tandem with these advancements, Insightec is actively investigating the potential of low-frequency MRgFUS to temporarily open the blood-brain barrier, facilitating direct drug delivery to specific brain targets and paving the way for groundbreaking disease-modifying therapies, as mentioned in the previous section.

Advanced imaging protocols

New therapeutic targets require dedicated imaging sequences for accurate target selection in MRgFUS, such as the STN or the GPi. At Clínica Universidad de Navarra, our pre- and post- MRI protocols always include a high-resolution T1-weighted MPRAGE, T2-weighted SPACE, SWI, and DTI scan. Both T1 and T2-weighted acquisitions can be employed in VIM-targeted procedures, while T2-weighted is particularly useful for direct STN targeting, as this nucleus shows hypointense contrast compared to its surrounding tissue in the T2 images. However, conventional T1 and T2 sequences do not typically allow differentiation between the internal and external divisions of the globus pallidus. Hence, for GPi-targeted procedures, we have adapted an MP2RAGE sequence [40] to acquire an FGATIR-like contrast (FLAWS1), and a combined (UNI) image with improved gray- and white-matter tissue differentiation (Fig. 2), allowing the distinction of the internal medullary lamina that separates the GPi from its external counterpart.

Until recently, intraoperative assessment of the lesion was limited to 2D T2-weighted TSE imaging, acquired with multiple averages to compensate for the SNR deprivation of operating without a dedicated coil, and with only partial brain coverage to restrain acquisition time. The availability of the 2-channel coil membrane has opened the possibility for new intra-operative protocol settings, such as 2D T2-STIR imaging with TI optimized to null the white-matter signal for better lesion conspicuity (Fig. 3A).

Aside from the aforementioned imaging sequences, our post-operative protocol also includes a selective 2D T2-weighted BLADE acquisition (Fig. 3C), with high in-plane resolution, centered at the lesion plane. Post-treatment evaluation is performed at our center 30 minutes after treatment end, and patients often show signs of fatigue after the intervention, which may result in involuntary motion and thus hinder the acquisition of good-quality, high-resolution, volumetric images. In such

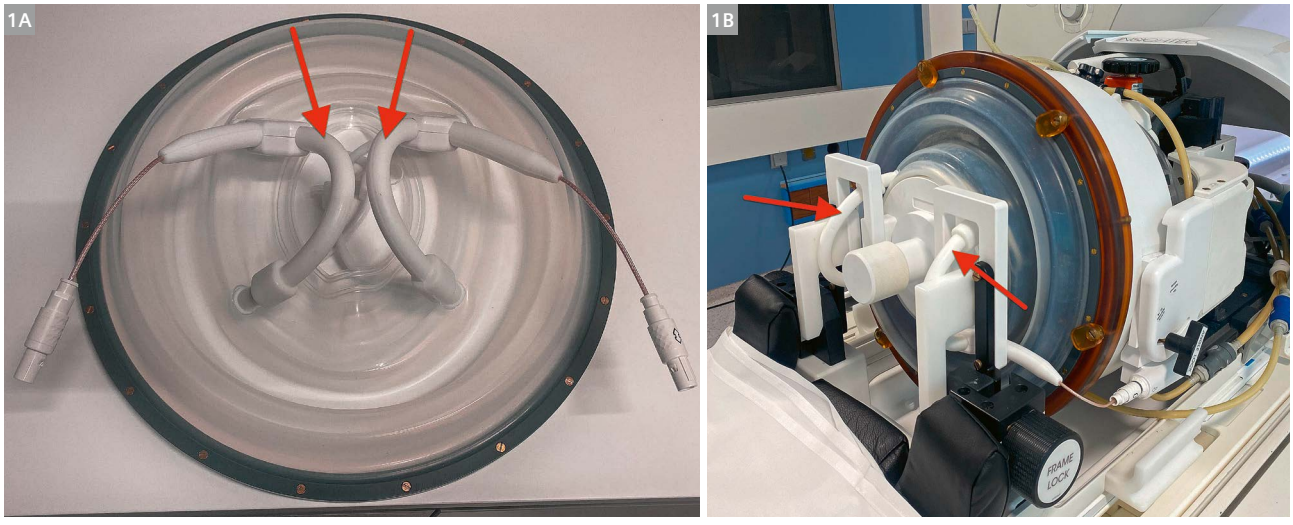

1 New two-channel head coil[1] integrated in the patient's membrane used in MRgFUS, outside **(1A)** and inside the MRgFUS **(1B)** environment. The two channels are indicated with the red arrows. The channel rings fall at both sides of the patient's head during the procedure.

[1] *The information shown herein refers to products of 3rd party manufacturers and thus are in their regulatory responsibility. Please contact the 3rd party manufacturer for further information.*

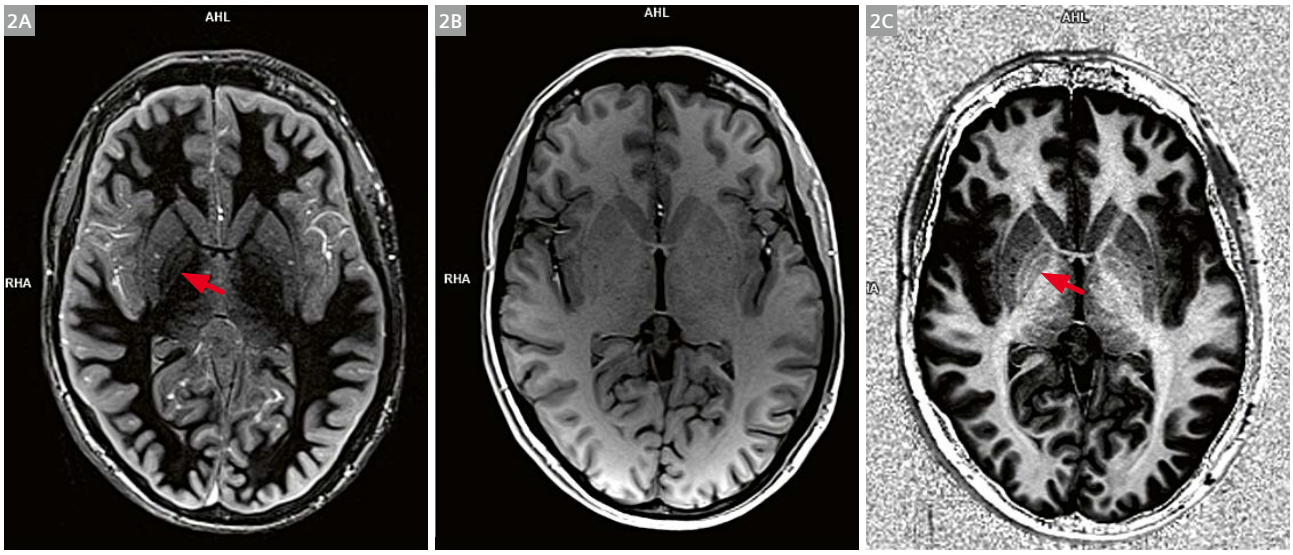

2 Example of modified MP2RAGE acquisition used in GPi-targeted presurgical protocol. The clear and concise distinction between Globus Pallidus Internus (GPi) and Globus Pallidus Externus (GPe) is highlighted by the arrows in figures 2A and 2C. Imaging parameters include TE/TI1/TI2/TR = 2.8/409/1620/3000 ms, 0.9 mm isotropic voxel size, TA = 8.5 min. **(2A)** shows the first inversion image with FGATIR-like contrast (FLAWS1), nulling the white-matter tissue signal. **(2B)** shows the second inversion image with MPRAGE-like contrast (FLAWS2). **(2C)** shows the MP2RAGE combined image (UNI) with improved gray- and white-matter differentiation in the basal ganglia.

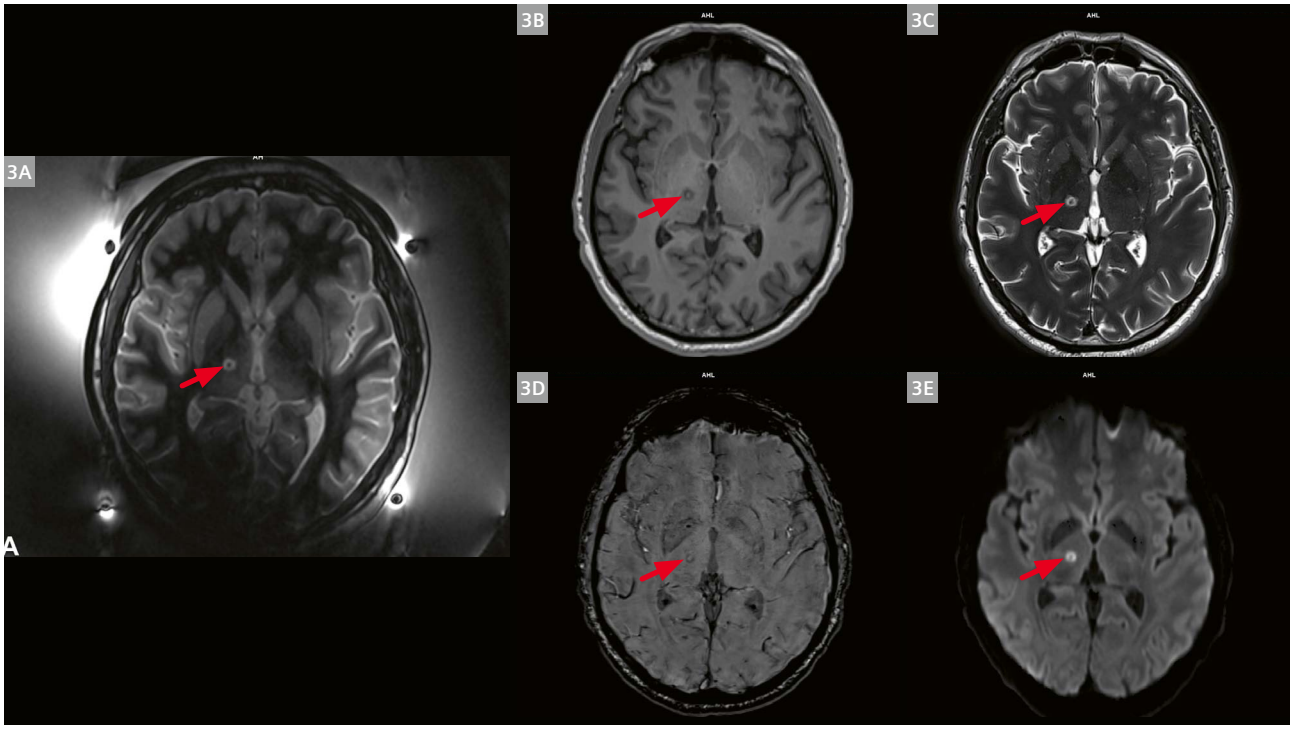

3 Intra- and post-surgical images of a representative subject who underwent a VIM-targeted MRgFUS treatment. Panel **(3A)** shows the newly optimized T2-STIR protocol acquired in the intra-operative setting (notice the water pool surrounding the patient's head), with TI = 400 ms to null the white-matter signal and improve lesion conspicuity. The right panel shows the post-operative T1 MPRAGE **(3B)**, T2 BLADE **(3C)**, SWI **(3D)** and DWI with b-value =1000 s/mm^2 **(3E)** images. A well-differentiated circular-shaped lesion created by the focused ultrasound beams can be observed in the post-op images (arrows).

cases, the BLADE readout is particularly useful, as it has an inherent robustness against motion thanks to its radial sampling.

Future directions

One of the most important recent milestones is that MRgFUS bilateral staged thalamotomy has been approved in the United States and has received a European CE mark as a treatment for drug-resistant ET. Many patients presenting with this condition in our clinics exhibit predominantly symmetric tremors affecting both upper extremities. Initially, treatment is offered for the limb corresponding to the patient's dexterity or the one deemed most necessary. However, in some patients the contralateral tremor evolves into a genuine disability, encompassing vocal and axial tremors. Consequently, bilateral staged MRgFUS thalamotomy has been used at the Clínica Universidad de Navarra since October 2023 (Fig. 4).

In line with the U.S. approval and the CE mark, candidates for this bilateral staged treatment are those who have surpassed nine months since the initial thalamotomy. Some published series suggest a timeframe of 6 to 12 months from the first treatment [9, 41, 42]. These candidates should also present refractory, debilitating tremors unresponsive to medical therapy. Furthermore, improvement in vocal and axial tremors has been noted in patients treated bilaterally [9]. However, despite their safety, bilateral treatments have been associated with higher rates of adverse effects compared to unilateral treatment, particularly gait ataxia and dysarthria [41, 42]. Many other possible applications of MRgFUS are being developed.

Experience after more than 350 treatments in Clínica Universidad de Navarra

More than 350 focused ultrasound treatments have been performed so far at our institution, making the Clínica Universidad de Navarra one of the centers with extensive experience in MRgFUS using a 3T MRI system (MAGNETOM Skyra, Siemens Healthineers, Erlangen, Germany). We have treated patients with Essential Tremor, Parkinson's disease, chronic neuropathic pain, and various unusual or atypical tremors (such as task-specific, post-traumatic, post-ischemic, or drug-induced tremor). Recently, six patients with ET underwent bilateral VIM MRgFUS ablation, following U.S. approval for bilateral staged thalamotomy for ET.

The learning curve has allowed us to hone our modus operandi and improve our results, both from an effectiveness and a safety standpoint. We have observed a decreased incidence of adverse events in the last 150 patients, in comparison with the first 200 cases. These improvements are thanks to the "human factor", and to the imaging techniques and technology that have made important leaps since our first MAGNETOM Flash article detailing our experience after the first year of using MRgFUS [39]. Since June 2022, we have been able to perform our treatments with the aforementioned head-coil membrane. This membrane is definitely helpful for characterizing the lesion intraoperatively and for checking the proximity of the lesion to critical structures such as the internal capsule. In targets such as STN or PTT, this improved intraoperative imaging allows us to directly observe either the target (STN, GPi) or reference structures surrounding the intended target such as the mammillothalamic tract (fascicle of Vicq d'Azyr), red nucleus, or internal capsule. Furthermore, we are continuously widening our indications and targets. For instance,

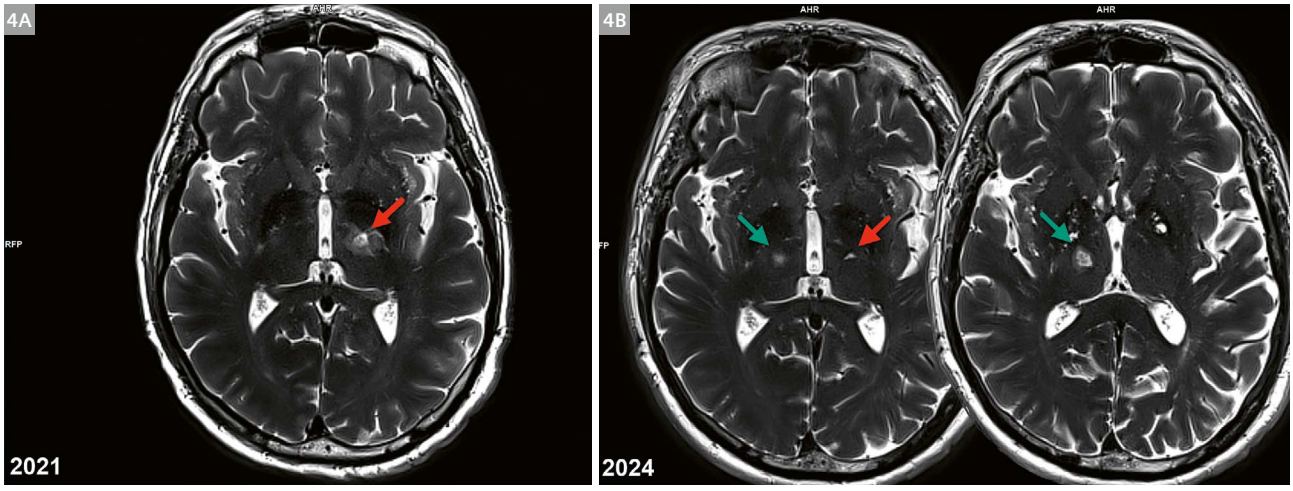

4 Example of a bilateral treatment for drug-resistant ET case performed at our center. The left panel **(4A)** shows the lesion created in the left hemisphere during the patient's MRgFUS treatment in 2021 (red arrow). The right panel **(4B)** shows the latest lesion created in the contralateral hemisphere in 2024 (green arrow).

we have performed pallidothalamic tractotomy for patients with PD, ventral oral thalamotomy for task-specific tremor and for focal hand dystonia, and in 2019 we were the first center in Spain to perform a centrolateral thalamotomy for pain. We believe that a fruitful and ongoing scientific partnership with both Siemens Healthineers and Insightec is of paramount importance to achieve good results and continue growing. With a cutting-edge technique such as MRgFUS, being up to date and participating in new clinical trials are key. In that sense, we are proud to have collaborated in multi-center clinical trials and to be currently working on developing new trials with novel indications and targets.

Abbreviations

ALS:	Amyotrophic lateral sclerosis
BBB:	Blood-brain barrier
CNP:	Chronic neuropathic pain
CT:	Computed Tomography
DBS:	Deep brain stimulation
DRT:	Dentatorubrothalamic tract
DTI:	Diffusion tensor imaging
DWI:	Diffusion-weighted imaging
ET:	Essential tremor
FGATIR:	Fast gray matter acquisition T1 inversion recovery
GPi:	Globus pallidus
HIFU:	High-intensity focused ultrasound
LIFU:	Low-intensity focused ultrasound
MDD:	Major depressive disorder
MRgFUS:	Magnetic resonance-guided focused ultrasound
MRI:	Magnetic resonance imaging
OCD:	Obsessive-compulsive disorder
PD:	Parkinson's Disease
PSA:	Posterior subthalamic area
PTT:	Pallidothalamic tract
RF:	Radiofrequency
SDR:	Skull density ratio
SPACE:	Sampling Perfection with Application-optimized Contrast using different flip angle Evolutions
STA:	Subthalamic area
STN:	Subthalamic nucleus
SWI:	Susceptibility-weighted imaging
VC:	Ventrocaudalis
VIM:	Ventral intermediate nucleus
VLp:	Posterior part of the ventral lateral nucleus
Voa:	Ventralis oralis anterior
Vop:	Ventralis oralis posterior

References

1 Meng Y, Suppiah S, Mithani K, Solomon B, Schwartz ML, Lipsman N. Current and emerging brain applications of MR-guided focused ultrasound. J Ther Ultrasound. 2017;5:26.

2 Jung HH, Kim SJ, Roh D, Chang JG, Chang WS, Kweon EJ, et al. Bilateral thermal capsulotomy with MR-guided focused ultrasound for patients with treatment-refractory obsessive-compulsive disorder: a proof-of-concept study. Mol Psychiatry. 2015;20(10): 1205–1211.

3 Kim SJ, Roh D, Jung HH, Chang WS, Kim CH, Chang JW. A study of novel bilateral thermal capsulotomy with focused ultrasound for treatment-refractory obsessive-compulsive disorder: 2-year follow-up. J Psychiatry Neurosci. 2018;43(5):327–337.

4 Davidson B, Hamani C, Rabin JS, Goubran M, Meng Y, Huang Y, et al. Magnetic resonance-guided focused ultrasound capsulotomy for refractory obsessive compulsive disorder and major depressive disorder: Clinical and imaging results from two phase I trials. Mol Psychiatry. 2020;25(9):1946–1957.

5 Davidson B, Hamani C, Huang Y, Jones RM, Meng Y, Giacobbe P, et al. Magnetic Resonance-Guided Focused Ultrasound Capsulotomy for Treatment-Resistant Psychiatric Disorders. Oper Neurosurg (Hagerstown). 2020;19(6):741–749.

6 Krishna V, Mindel J, Sammartino F, Block C, Dwivedi AK, Van Gompel JJ, et al. A phase 1 open-label trial evaluating focused ultrasound unilateral anterior thalamotomy for focal onset epilepsy. Epilepsia. 2023;64(4):831–842.

7 Abe K, Yamaguchi T, Hori H, Sumi M, Horisawa S, Taira T, et al. Magnetic resonance-guided focused ultrasound for mesial temporal lobe epilepsy: a case report. BMC Neurol. 2020;20(1):160.

8 Yamaguchi T, Hori T, Hori H, Takasaki M, Abe K, Taira T, et al. Magnetic resonance-guided focused ultrasound ablation of hypothalamic hamartoma as a disconnection surgery: a case report. Acta Neurochir (Wien). 2020;162(10):2513–2517.

9 Martínez-Fernández R, Mahendran S, Pineda-Pardo JA, Imbach LL, Máñez-Miró JU, Büchele F, et al. Bilateral staged magnetic resonance-guided focused ultrasound thalamotomy for the treatment of essential tremor: a case series study. J Neurol Neurosurg Psychiatry. 2021;92(9):927–931.

10 Parras O, Domínguez P, Tomás-Biosca A, Guridi J. The role of tractography in the localisation of the Vim nucleus of the thalamus and the dentatorubrothalamic tract for the treatment of tremor. Neurologia (Engl Ed). 2022;37(8):691–699.

11 Caston RM, Campbell JM, Rahimpour S, Moretti P, Alexander MD, Rolston JD. Hemorrhagic Safety of Magnetic Resonance-Guided Focused Ultrasound Thalamotomy for Tremor without Interruption of Antiplatelet or Anticoagulant Therapy. Stereotact Funct Neurosurg. 2023;101(5):314–318.

12 Louis ED, Ferreira JJ. How common is the most common adult movement disorder? Update on the worldwide prevalence of essential tremor. Mov Disord. 2010;25(5):534–541.

13 Bhatia KP, Bain P, Bajaj N, Elble RJ, Hallett M, Louis ED, et al. Consensus Statement on the classification of tremors. from the task force on tremor of the International Parkinson and Movement Disorder Society. Mov Disord. 2018;33(1):75–87.

14 Macchi G, Jones EG. Toward an agreement on terminology of nuclear and subnuclear divisions of the motor thalamus. J Neurosurg. 1997;86(4):670–685. https://doi.org/10.1080/02688697.2021.1958150

15 Hirai T, Jones EG. A new parcellation of the human thalamus on the basis of histochemical staining. Brain Res Rev. 1989;14(1):1–34.

16 Lenz FA, Kwan HC, Martin RL, Tasker RR, Dostrovsky JO, Lenz YE. Single unit analysis of the human ventral thalamic nuclear group. Tremor-related activity in functionally identified cells. Brain. 1994;117(3):531–543.

17 Tasker RR, Kiss ZH. The role of the thalamus in functional neurosurgery. Neurosurg Clin N Am. 1995;6(1):73–104.
18 Ohye C, Maeda T, Narabayashi H. Physiologically defined VIM nucleus. Its special reference to control of tremor. Appl Neurophysiol. 1976-1977;39(3-4):285–295.
19 Abusrair AH, Elsekaily W, Bohlega S. Tremor in Parkinson's Disease: From Pathophysiology to Advanced Therapies. Tremor Other Hyperkinet Mov (N Y). 2022;12:29.
20 Bond AE, Shah BB, Huss DS, Dallapiazza RF, Warren A, Harrison MB, et al. Safety and Efficacy of Focused Ultrasound Thalamotomy for Patients With Medication-Refractory, Tremor-Dominant Parkinson Disease: A Randomized clinical Trial. JAMA Neurol. 2017;74(12): 1412–1418.
21 Martínez-Fernández R, Rodríguez-Rojas R, Del Álamo M, Hernández-Fernández F, Pineda-Pardo JA, Dileone M, et al. Focused ultrasound subthalamotomy in patients with asymmetric Parkinson's disease: a pilot study. Lancet Neurol. 2018;17(1):54–63.
22 Martínez-Fernández R, Máñez-Miró JU, Rodríguez-Rojas R, Del Álamo M, Shah BB, Hernández-Fernández F, et al. Randomized Trial of Focused Ultrasound Subthalamotomy for Parkinson's Disease. N Engl J Med. 2020;383(26):2501–2513.
23 Krishna V, Fishman PS, Eisenberg HM, Kaplitt M, Baltuch G, Chang JW, et al. Trial of Globus Pallidus Focused Ultrasound Ablation in Parkinson's Disease. N Engl J Med. 2023;388(8):683–693.
24 Gallay MN, Moser D, Rossi F, Magara AE, Strasser M, Bühler R, et al. MRgFUS Pallidothalamic Tractotomy for Chronic Therapy-Resistant Parkinson's Disease in 51 Consecutive Patients: Single Center Experience. Front Surg. 2020;6:76.
25 Gallay MN, Moser D, Magara AE, Haufler F, Jeanmonod D. Bilateral MR-Guided Focused Ultrasound Pallidothalamic Tractotomy for Parkinson's Disease With 1-Year Follow-Up. Front Neurol. 2021;12: 601153.
26 Jamora RDG, Chang WC, Taira T. Transcranial Magnetic Resonance-Guided Focused Ultrasound in X-Linked Dystonia-Parkinsonism. Life (Basel). 2021;11(5):392.
27 Martin E, Jeanmonod D, Morel A, Zadicario E, Werner B. High-intensity focused ultrasound for noninvasive functional neurosurgery. Ann Neurol. 2009;66(6):858–861.
28 Gallay MN, Moser D, Jeanmonod D. MR-Guided Focused Ultrasound Central Lateral Thalamotomy for Trigeminal Neuralgia. Single Center Experience. Front Neurol. 2020;11:271.

Contact

Lain Hermes Gonzalez-Quarante, M.D.
Neurosurgery Department
Clínica Universidad de Navarra
Avda. Pío XII, 36
31008 Pamplona (Navarra)
Spain
Tel.: +34 948 255 400
lgonzalezq@unav.es

29 Gallay MN, Magara AE, Moser D, Kowalski M, Kaeser M, Jeanmonod D. Magnetic resonance-guided focused ultrasound central lateral thalamotomy against chronic and therapy-resistant neuropathic pain: retrospective long-term follow-up analysis of 63 interventions. J Neurosurg. 2023;139(3):615–624.
30 Ahmed AK, Zhuo J, Gullapalli RP, Jiang L, Keaser ML, Greenspan JD, et al. Focused Ultrasound Central Lateral Thalamotomy for the Treatment of Refractory Neuropathic Pain: Phase I Trial. Neurosurgery. 2024;94(4):690–699.
31 Lipsman N, Meng Y, Bethune AJ, Huang Y, Lam B, Masellis M, et al. Blood-brain barrier opening in Alzheimer's disease using MR-guided focused ultrasound. Nat Commun. 2018;9(1):2336.
32 Abrahao A, Meng Y, Llinas M, Huang Y, Hamani C, Mainprize T, et al. First-in-human trial of blood-brain barrier opening in amyotrophic lateral sclerosis using MR-guided focused ultrasound. Nat Commun. 2019;10(1):4373.
33 Gasca-Salas C, Fernández-Rodríguez B, Pineda-Pardo JA, Rodríguez-Rojas R, Obeso I, Hernández-Fernández F, et al. Blood-brain barrier opening with focused ultrasound in Parkinson's disease dementia. Nat Commun. 2021;12(1):779.
34 Rezai AR, D'Haese PF, Finomore V, Carpenter J, Ranjan M, Wilhelmsen K, et al. Ultrasound Blood-Brain Barrier Opening and Aducanumab in Alzheimer's Disease. N Engl J Med. 2024;390(1):55-62.
35 Dallapiazza RF, Timbie KF, Holmberg S, Gatesman J, Lopes MB, Price RJ, et al. Noninvasive neuromodulation and thalamic mapping with low-intensity focused ultrasound. J Neurosurg. 2018;128(3): 875–884.
36 Legon W, Ai L, Bansal P, Mueller JK. Neuromodulation with single-element transcranial focused ultrasound in human thalamus. Hum Brain Mapp 2018;39:1995–2006.
37 Sanguinetti JL, Hameroff S, Smith EE, Sato T, Daft CMW, Tyler WJ, et al. Transcranial Focused Ultrasound to the Right Prefrontal Cortex Improves Mood and Alters Functional Connectivity in Humans. Front Hum Neurosci. 2020;14:52.
38 Cain JA, Visagan S, Johnson MA, Crone J, Blades R, Spivak NM, et al. Real time and delayed effects of subcortical low intensity focused ultrasound. Sci Rep. 2021;11(1):6100.
39 Vidorreta M, Fernandez M, Domínguez P, Aviles-Olmos I, Gorospe A, Rodriguez-Oroz MC, et al. Experience after One Year with MRgFUS. ↗MAGNETOM Flash. 2019;75(4):36–41.
40 Tanner M, Gambarota G, Kober T, Krueger G, Erritzoe D, Marques JP, et al. Fluid and white matter suppression with the MP2RAGE sequence. J Magn Reson Imaging. 2012;35(5):1063–1070.
41 Iorio–Morin C, Yamamoto K, Sarica C, Zemmar A, Levesque M, Brisebois S, et al. Bilateral Focused Ultrasound Thalamotomy for Essential Tremor (BEST–FUS Phase 2 Trial). Mov Disord. 2021;36(11):2653–2662.
42 Fukutome K, Hirabayashi H, Osakada Y, Kuga Y, Ohnishi H. Bilateral Magnetic Resonance Imaging-Guided Focused Ultrasound Thalamotomy for Essential Tremor. Stereotact Funct Neurosurg. 2022;100(1):44–52.
43 Kultas-Ilinsky K, Ilinsky IA. Fine structure of the ventral lateral nucleus (VL) of the Macaca mulatta thalamus: cell types and synaptology. J Comp Neurol. 1991;314(2):319–349.

PREDICTOM
EARLY DEMENTIA DETECTION

Working together to develop a screening platform to enhance the detection and management of Alzheimer's disease

PREDICTOM is an international across sector initiative to bring dementia diagnostics closer to the public through a customisable cognitive and biomarker screening platform

predictom.eu

CONTACT US: predictom@sus.no

COCIR Advancing Healthcare · efpia · EuropaBio · MedTech Europe from diagnosis to cure · Vaccines Europe · Co-funded by the European Union · IHI innovative health initiative

PREDICTOM receives funding the Innovative Joint Undertaking under Grant Agreement no. 101132356. This Joint Undertaking receives support from the European Union's Horizon Europe research and innovation programme, COCIR, EFPIA, MedTechEurope and Vaccines Europe. Our UK and Swiss partners receive funding from UKRI and Swiss State Secretariat.
See www.predictom.eu for more details.

Cover images

Upper left: T2 FLAIR with Deep Resolve (Study-ID: 2aaaa2636)

Upper right: Amyloid PET MRI, acquired on BIOGRAPH mMR (Study-ID: 4aaaa0025), Image courtesy of University Hospital, Plzen, Czech Republic

Lower left: DTI, Image courtesy of Cardiff University Brain Research Imaging Centre (CUBRIC), Wales, United Kingdom

Lower right: Data courtesy of Lausanne University Hospital, Lausanne, Switzerland

Not for distribution in the US

On account of certain regional limitations of sales rights and service availability, we cannot guarantee that all products included in this brochure are available through the Siemens Healthineers sales organization worldwide. Availability and packaging may vary by country and is subject to change without prior notice. Some/All of the features and products described herein may not be available in the USA.

The information in this document contains general technical descriptions of specifications and options as well as standard and optional features which do not always have to be present in individual cases, and which may not be commercially available in all countries. Due to regulatory reasons their future availability cannot be guaranteed. Please contact your local Siemens Healthineers organization for further details.

Siemens Healthineers reserves the right to modify the design, packaging, specifications, and options described herein without prior notice. Please contact your local Siemens Healthineers sales representative for the most current information.

Note: Any technical data contained in this document may vary within defined tolerances. Original images always lose a certain amount of detail when reproduced.

Siemens Healthineers Headquarters
Siemens Healthineers AG
Siemensstr. 3
91301 Forchheim, Germany
Phone: +49 9191 180
siemens-healthineers.com

Published by Siemens Healthineers AG · Order No. A91MR-01000-0012M-7600 · Printed in Germany · 17892 326 ·